Bachelor's Thesis

Monte Carlo Simulation Radiation Transport - Radiation Analysis for the nano-satellite AcubeSAT

Department of Physics
Aristotle University of Thessaloniki

Michael Chadolias

Thessaloniki, 10th of March, 2022

Submitted in partial fulfillment of the requirements for the degree of B. Sc. in Physics
Supervised by Prof Christos Elefteriadis

Abstract

This thesis includes the radiation studies for the first nano satellite, AcubeSAT from the Aristotle University of Thessaloniki. This research was conducted inside the SpaceDot team, which participates in the third round of the "Fly Your Satellite!" program under of the European Space Agency(ESA). AcubeSAT is a greek student 3U-Cubesat, that host inside a biological experiment, that studies the effect of radiation and microgravity to eykariotic cells, with the expected launch to occur in the second quarter of 2023. A detailed analysis for the flux and the flunce of trapped particles, solar particles and galactic cosmic rays in a LEO orbit. The LET and the total ionizing dose has been calculated for a spherical shell geometry. The simulation was conducted with the OMERE, a software developed by TRAD company with the support of CNES.

In addition, two simulations methods have been performed with the FASTRAD software: the ray-tracing simulation and forward Monte Carlo simulation. Ray-tracing simulation provides a sector shielding analysis of the models, giving an overview of the received radiation dose for each specific point in the models. Forward Monte Carlo provides an overview of the deposited radiation for each section of the model, which has proven particularly useful for the state-of-the-art model, in which the deposited dosage for each part of the model has been determined.

All simulations for the AcubeSAT missions indicate that the greatest contributor to radiation dose in the simulations came from trapped particles. From the dose levels results, the components of the satellite can endure and be functional during the whole duration of the mission.

Περίληψη

Η παρούσα διπλωματική εργασία περιλαμβάνει τις μελέτες ακτινοβολίας για τον πρώτο νανοδορυφόρο, AcubeSAT από το Αριστοτέλειο Πανεπιστήμιο Θεσσαλονίκης. Αυτή η έρευνα διεξήχθη εντός της ομάδας SpaceDot, η οποία συμμετέχει στον τρίτο γύρο του "Fly Your Satellite!" πρόγραμμα στο πλαίσιο του Ευρωπαϊκού Οργανισμού Διαστήματος (ESA). Το AcubeSAT είναι ένας ελληνικός φοιτητικός δορυφόρος 3U-Cubesat, που φιλοξενεί ένα βιολογικό πείραμα, μελετώντας την επίδραση της ακτινοβολίας και της μικροβαρύτητας στα ευκαριώτικα κύτταρα, με την αναμενόμενη εκτόξευση να γίνει το δεύτερο τρίμηνο του 2023. Λεπτομερής ανάλυση για τη ροή και τη ροή παγιδευμένων σωματιδίων, ηλιακών σωματιδίων και γαλαξιακών κοσμικών ακτίνων σε τροχιά LEO. Το LET και η δόση ιονισμού έχουν υπολογιστεί για μια σφαιρική γεωμετρία κελύφους. Η προσομοίωση πραγματοποιήθηκε με το OMERE, ένα λογισμικό που αναπτύχθηκε από την εταιρεία TRAD με την υποστήριξη της CNES.

Επιπλέον, έχουν πραγματοποιηθεί δύο μέθοδοι προσομοίωσης με το λογισμικό FASTRAD: η προσομοίωση ray-tracing και η προσομοίωση Forward Monte Carlo. Η προσομοίωση ray-tracing παρέχει μια ανάλυση θωράκισης τομέα των μοντέλων, δίνοντας μια επισκόπηση της λαμβανόμενης δόσης ακτινοβολίας για κάθε συγκεκριμένο σημείο των μοντέλων. Το Forward Monte Carlo παρέχει μια επισκόπηση της εναποτιθέμενης ακτινοβολίας για κάθε τμήμα του μοντέλου, η οποία έχει αποδειχθεί ιδιαίτερα χρήσιμη για το υπερσύγχρονο μοντέλο, στο οποίο έχει καθοριστεί η δόση για κάθε τμήμα του μοντέλου.

Όλες οι προσομοιώσεις για την αποστολή AcubeSAT δείχνουν ότι η μεγαλύτερη συνεισφορά στη δόση ακτινοβολίας στις προσομοιώσεις προήλθε από παγιδευμένα σωματίδια από το μαγνητικό πεδ. Από τα επίπεδα της δόσης ακτινοβολίας, τα εξαρτήματα του δορυφόρου μπορούν να αντέξουν και να λειτουργήσουν καθ' όλη τη διάρκεια της αποστολής.

Dedication

To my family, who were always there for me. And to my friends for their emotional support.

Acknowledgements

I would like to thank Dr Christos Elefteriadis for giving me the opportunity to complete this research as part of Bachelors in Physics. I also would like to express my gratitude to my team members in the AcubeSAT, for their tireless effort in making the nanosatellite a reality! Special thanks are needed

Contents

1 Introduction **1**

2 AcubeSAT Mission **2**
2.1 CubeSat . . . 2
2.2 AcubeSAT . . . 2
2.2.1 Physical Architecture . . . 3
2.2.2 Physical Architecture Diagram . . . 6

3 Orbital Mechanics and Definition **7**
3.1 Keplerian motion model . . . 7
3.1.1 Keplerian Elements . . . 8
3.2 Low Earth Orbit . . . 9
3.3 Sun Synchronous Orbit . . . 9

4 Space Environment **12**
4.1 Space Environment . . . 13
4.1.1 Geomagnetic fields . . . 13
4.1.1.1 Geomagnetic Shielding (Størmer's theory) . . . 16
4.1.2 Van Allen Belts . . . 16
4.1.2.1 Phenomenology . . . 17
4.1.3 South Atlantic Anomaly . . . 18
4.1.4 Poles . . . 19
4.2 Sources of Radiation . . . 20
4.2.1 Trapped Particles . . . 20
4.2.1.1 East-West Effect . . . 21
4.2.1.2 Pitch-angle distribution . . . 22
4.2.2 Solar Particle Events . . . 22
4.2.2.1 Solar Protons . . . 22
4.2.2.2 Solar Flares . . . 23
4.2.2.3 Solar Cycles . . . 23
4.2.3 Galactic Cosmic Rays . . . 24
4.2.4 Secondary Particles . . . 25

5 Space Dosimetry **27**
5.1 Definition of Quantities . . . 27
5.1.1 Cross Section . . . 27
5.1.2 Fluence . . . 27
5.1.3 Flux . . . 28
5.1.4 Mass Stopping Power . . . 29
5.1.5 Linear Energy Transfer . . . 30
5.1.6 Absorbed Dose . . . 30
5.2 Interaction with Matter . . . 31
5.2.1 Charged Particles: Electrons and Heavy Charged Particles . . . 31
5.2.1.1 Coulomb Interaction . . . 31
5.2.1.2 Bremmstrahlung . . . 31
5.2.2 Photons . . . 32
5.2.2.1 Photoelectric Effect . . . 32
5.2.2.2 Compton Effect . . . 33
5.2.3 Neutrons . . . 34
5.2.3.1 Eleastic Scattering . . . 34
5.2.3.2 Inelastic Scattering . . . 35
5.2.3.3 Radiative Capture (n,X) . . . 35

6 Simulation Tools **37**
6.1 OMERE . . . 37
6.2 FASTRAD . . . 38

7 OMERE - Simulation Results **39**
7.1 Simulation Details and Mission Definition . . . 39
7.1.1 Assumptions in Orbit Definition . . . 39
7.2 Detector layout and shielding . . . 40
7.3 Results - SSO 600km . . . 40
7.3.1 Flux Calculation . . . 40
7.3.1.1 Trapped Protons and Electrons . . . 40
7.3.1.2 Solar Energetic Protons and Ions . . . 41
7.3.1.3 Solar Flares . . . 41
7.3.1.4 Galactic Cosmic Rays . . . 42
7.3.2 Linear Energy Transfer(LET) Calculation . . . 43
7.3.2.1 Mission Duration: 1 year . . . 43
7.3.2.2 Mission Duration: 1.5 year . . . 43
7.3.3 Dose Calculation . . . 44
7.3.3.1 Mission Duration: 1 year . . . 44
7.3.3.2 Mission Duration: 1.5 years . . . 45
7.4 Results - SSO 500km . . . 47

7.4.1 Flux Calculation . . . 47
7.4.1.1 Trapped Protons and Electrons . . . 47
7.4.1.2 Solar Energetic Protons and Ions . . . 47
7.4.1.3 Solar Flares . . . 48
7.4.1.4 Galactic Cosmic Rays . . . 49
7.4.2 Linear Energy Transfer(LET) calculation . . . 50
7.4.2.1 Mission Duration: 1 year . . . 50
7.4.2.2 Mission Duration: 1.5 years . . . 50
7.4.3 Dose Depth Calculation . . . 51
7.4.3.1 Mission Duration: 1 year . . . 51
7.4.3.2 Mission Duration: 1.5 year . . . 52

8 FASTRAD - Simulation Results 54
8.1 Simulation Techniques Models . . . 54
8.1.1 FMC Method . . . 54
8.1.2 Ray-Tracing Method . . . 58
8.2 Geometry Model . . . 60
8.3 Results . . . 61
8.3.1 Forward Monte Carlo Method . . . 61
8.3.2 Ray-Tracing Method . . . 64

9 Conclusion 66
9.1 Sector Shielding Analysis for future improvement . . . 66
9.2 FMC Method . . . 66
9.3 Model Variation . . . 67
9.4 AcubeSAT viability . . . 67
9.5 Future Work . . . 67
9.5.1 CubeSAT models . . . 67
9.5.2 Radiation Methods . . . 67

A Radiation Effects 68
A.1 Single Event Effects - SEE . . . 68
A.2 Total Ionizing Dose - TID . . . 68

B Workflow-diagram 69

List of Figures

2.1 AcubeSAT mock-up . . . 3
2.2 Render of the assembled Subsystem Stack . . . 4
2.3 Render of the unibody inside the payload container (exploded view). The SU Board and the valve mounting interface can also be seen. . . . 5
2.4 AcubeSAT Physical Architecture[19] . . . 6

3.1 Keplerian sphere . . . 8
3.2 Space Regions . . . 9
3.3 Types of Orbits . . . 9
3.4 Polar Orbit Representation . . . 10

4.1 Space Radiation Sources . . . 12
4.2 Earth's magnetic field lines . . . 13
4.3 Earth's magnetic intensity[41] . . . 14
4.4 Geocentric dipole approximation of the geomagnetic field [20] . . . 15
4.5 Van Allen Belts . . . 17
4.6 Motion of trapped charged particles in the geomagnetic field[11] . . . 19
4.7 South Atlantic Anomaly . . . 19
4.8 The three principal sources of space radiation: (1) galactic cosmic rays, (2)trapped particles in the ERBs and (3) solar particle events. . . . 20
4.9 Solar Cycle 25th prediction . . . 24

5.1 Flux from a point source [15] . . . 29
5.2 Representation of a photon track and an ion passing though matter [3] 30
5.3 Compton Scattering [31] . . . 33
5.4 Principle of elastic scattering for neutrons . . . 35
5.5 Radiative neutron capture process (n,X). From **PRETAM KUMAR DAS** . . . 36

6.1 Caption . . . 37
6.2 A look into the 3D environment of the FASTRAD. . . . 38

7.1 Flux Graph for Trapped Particles . . . 41
7.2 Flux Graph for Energetic Solar Particles . . . 41
7.3 Flux Graph for Solar Flares . . . 42

7.4 Flux Graph for Galactic Cosmic Rays . . . 42
7.5 Both LET curves at 4.7mm . . . 43
7.6 Both LET curves at 4.7mm . . . 44
7.7 Dose depth curve for silicon target . . . 45
7.8 Dose depth curve for muscle tissue target . . . 45
7.9 Dose depth curve for silicon target . . . 46
7.10 Dose depth curve for muscle tissue target . . . 46
7.11 Flux Graph for Trapped Particles . . . 47
7.12 Flux Graph for Energetic Solar Particles . . . 48
7.13 Flux Graph for Solar Flares . . . 48
7.14 Flux Graph for Galactic Cosmic Rays . . . 49
7.15 Both Linear Energy Transfer curves at 4.7mm . . . 50
7.16 Both Linear Energy Transfer curves at 4.7mm . . . 51
7.17 Dose depth curve for silicon target . . . 52
7.18 Dose depth curve for muscle tissue target . . . 52
7.19 Dose depth curve for silicon target . . . 53
7.20 Dose depth curve for muscle tissue target . . . 53

8.1 Passage of particles through matter. . . . 55
8.2 Method step visualization. . . . 55
8.3 Forward Monte Carlo particle generation. From [42] . . . 57
8.4 Solid angle calculation method. From the source. . . . 58
8.5 Slant Method Calculation. . . . 59
8.6 Slant path (left) and minimum path (right . . . 59
8.7 The AcubeSAT simplified model. . . . 61
8.8 Fluence for the various detectors in the model. . . . 62
8.9 Deposited dose in the OBC PCB . . . 63
8.10 Error in the deposited dose . . . 64
8.11 The rays tracing from the detector placed inside the OBC PCB . . . 65

B.1 Workflow Diagram . . . 69

List of Tables

4.1 Trapped particles properties [5] 21
4.2 Solar Particle Events properties [5] 22
4.3 The space radiation environment in LEO and interplanetary space [] . 22
4.4 Galactic Cosmic Rays properties [5] 25

7.1 AcubeSAT Orbital Parameters for the Baseline Orbit 39
7.2 AcubeSAT Orbital Parameters for the Upper Orbit 40
7.3 Dose-depth values for SSO 600km 46
7.4 Dose-depth values for SSO 500km 53

8.1 AcubeSAT dimensions 60
8.2 Dose-depth values for the FMC method 64
8.3 Ray-tracing method deposited doses 65

Acronyms

ADCS Altitude Determination and Control Subsystem. 4, 40

AP Argument of Periapsis. 39

CAD Computer-aided design. 38

CME Coronal Mass Ejection. 23

CNES National Centre for Space Studies. 37

COMMS Communications. 4, 40

COTs Commercial Off-The-Self. 4

ECSS European Cooperation for Space Standardization. 37

EPS Electric Power Supply. 4, 40

ERBs Earth's Radiation Belts. 8, 20

ESA European Space Agency. 38

ESP Energetic Solar Protons. 22

FMC Forward Monte Carlo. 54, 61, 67

GCR Galactic Cosmic Rays. 18, 19, 25

GeV Giga electron volt. 22

HZE High Atomic number and energy elements. 22, 26

IC Internal Charging. 67

keV kilo electron volt. 22

LEO Low Earth Orbit. 1

LET Linear Energy Transfer. 9, 30, 43, 50, 51

MeV Mega electron volt. 20

MTQ Magnetorquer. 4

OBC On Board Computer. 4, 40

PCB Printed Circuit Board. 4, 40

RMC Reverse Monte Carlo. 67

RTC Ray-Tracing Method. 54, 58, 64, 67

SAA South Atlantic Anomaly. 13, 18

SEP Solar Energetic Particles. 18, 19, 22

SI International System of Units. 30

SSO Sun-Synchronous Orbit. 9, 10, 47, 50

TA True Anomaly. 39

TID Total Ionizing Energy. 40, 67

1. Introduction

Space has become the next frontier in exploration. From the age of discovery in the 15^{th} century to the moon landing in 1969, space has truly become an integral piece in our lives today. According to the United Nations' Outer Space Objects[21], there are at close to 7,500 satellite only in LEO. Thanks to them today there is GPS, weather forecast, telecommunications across the world and etc.

However, the space environment is dangerous. Galactic cosmic rays (GCRs), solar particle events (SPEs), and energetic particles trapped in the Earth's magnetic field (Van Allen Belts) [30] are the three principal sources of space radiation. Different forms of radiation, such as protons, neutrons, electrons, heavy ions, gamma and x-rays, may be present in each of these sources. Space radiation has a broad spectrum of energy (from keV to GeV), and the exposure rate (particle flux) can change by many orders of magnitude in a matter of hours or days, especially during the SPEs[10].

Ionizing radiation is one of the major concerns during space mission development. Both the electronic components as well as the nature of the payload experiment are affected by radiation, which can result in detrimental consequences if some components fail under certain conditions.Effective analysis techniques for the study and prediction of the basic impacts of the particle environment on new technologies are required for knowledge of the possible consequence of the radiation environment on evolving space born gadgets.

For scientific missions, CubeSats[33] can provide low-cost and quick-turnaround options. The examination of the shielding supplied by the structure should be the first step in ensuring a CubeSat's radiation hardening. This thesis shows how the radiation simulation tool FASTRAD[18] can be used to carry out this investigation.

The thesis begin with a brief description of the AcubeSAT project in chapter 2. It is followed by a short introduction in orbital mechanics and a description of the Low Earth region as part of a radiation environment in chapter 3 and chapter 4 respectively. Continuing with a brief presentation of the dosimetric values studied in this thesis and the main particle interactions with matter in chapter 5. Starting with a mention of the software utilized in this study in chapter 6, the results in those software is presented for OMERE and FASTRAD in chapter 7 and chapter 8 duly. In the end, there is a discussion for the results of the analysis in chapter 9.

2. AcubeSAT Mission

2.1 CubeSat

A CubeSat is a small satellite standard that was developed to allow people to conduct space missions, and research on a budget with no restrictions based on organisation history [14]. The first CubeSat was deployed in 2002 and since then, universities, space agencies and government organisations have continued to launch them for education, research and operational deployment [34]. The physical standard adopted was 1U (10 cubic cm), with a volume of one litre and mass of 1.33kg or less from CalPoly and NASA standards [14]. The orbital deployer currently in use can cater for a 3U (three times all dimensions of a 1U) CubeSat, allowing flexibility for payload development [14].

Because the size of a satellite is directly proportional to the costs of physical materials and parts, development labor, and launch vehicle fuel, it is easy to deduce that the primary advantages of small satellites over their larger siblings are lower cost and quicker development time. Small satellites, on the other hand, offer their own set of technological and mission-related advantages. Because of the shorter development cycle[24], newer payload and bus technologies can be incorporated. Furthermore, compared to a single, large, traditional satellite, a network of multiple tiny satellites has the potential to be more adaptable, as it may be adjusted based on mission requirements.

2.2 AcubeSAT

The project has been a part of the European Space Agency's Fly Your Satellite! initiative since February 2020, a dedicated programme that allows selected student teams to design and fly their own satellite, mostly through training and financial support. SpaceDot's nanosatellite[36] will have a pressurised vessel manufactured in-house that will house a custom-made miniature imaging system and a lab-on-a-chip. In order to investigate the combined impacts of cosmic radiation and microgravity conditions in low earth orbit, the platform is being used to multiplex yeast Saccharomyces cerevisiae cultivation and analysis. The yeast cells are genetically altered to elicit fluorescence during the expression of a gene of interest in order to achieve that experimental purpose. Fluorescence intensity captures changes in gene expression, which are then quantified. During an extended period of 6 to 9 months in orbit, our studies will study genes on a scale up to 100-200 times larger than past missions, while also providing high-quality visual views.Our technology is built from the ground up to be modular, allowing it to be reused in space biology research with

little resources, know-how, and time, potentially making the field more accessible to labs and organisations all over the world.

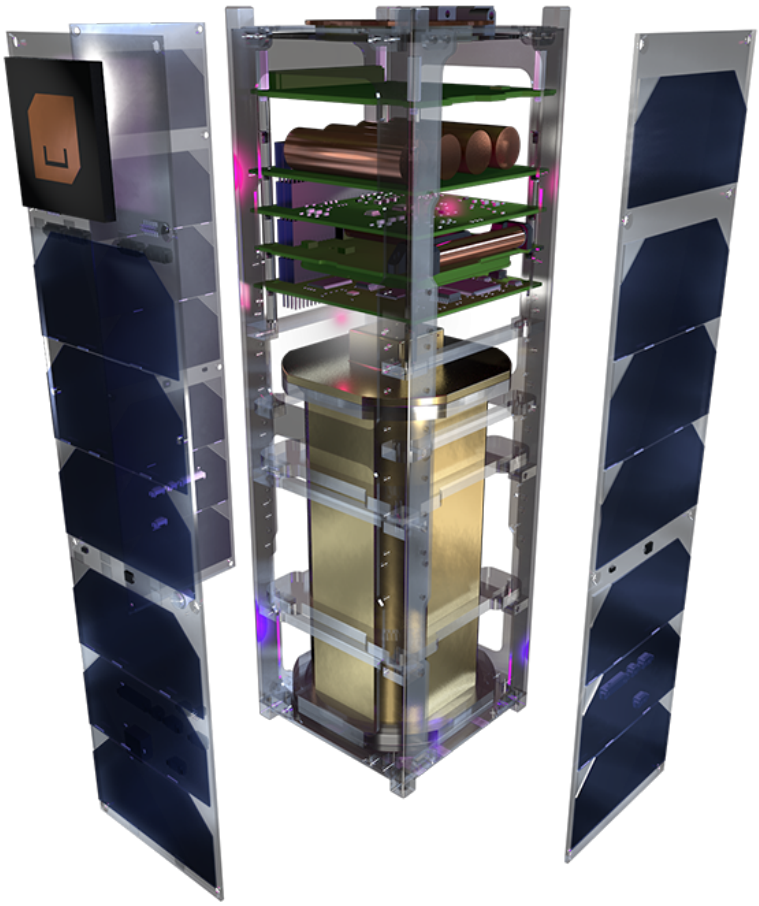

Figure 2.1: AcubeSAT mock-up

From the mission objective stated before [7], the TRA subsystem is responsible for the mission analysis aspects of this endeavor. According to the mission description, the subsystem proposed that a LEO should be considered to be able to compare the data on a human sized level. Due to the lack of a propulsion system, a LEO is the best option for the mission in order to meet the criteria of a maximum life duration of 25 years, according to guidelines set by the European Space Agency [2]. As a result, the baseline orbit will be a sun-synchronous orbit. The ability to choose the shortest eclipse time and the orbit's life length is advantageous to the mission's efficiency. Finally, a range of orbits will be shown, together with a preliminary study demonstrating that they are compatible with the mission. Of course further info is presented in the official document of the CDR in Mission Analysis Appendix.

2.2.1 Physical Architecture

At a high level, the physical architecture of AcubeSAT can be split into three distinct main items, namely:

1. Subsystem Stack

2. Payload Container
3. Spacecraft Frame

The **Subsystem Stack** houses all subsystem boards, with the exception of the payload PCB. Both in-house developed boards (*OBC/ADCS board*) and COTs boards (*EPS, COMMS and MTQ board*) follow the mechanical properties of the PC/104 Standard[19]. A view of the Subsystem Stack can be found in Figure 2.2.

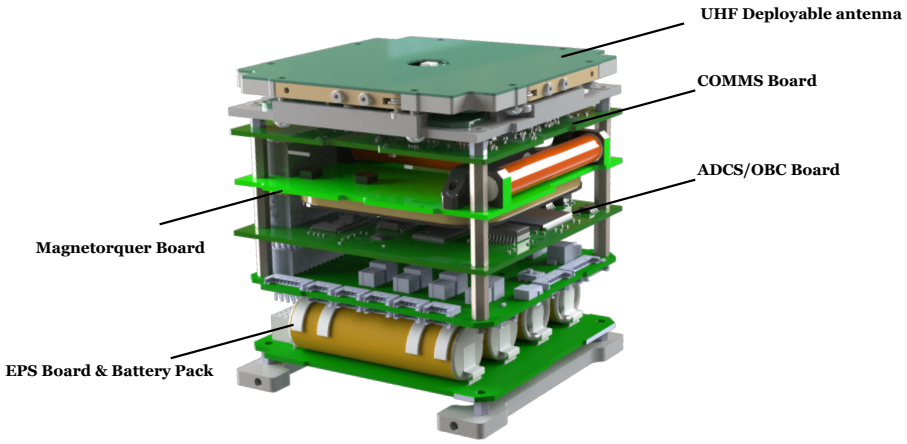

Figure 2.2: Render of the assembled Subsystem Stack

The **Payload Container** houses the microfluidic chip, where the experiment will be conducted, and all supporting components including the Payload PCB. All components inside the payload container are fixed using a structure called *unibody*. A picture of the unibody can be seen in Figure 2.3. The unibody slides in the payload container and then the payload container is then sealed by closing the lid on the -Z face of the payload container.

On the opposite face of the payload container, a mount houses the reaction wheel of the spacecraft. The vacuum feedthrough, which enables power and data to be transmitted to the payload from the subsystem stack and vice versa, is on the +Z face of the payload container as well. In the future, pressure valves in order to pressurize the payload container to 1.2 atm will also exist on that side.

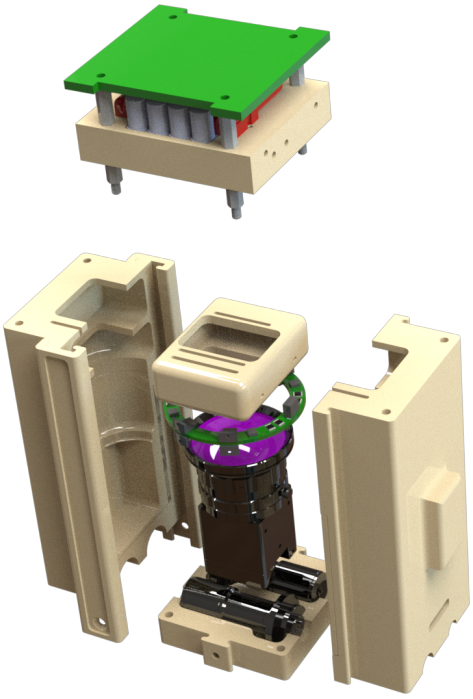

Figure 2.3: Render of the unibody inside the payload container (exploded view). The SU Board and the valve mounting interface can also be seen.

Both the Subsystem Stack and the Payload container are then mounted inside the **Spacecraft Frame**. After all necessary connections inside the frame have been made, the solar panels are mounted on the frame, completing the architecture of the space segment. The interconnection of all the different parts can been in Figure 2.4.

2.2.2 Physical Architecture Diagram

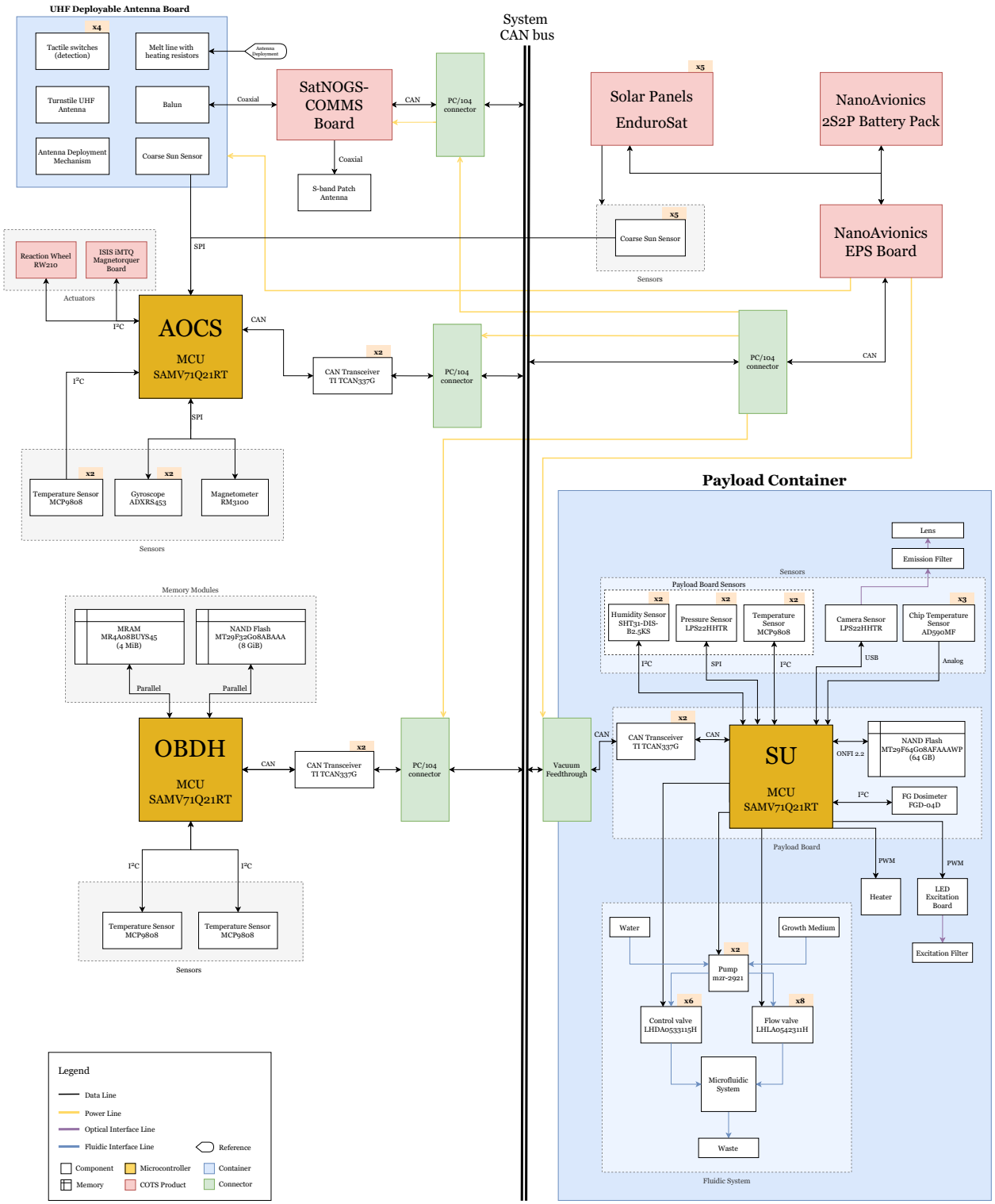

Figure 2.4: AcubeSAT Physical Architecture[19]

3. Orbital Mechanics and Definition

3.1 Keplerian motion model

The Keplerian motion model appears as a solution to the two-body problem. Bodies are considered as material points isolated from other bodies and any other influences. They move only under the influence of mutual attraction according to Newton's law of squares of reciprocal distances. Such a motion is also called unperturbed motion[8].

We consider the equations of motion of the two-body problem with masses m_1 and m_2 in an arbitrary non-rotating systemof rectangular coordinates x, y, z. The origin of the coordinate system O is located either in the first body, or in the second, or in the barycenter of the system. For all three cases, the equations of motion will have the form [35]:

$$\frac{d^x}{dt^2} = -\frac{\mu x}{r^3} \tag{3.1}$$

$$\frac{d^y}{dt^2} = -\frac{\mu y}{r^3} \tag{3.2}$$

$$\frac{d^z}{dt^2} = -\frac{\mu z}{r^3} \tag{3.3}$$

where $r = \sqrt{x^2 + y^2 + z^2}$ and μ is a constant called the gravitational parameter. The equations of motion of the second body relative to the barycenter have the same form, but the gravitational parameter in this case is given by the equation:

$$\mu = G\frac{m_1^3}{(m_1 + m_2)^2} \tag{3.4}$$

The trajectory of motion in the two-body problem in the orbital coordinate system is described by the following relation:

$$\mu * r = c^2 - f * \xi \tag{3.5}$$

The degenerate case of rectilinear motion in the two-body problem, when the constant of the area integral c is zero, we do not consider. Here we assume that $c > 0$, and consider the equation of the trajectory in polar coordinates.

We introduce the polar coordinates of the object r and v in the orbit plane using the formulas

$$\xi = r\cos v\eta = r\sin v \tag{3.6}$$

where the angle v in the Keplerian motion is called true anomaly and is counted from the pericenter in the positive direction of the point. The focal equation of the orbit in polar coordinates has the form

$$r = \frac{p}{1 + e\cos v} \tag{3.7}$$

The change in the polar angle v in time is described by the differential equation

$$(\frac{p}{1 + e\cos v})^2 \frac{dv}{dt} = c \tag{3.8}$$

3.1.1 Keplerian Elements

An orbit can be expressed by the sum of six variables. The collection of these parameters together can be defined as the Keplerian elements. In the following Figure 3.1 there is a visualization of an orbit, where the definition of each variable can be further analyzed:

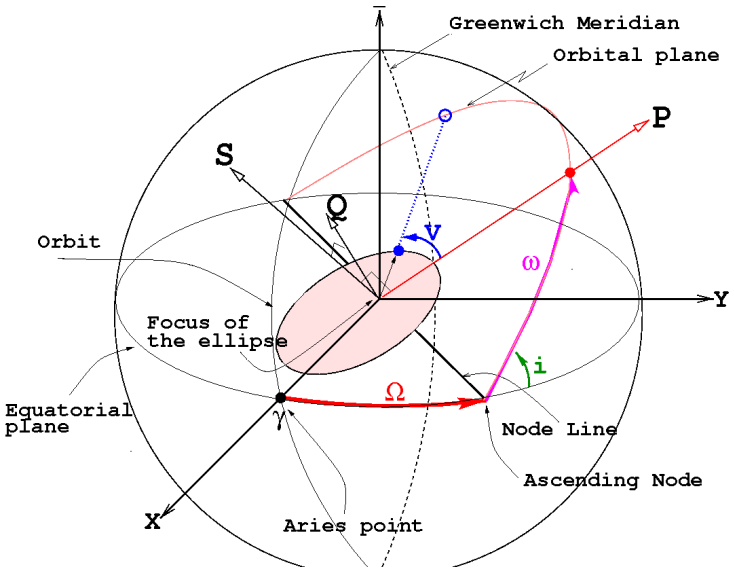

Figure 3.1: Keplerian sphere

- eccenticity (e): since the orbit is the shape of an ellipse, this value is utilized to measure the elongation
- semi-major axis (a): from the ellipse can be defined as: $\frac{c+b}{2}$: where b and c is the periapsis and apoapsis distances, respectively.
- inclination (i): defined as the vertical tilt of the ellipse with respect to the reference plane, measured at the ascending node.
- Longitude of the ascending node (Ω)
- Argument of periapsis (ω): defines the orientation of the ellipse
- True Anomaly (θ) at an epoch defines the position of the the mass and a certain time (t_0), which is the epoch.

3.2 Low Earth Orbit

Low-Earth Orbit (LEO) is an orbit with altitude ranging from 200–300 km to 1600 km. In LEO, particles of different origin are encountered: protons, electrons, heavy ions, neutrons, and others. LEO's close proximity to Earth makes it useful for several reasons. It is the orbit most commonly used for satellite imaging, as being near the surface allows it to take images of higher resolution [39].

Objects that are in a low-Earth orbit are subject to atmospheric drag since they are still within the upper layers of Earth's atmosphere – specifically the thermosphere (80 – 500 km; 50 – 310 mi), theremopause (500–1000 km; 310–620 mi), and the exosphere (1000 km; 620 mi, and beyond). The higher the object's orbit, the lower the 1atmospheric density and drag.

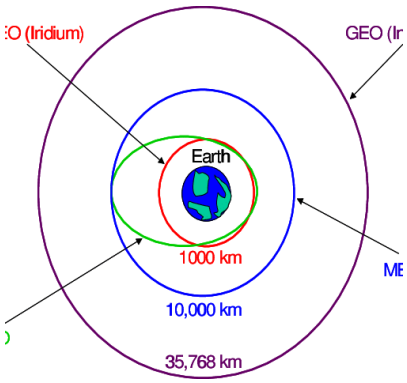

Figure 3.2: Space Regions

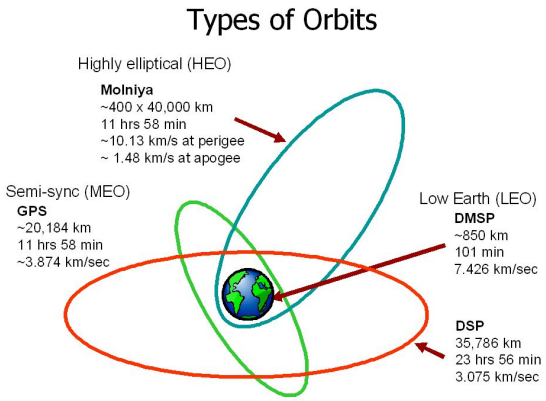

Figure 3.3: Types of Orbits

Objects that are in a low-Earth orbit are subject to atmospheric drag since they are still within the upper layers of Earth's atmosphere – specifically the thermosphere (80 – 500 km; 50 – 310 mi), theremopause (500–1000 km; 310–620 mi), and the exosphere (1000 km; 620 mi, and beyond). The higher the object's orbit, the lower the 1atmospheric density and drag.

3.3 Sun Synchronous Orbit

A sun synchronous orbit (***SSO***, or as it is also called *Heliosynchronous orbit*) is a nearly polar orbit around a planet (in this case the Earth) in which the satellite passes over any given point of the planet's surface at the same local mean solar time. More technically, it is an orbit arranged so that it precesses through one complete revolution each year, so it always maintains the same relationship with the Sun.

At first, the initial altitude needs to be defined. Knowing that for an Sun-Synchronous Orbit (SSO) the precision rate should be equal to the mean motion of Earth around the Sun, which is 360^o over one year, then the Equation 3.9 is derived. Equation 3.9 shows the dependence between the initial altitude and the inclination of the orbit

$$\cos i = -\left(\frac{a}{12352 \text{ km}}\right)^{\frac{7}{2}}, \tag{3.9}$$

An SSO is achieved by having the osculating orbiting plane precess (rotate) approximately one degree eastward each day with respect to the celestial sphere to keep pace with the Earth's movement around the Sun. This precession is achieved by tuning the inclination to the altitude of the orbit so that Earth's equatorial bulge, which perturbs inclined orbits, causes the orbital plane of the spacecraft to precess with the desired rate. The plane o f the orbit is not fixed in space relative to the distant stars, but rotates slowly about the Earth's axis.

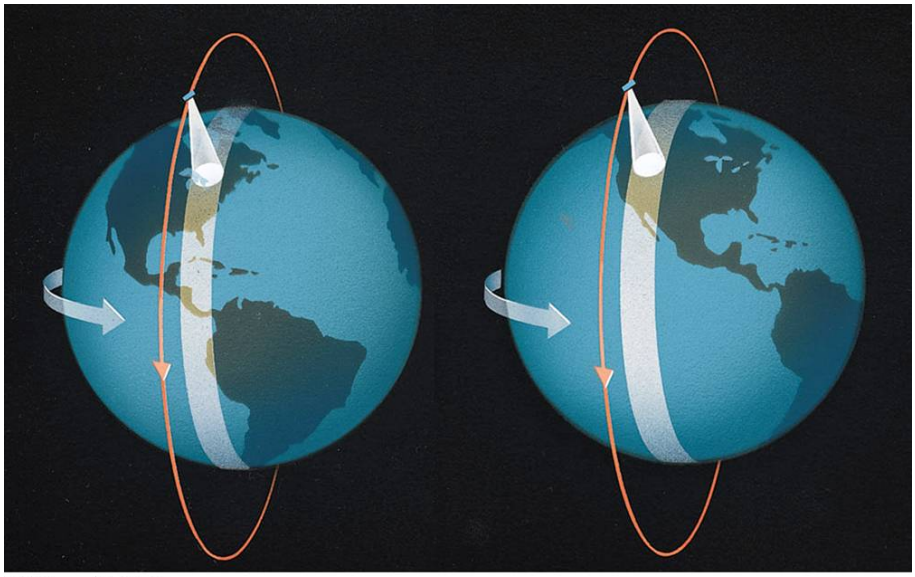

Figure 3.4: Polar Orbit Representation

Typical Sun-synchronous orbits around Earth are about 600-800 km in altitude , with periods in 96-100 minute range, and inclinations of about 98°. This is slightly retrogade compared to the direction of Earth's rotation: 0°represents an equatorial orbit, and 90°represents a polar orbit.

A SSO can place a satellite in constant sunlight, which allows the solar panels to work continually. This orbit is also useful for imaging, spy, and weather satellites, , because every time the satellite is overhead, the surface illumination angle on the planet underneath it will be nearly the same. This consistent lighting is a useful characteristic for satellites that image the Earth's surface in visible or infrared wavelengths, such as weather, and spy satellites; and for other remote-sensing satellites, such as those carrying ocean and and atmospheric remote-sending instruments that require sunlight.

Special cases of the SSOs are the *noon/midnight orbit* where the local mean solar time of passage for equatorial latitudes is around noon or midnight, and the *dusk/-dawn orbit*, where the local mean solar time of passage for equatorial latitudes is around sunrise or sunset, so that the satellite rides the terminator between day and night.Riding the terminator is useful for active radar satellites, as the satellites' solar panels can always see the Sun, without being shadowed by the Earth. It is also useful for some satellites with passive instruments that need to limit the Sun's influence on the measurements, as it is possible to always point the instruments towards the night side of the Earth. The dawn/dusk orbit has been used for solar-observing

scientific satellites , such as *Yohkoh, TRACE, HINODE* and *PROBA2*, affording them a nearly continuous view of the Sun.

4. Space Environment

There is significant level of radiation exposure for the astronauts and satellites traveling outside the Earth's magnetosphere on missions to and from the Moon or Mars in excess of those encountered on the ground. The radiation environment is presented in this section on the premise of a theoretical foundation so that the reader may have a sense of the numerous sources of radiation. As stated from the previous chapter, the region that is being discussed is LEO. The sources affecting the space environment are the following:

- Trapped Electron & Protons
- Solar Protons
- Solar Flare Protons & Ions
- Galactic Cosmic Rays

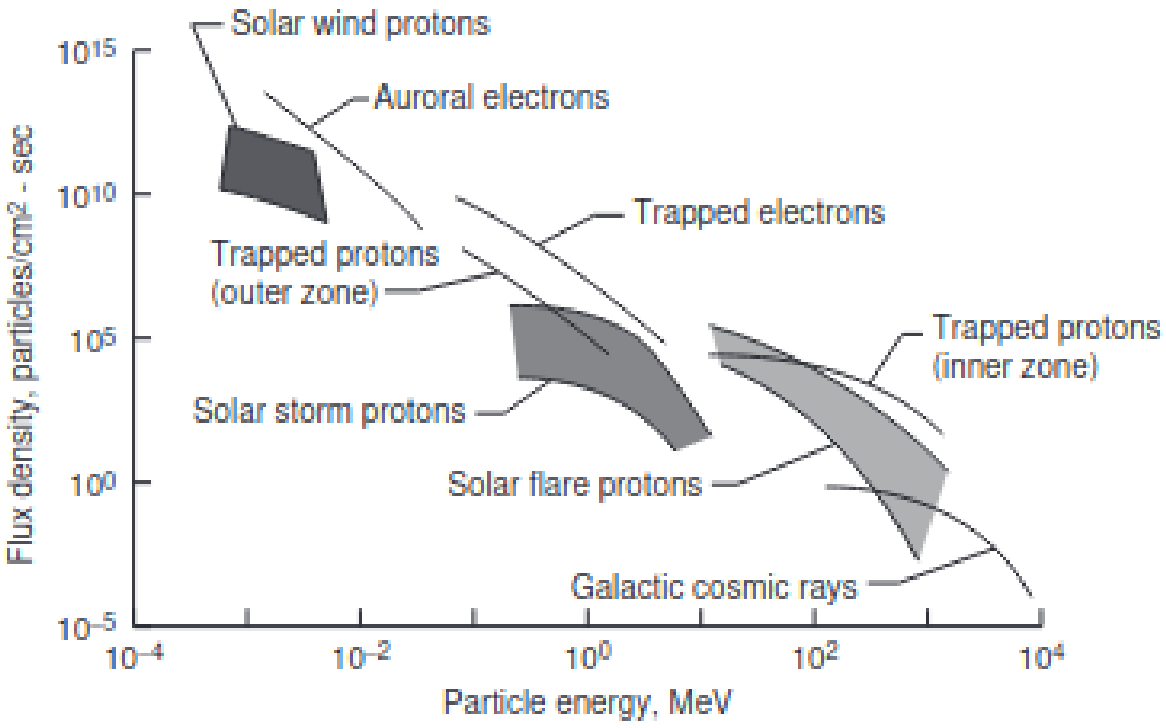

Figure 4.1: Space Radiation Sources

4.1 Space Environment

In this section, different areas of high particle fluxes are presented. The main ones that will be encountered in our mission are South Atlantic Anomaly (SAA) and the poles.

4.1.1 Geomagnetic fields

In space physics, the Earth's external magnetic field is crucial. This is due to its intense interaction with charged particles, which produces a variety of intriguing effects. The aurora's striated shape and the capture of energetic particles in the Earth's radiation belt are two examples. Furthermore, the magnetic field has a significant impact on the ionosphere's conductivity, as do critical solar-terrestrial relationships based on the interaction of the solar wind with the magnetosphere.

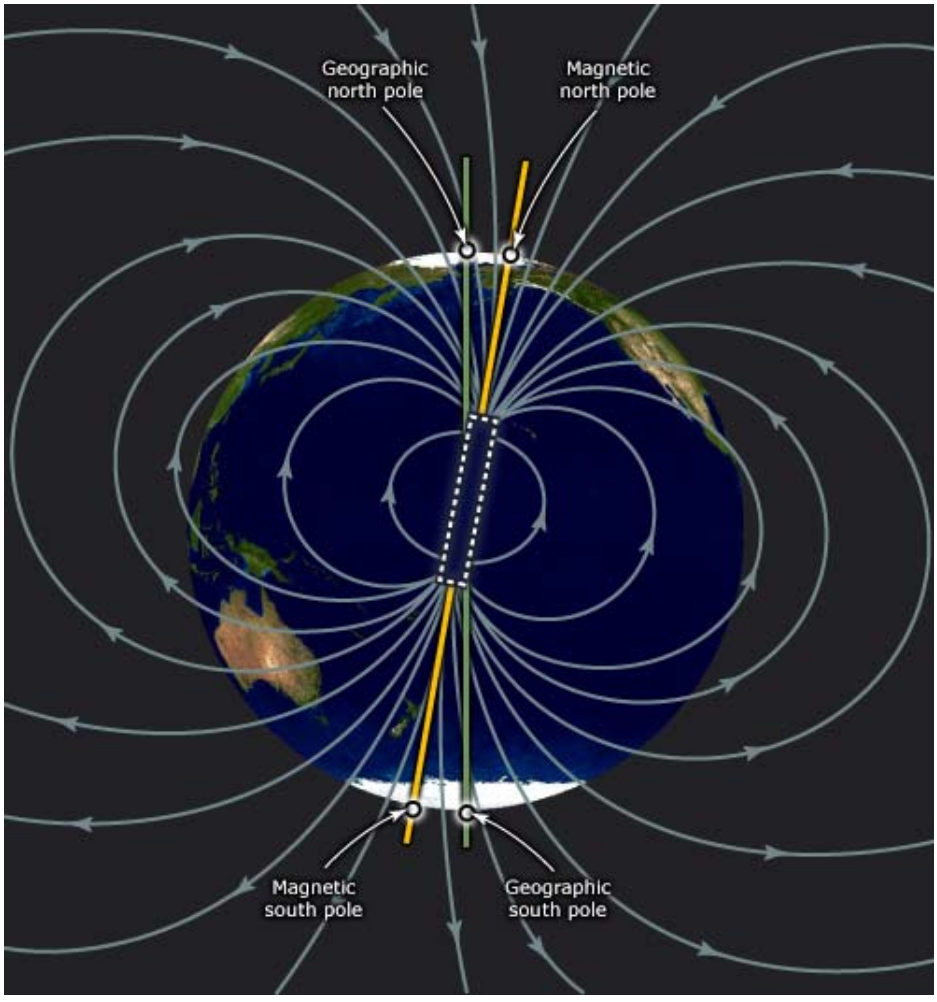

Figure 4.2: Earth's magnetic field lines

The magnetic inclination or dip equator is the point where the field direction is completely horizontal, i.e. where the inclination or dip angle with respect to the Earth's surface is zero. The magnetic inclination or dip poles are the two spots on the Earth's surface where the magnetic field is precisely perpendicular to the

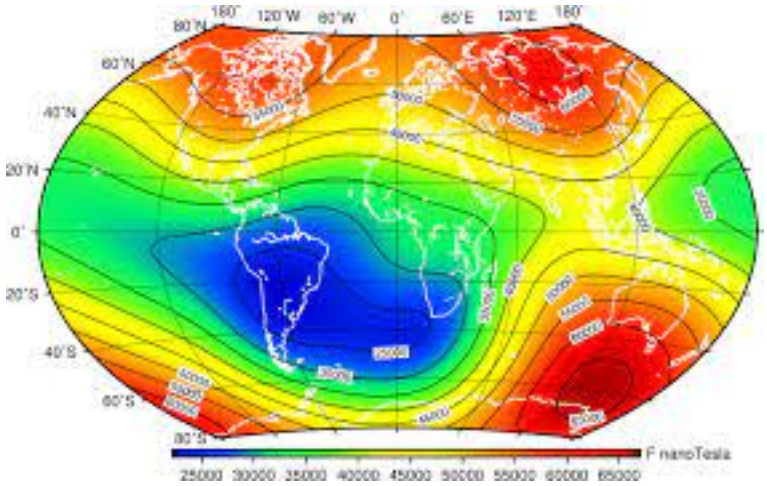

Figure 4.3: Earth's magnetic intensity[41]

surface. The boreal pole (BP) in the Northern Hemisphere (which is magnetically a south pole because the field points into the Earth!) and the austral pole (AP) in the Southern Hemisphere (which is magnetically a north pole because the field points away from the Earth) are distinguished here.

$$B_\theta = \frac{\mu_0 \mathcal{M}}{4\pi} \frac{1}{r^3} \sin\theta \tag{4.1}$$

$$B_r = \frac{2\mu_0 \mathcal{M}}{4\pi} \frac{1}{r^3} \cos\theta \tag{4.2}$$

$$B_\lambda = 0 \tag{4.3}$$

where $\mathcal{M}$ denotes the magnetic dipole moment and $\mu_0 = 4\pi * 10^{-7}$ Tm/A is the magnetic permeability in vacuum. The dipole moment evidently characterizes the intensity of the dipolar magnetic field.

An equation for a dipole field line is needed to calculate particle trajectories in the geomagnetic field. This can be deduced from the fact that magnetic field lines must be co-aligned with the direction of the magnetic field at all times[20].

$$\frac{r d\phi}{dr} \sim \tan a = \frac{B_\phi}{B_r} = \frac{-1}{2} \frac{\cos\phi}{\sin\phi} \tag{4.4}$$

Separation of variables and using the substitution $x = \cos\phi$, we obtain the differential equation

$$\frac{dr}{r} = 2\frac{dx}{x} \tag{4.5}$$

with the solution

$$r = \frac{r_1}{\cos^2\phi_1} \cos^2\phi \tag{4.6}$$

Introducing the shell parameter L, defined as the geocentric distance of a field line in the geomagnetic equatorial plane measured in units of Earth radii, the equation for a field lien assumes the following expression:

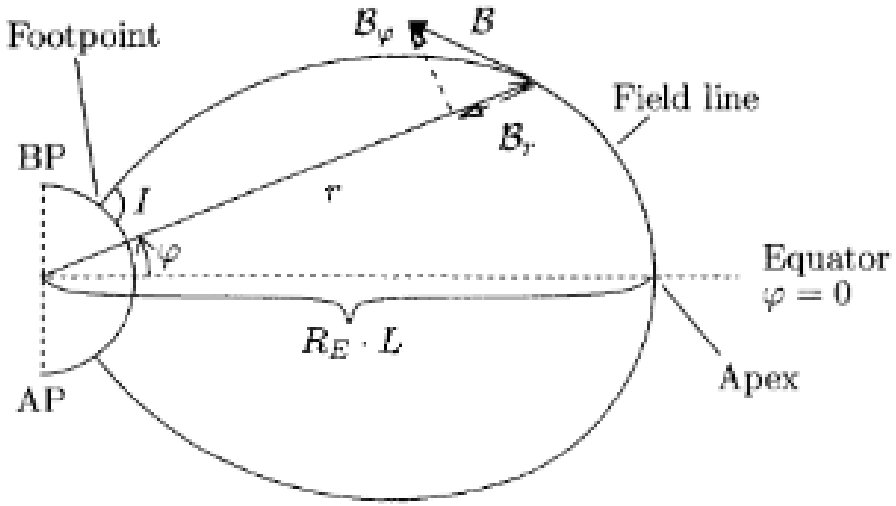

Geomagnetic poles:	BP (79°N, 290°E)
	AP (79°S, 110°E)
Horizontal component:	$\mathcal{B}_\varphi = \mathcal{B}_{00}\ (R_E/r)^3\ \cos\varphi$
Vertical component:	$\mathcal{B}_r = -2\ \mathcal{B}_{00}\ (R_E/r)^3 \sin\varphi$
Intensity:	$\mathcal{B} = \mathcal{B}_{00}\ (R_E/r)^3 \sqrt{1+3\sin^2\varphi}$
with	φ = geomagnetic latitude
	$r(\geq R_E)$ = geocentric distance
	$\mathcal{B}_{00} = \mu_0\ \mathcal{M}_E/(4\pi\ R_E^3) \simeq 30\mu\mathrm{T}$
Field line equation:	$r(\varphi) = L\ R_E\ \cos^2\varphi$
Shell parameter:	$L = r(\varphi = 0)/R_E$
Footpoints:	$\varphi(R_E) = \arccos\sqrt{1/L}$
Inclination:	$I = \arctan(2\tan\varphi)$
Declination:	$D = -\arcsin(\cos\varphi_g^{BP}\ \sin(\lambda_g - \lambda_g^{BP})/\cos\varphi)$
Curvature:	$\rho_c = \mathcal{B}/\lvert\nabla_\perp \mathcal{B}\rvert$

Figure 4.4: Geocentric dipole approximation of the geomagnetic field [20]

$$r = L * R_E * \cos^2 \phi \tag{4.7}$$

4.1.1.1 Geomagnetic Shielding (Størmer's theory)

Geomagnetic shielding is the effect of the Earth's magnetic field partially protecting near- Earth space from solar energetic particles and cosmic rays. These particles, on the other hand, can readily reach the polar regions and great altitudes like the geostationary orbit.

There are minimum cutoff energies required for ions to penetrate to a specific point in the field. Based on the geomagnetic R, coordinates of the point and the angle of ion arrival from east, Størmer's theory[7] yields a cutoff stiffness, P_c, for particle arrival at a point.

$$P_c = \frac{M \cos^4 \lambda}{R^2[1 + (1 - \cos^3 \lambda \cos \gamma)^{1/2}]} \tag{4.8}$$

M is the normalized dipole moment of the Earth. From this equation, it can be seen that cosmic rays penetrate the geomagnetic field more easily from the west ($\gamma = 180°$) than from the east ($\gamma = 0$). For vertical arrival, Equation 4.8 simplifies to:

$$P_c \sim \frac{16 \cos^4 \lambda}{R^2} = \frac{16}{L^2} GV \tag{4.9}$$

4.1.2 Van Allen Belts

Energetic electrons and ions are magnetically trapped around the Earth forming the radiation belts, also known as the Van Allen belts. The radiation belts extend from 100 km to 65000 km and consist mainly of electrons of up to a few MeV energy and protons of up to several hundred MeV energy. The high energy particle flux in the radiation belts is dependent on the solar activity.

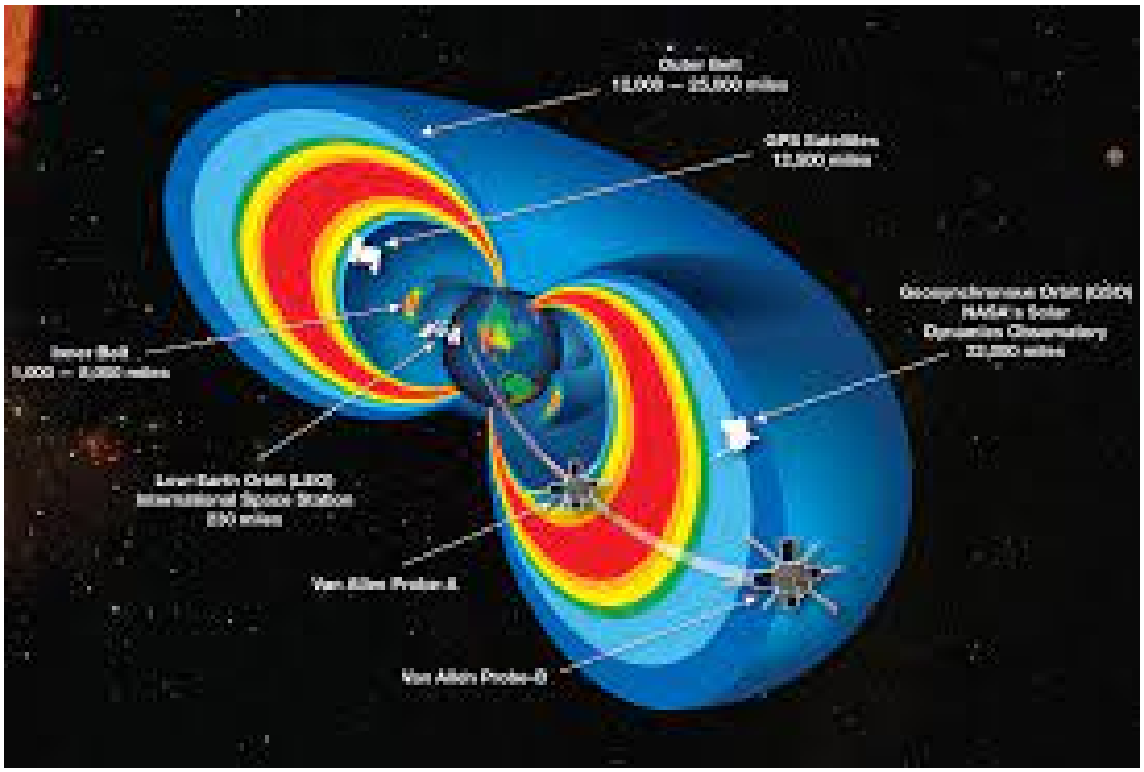

Figure 4.5: Van Allen Belts

As small outline of the Van Allen Belts. They consist of two regions, which from the plane of the equinox the regions can be depicted as a torus, where the hole is the Earth. They have a mean distance of 1.5 and 6 RE. The internal region Van-Allen is inside theplasma-sphere and the external one is outside of it. The plasma-sphere plays a vital role in the formation of the boundary between the two regions. Both regions consist of highly energetic protons and electrons. Although it should be noted, that the energies of the particles are different between the external and the internal regions as they depend on the distance from the Earth.

There are many ways of charged particles being trapped in the belts. The first one being through immediate trapping from the magnetic field of solar particles. The second one and more prevalent is the beta decay of atmospheric neutrons, formed by the interaction of cosmic ions with the Earth's atmosphere, also known as CRAND. Those also called albedo neutrons and are decayed in free protons:

$$p \rightarrow \pi^0 + \pi^- + \pi^+ + nn \rightarrow p^+ + e^- + \vec{\nu_e} \tag{4.10}$$

4.1.2.1 Phenomenology

The charged particles interact with the magnetic field with the Lorentz force, resulting in a helical movement.

$$F_{mag} = q(\vec{v}x\vec{B}) \tag{4.11}$$

The acceleration is vertical to the velocity, resulting to the spiral case.

$$\frac{d(\gamma m\vec{v}}{dt} = q(\vec{v}x\vec{B}) \tag{4.12}$$

For the magnetic field, the acceleration is resulted in:

$$\gamma m_0 \frac{d\vec{u}}{dt} = ze(\vec{v}x\vec{B}) \tag{4.13}$$

As already know only the vertical component of the velocity is the only one affected by the magnetic field B and assuming that the magnetic field in small distances is constant we can assume a circular movement:

$$zev_{ver} = \frac{\gamma m_0 v_{ver}^2}{r} \rightarrow R = B * r = \frac{p_{ver}}{z * e} \tag{4.14}$$

The classification of particles can be shown in the following listing:

- Stably-trapped
  - Outside drift loss cone
  - Tracing: .= drift cycle, in both directions
  - Adiabatic invariant conservation check
  - $\tau_{gyration} << \tau_{bounce} << \tau$ drift, where τ is the period associated to each kind of motion
- Quasi-trapped
  - Inside drift loss cone & outside bounce loss cone
  - Tracing: intersection with atmosphere(100km) before completing 2 full drift cycles, in both directions
  - Third adiabatic invariant violated
- Un-trapped
  - Inside bounce loss cone
  - Tracing: intersection with atmosphere before completing full bounce cycle, including both directions
  - All adiabatic invariant violated/chaotic trajectories

4.1.3 South Atlantic Anomaly

South Atlantic anomaly is the inner edge of the inner radiation belt encountered in low altitude orbits below 800km. The offset between the rotational axis and the magnetic axes, result in a tilted magnetic field bringing the inner belt to its lowest altitudes in the South Atlantic region. In the South Atlantic Anomaly (SAA) the most energetic particles of the Van Allen Belts are found due to their invasive nature. The region consists mainly of trapped protons of <300 MeV and is the dominant contributor in radiation doses in this region, since the fluxes of Galactic Cosmic Rays (GCR) and Solar Energetic Particles (SEP) are reduced by the Earth's magnetic Field.

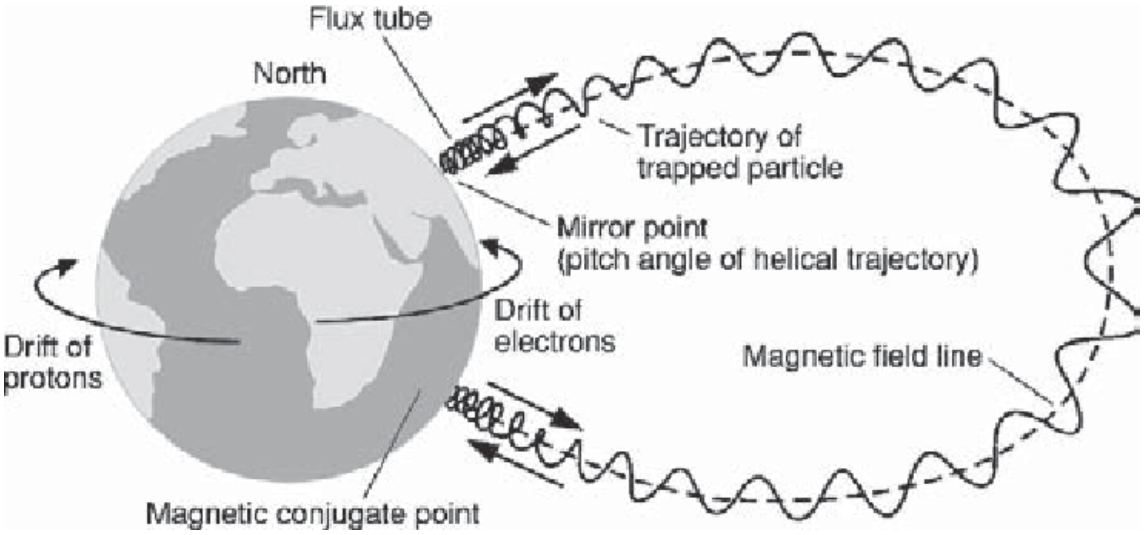

Figure 4.6: Motion of trapped charged particles in the geomagnetic field[11]

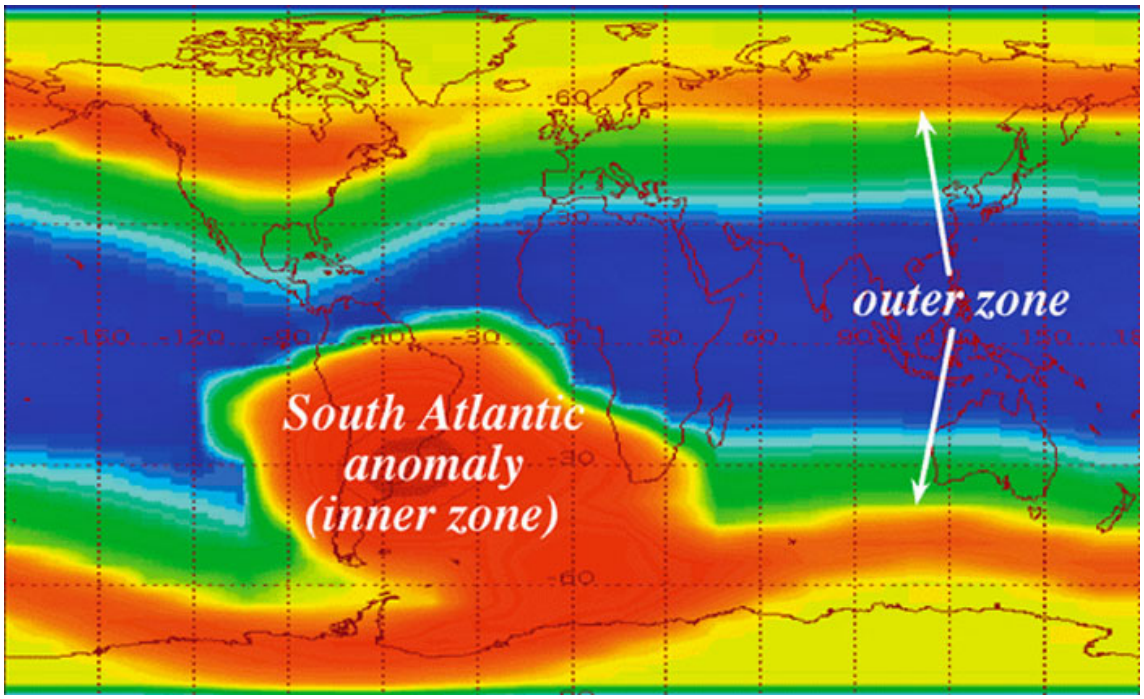

Figure 4.7: South Atlantic Anomaly

4.1.4 Poles

Poles are defined as the high latitude parts of the Earth and are the beginning and the termination of Earth's magnetic field. Due to their high magnetic intensity, these areas are recognised by their high flux radiation environment since the electrons trapped by the Earth's magnetic field are situated there. Furthermore, on the high latitude parts of the orbit, a spacecraft is exposed to almost unattenuated fluxes of Galactic Cosmic Rays (GCR) and Solar Energetic Particles (SEP) as the geomagnetic shielding is at its lowest.

4.2 Sources of Radiation

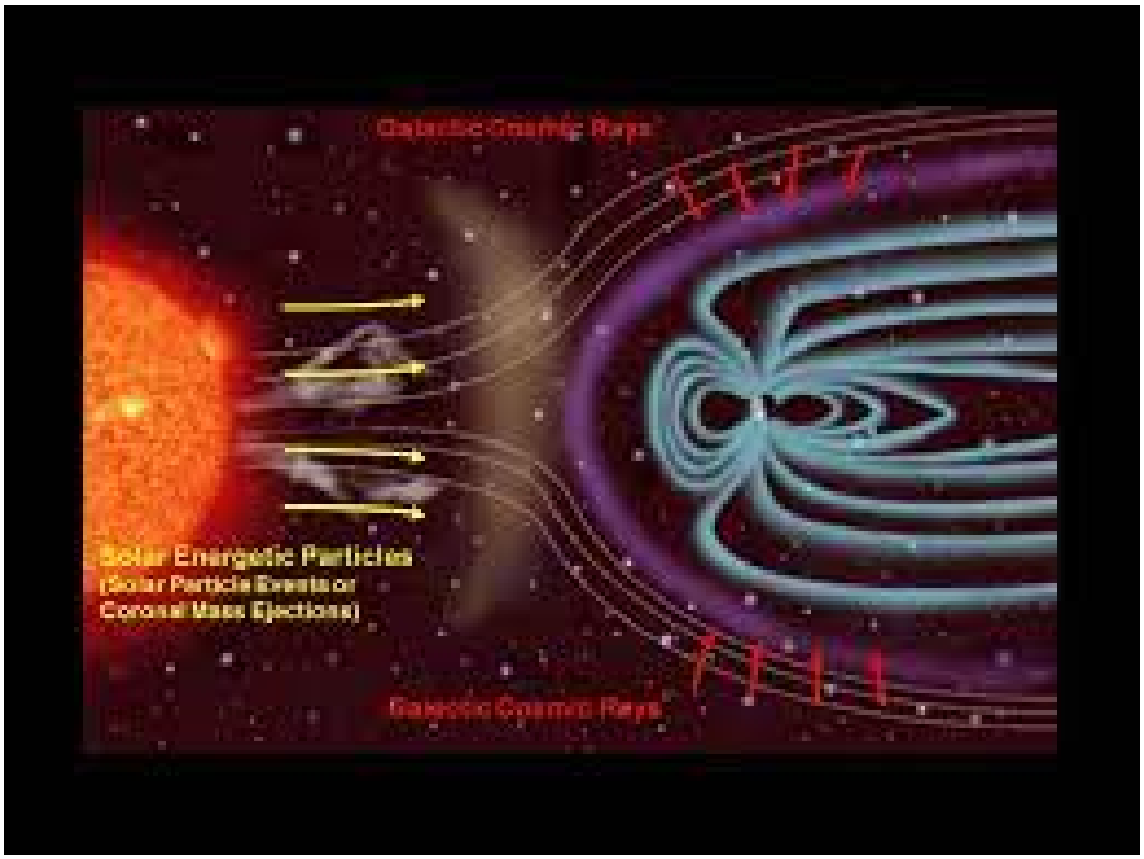

Figure 4.8: The three principal sources of space radiation: (1) galactic cosmic rays, (2)trapped particles in the ERBs and (3) solar particle events.

4.2.1 Trapped Particles

The Earth is surrounded by intense regions of energetic protons and electrons referred to as Earth's Radiation Belts (ERBs). The charged particles revolve around a geomagnetic field line in what is called cyclotron motion[5].Finally there is a drift of the protons to the west and of the electrons to the east[7].

Trapped radiation belt charged energetic particles in the geomagnetic field with a gyration period and radius are:

$$t_c = \frac{2\pi m}{eB} \tag{4.15}$$

$$R_c = \frac{mv}{eB} \tag{4.16}$$

Trapped electrons occur in two belts or zones.The first, inner zone extends to about 2.4 Earth radii (R_E) and consists mostly of electrons with energies less than 5 MeV. The second or outer zone extends from about 2.8 to 12 R_E[4],[7] and contains electrons with energies up to about 7 MeV. The gap between the inner and outer electron belts is referred to as the slot region. Electron ¯flux is about an order of magnitude greater in the outer zone than in the inner zone.

Trapped protons occur in only a single region that decreases in intensity as a function of distance from the Earth. Trapped protons extend in energy from several to several hundred MeV and form a broad peak between 150 and 250 MeV. The majority of the trapped proton are situated in the inner region of the van allen belt.

Table 4.1: Trapped particles properties [5]

	Earth's radiation belts
Primary Composition	Electrons <6 MeV
	Protons <250 MeV
Effect of solar cycle	Solar cycle affects atmospheric scale height
	East/west anisotropy
	Creation of temporary belts during solar max
Effect of geomagnetic field	Raison d'etre
	South Atlantic Anomaly
Effect of spacecraft's shielding	Electrons fully attenuated, some production of Bremsstrahlung
	Attenuation of low-energy protons
	Target fragmentation by high-energy protons
Relative contribution in LEO	Dominates for low-inclination, high- altidtude orbits
	50% of ISS dose

The first environment of radiation source are trapped protons and electrons stemming from the Earth's magnetic field. Regarding the electrons and protons, [7] is used. From the aforementioned standard the following models were used, the AE8[32] for electrons and AP8[25] for protons along with the standard Jensen Cain magnetic field model, which includes a customizable energy grid. We can extract:

- the *instantaneous flux* at a single energy.
- the *instantaneous energy* spectrum along the orbit.
- the *proton peak* at an energy.

Particularly, the trapped particle models used are compatible with [7] and calculate maximum and minimum flux in two different ways:

- differential calculation
- integral calculation

4.2.1.1 East-West Effect

Particles arriving from the west have gyrated from a higher altitude, while those arriving from the east have gyrated from a lower altitude, due to the inclination of geomagnetic field lines with regard to the atmosphere here.Because of atmospheric absorption, there are fewer coming from below, resulting in an asymmetry in fluxes.

4.2.1.2 Pitch-angle distribution

At low altitude, the directional distribution of trapped particles peaks perpendicular to the magnetic field direction. This is due to the absorption of particles having a large parallel component in the atmosphere when they gyrate to lower altitudes. Through transformations, radiation belt models with particle fluxes represented in geomagnetic coordinates can easily be used to infer the directional distribution ("pitch angle distribution")[27].

4.2.2 Solar Particle Events

4.2.2.1 Solar Protons

In low-Earth orbits, solar energetic particles are the third source of charged particles. The number of SEP occurrences and their frequency are determined by solar activity. Almost all of the events take place within a seven-year window around the solar maximum. The annual number of SEP occurrences, N, is a power function of W, the sunspot number[20]:

$$N = 0.178 * W^{0.75} \tag{4.17}$$

Table 4.3: The space radiation environment in LEO and interplanetary space []

	Solar particle events
Primary Composition	Low Energy protons and electrons Some heavy ions
Effect of solar cycle	Frequency and magnitude of SPE proportional to solar cycle
Effect of geomagnetic field	Protection in LEO due to cut-off Rigidity, function of geomagnetic latitude
Effect of spacecraft's shielding	Low-energy protons attenuated Higher-energy protons and ions interact with the shield atoms
Relative contribution in LEO	More severe in higher-inclination orbits Unknown contribution to ISS Dose

Furthermore, Solar Energetic Particles are high-energy particles emitted from the Sun, which consist of protons, electrons and High Atomic number and energy elements ions. Their energy ranging from a few tens of kilo electron volt to many Giga electron volt. Regarding the solar particles, fluences that were used (Energetic Solar Protons[9] model for the protons and Psychic model for the ions) are also compatible with the [7] standard, having a 95% confidence level for the protons and a solar active period for the entire duration of the simulation, being one year. This particular model includes a magnetospheric cutoff (Størmer[26] model) on Earth's shadow with a quite condition. By running the simulations, we calculated the mean values of both flux and fluence.

It is based on an explicit formula[7] for the probability of exceeding a given fluence ϕ of protons with energy above E, over a duration T:

$$F(\phi, T|\Phi_{RV}(E), \Phi_{muon}(E)) = \frac{1}{\sigma\sqrt{2\pi}} \int_0^{\inf} \frac{1}{x} exp(-\frac{1}{2\sigma^2}[\ln x - \mu]^2)dx \tag{4.18}$$

with

$$\sigma^2 = \ln 1 + \Phi_{RV}/T \tag{4.19}$$

and

$$\mu = \ln T * \Phi_{mean} - \frac{\sigma^2}{2} \tag{4.20}$$

Where Φ_{RV} and Φ_{mean} are respectively the relative variance and the mean of 1 year averaged proton fluence at 1 AU in the corresponding energy range.

4.2.2.2 Solar Flares

Solar flares have a very intense release of radiation in space, which can be originated by the sudden change of the Sun's magnetic field. The frequency of these sudden changes can be correlated to the Sun's eleven year cycle. Solar flares are usually accompanied by Coronal Mass Ejections, which are huge fluxes of highly energetic particles. For the Solar Flare Particle models, two models are used since there is source of both protons and ions. The model for the protons is Worst Day October 1989, which is derived from the aforementioned date and is compatible with the [7] standard. For ions, we use the model CREME96 Worst Day, which is also compatible with the [7] standard.

4.2.2.3 Solar Cycles

We now know that the sun goes through a periodic cycle in which many characteristics of its activity cycle in a predictable pattern. The size and number of sun spots and solar flares are two examples of synchronised correlations. Given how damaging the latter can be to satellites, it's easy to see why solar cycle projections have become an important aspect of space mission planning. In fact, the sun's most concerning and immediate influence is solar radiation pressure, which has the ability to modify an orbit. Strong radiation causes stronger orbital decay, as a general rule.

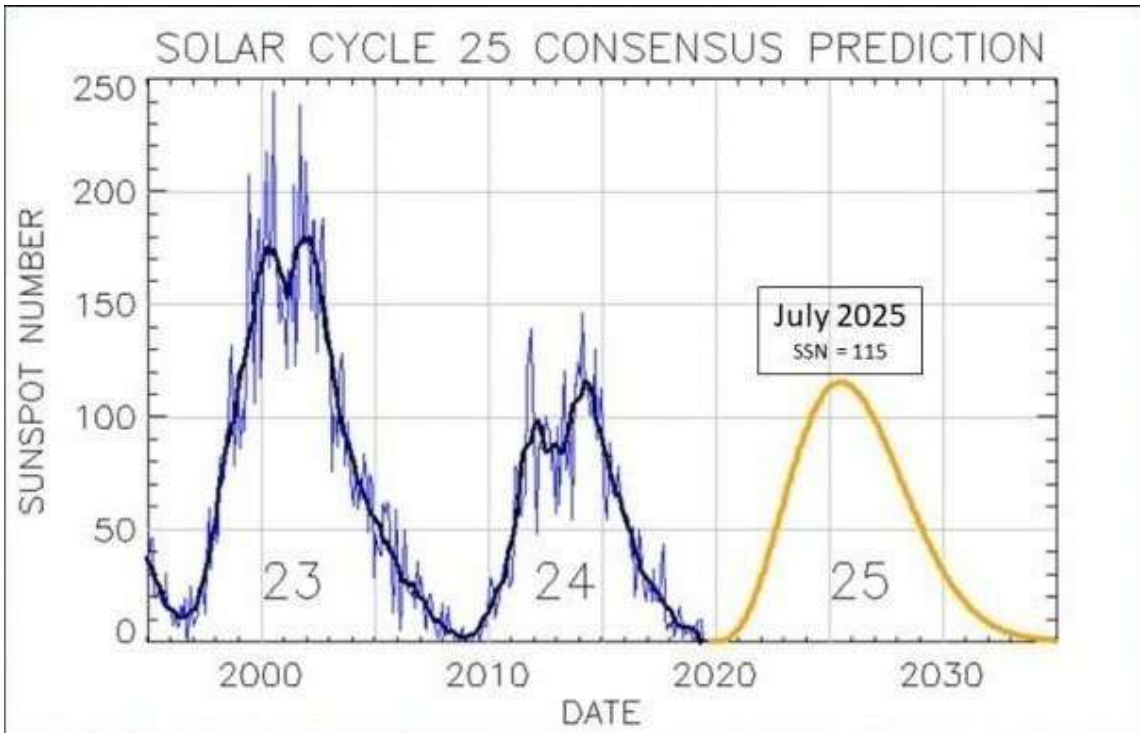

Figure 4.9: Solar Cycle 25th prediction

4.2.3 Galactic Cosmic Rays

Cosmic rays from beyond our solar system are known as galactic cosmic rays (a region extending nearly 100 AU from the sun). The GCR comprises particles with energies ranging from a few MeV/nucleon to almost 1015 MeV/nucleon, but hydrogen, helium, carbon, neon, oxygen, silicon, and iron nuclei account for the vast bulk of absorbed radiation and equivalent dose rate. Relativistic iron nuclei have a flux that is roughly 10,000 times lower than hydrogen nuclei.

GCRs are high-energy charged particles that enter the solar system from the outside and whose flux is altered in anti-correlation with solar activity due to the solar wind. Protons, electrons, and completely ionised nuclei make up these particles. The stream of Galactic Cosmic Ray (GCR) ions is constant and isotropic. GCRs contain energetic heavy ions that can deposit considerable quantities of energy in sensitive volumes and cause issues for spacecraft electronics and humans in orbit, despite the flux being low (a few particles cm -2 s -1). In the case of solar particles, the Earth's magnetic field shields near-Earth regions from these particles to variable degrees. Galactic cosmic rays are charged particles that originate from sources beyond our solar system. The distribution of GCRs is believed to be isotropic throughout interstellar space.

The differential energy spectrum according to Mewaldt[16], $j(Z, E, t, r, \theta, \phi)$ can be expressed in terms of seperate terms:

$$j = j_0(Z, E) * F_t(Z, E, t) * F_r(Z, E, t) * F_\theta(Z, E, t) * F_\phi(Z, E, t) \tag{4.21}$$

where $j_0(Z, E)$ is the local interstellar spectrum of a particle with charge Z, and the four terms $F(Z, E, t)$ are the time-,radial-,heliolatitude- and heliolongitude-

dependent functions, respectively. The flux of GCR particles is dependent on the solar activity. The flux of GCR is at its minimum during the highest solar maximum. According to [17], the magnetic irregularities move with the solar wind, of course, with velocity v_i, so that in the fixed frame of reference there is an additional particle flux v,W of convective origin. The divergence of the total particle flux gives the accumulation at a point,yielding the Fokker-Planck or diffusion equation:

$$\frac{\partial W}{\partial t} + \frac{\partial}{\partial x_i}(W v_i) - \frac{\partial}{\partial x_i}(k_{ij}\frac{\partial W}{\partial x_j} = 0 \tag{4.22}$$

A complete numerical solutions of the Fokker-Planck equation are represented in:

$$\phi(e,t) = \frac{1}{3}\int_r^{r_B}[\frac{V(r',t)}{\kappa(r',t)}]dr' \tag{4.23}$$

where V is the solar wind velocity, K is the diffusion coefficient, and r_B is the radial extent of the heliospheric boundary.

Table 4.4: Galactic Cosmic Rays properties [5]

	Galactic Cosmic Rays
Primary Composition	98 % hadrons (87% protons, 12% a-particles, 1% heavy ions)
	2% leptons (electrons and positrons)
Effect of solar cycle	Flux inversely proportional to solar cycle
	Solar modulation affect <= 1 GeV/n
Effect of geomagnetic field	Protection in LEO due to cutoff
	Rigidity, function of geomagnetic latitude
Effect of spacecraft's shielding	Little attenuation through ionization
	Projectile and Target Fragmentation by heavy ions
	Target Fragmentation by protons
Relative contribution in LEO	Dominates for high-inclination orbits
	50% of ISS dose

Lastly, we incorporate cosmic rays into our analysis with the Galactic Cosmic Rays ISO[22] 15390 model, which is compatible with [7]. From the Galactic Cosmic Rays ISO 15390 model three options are available, for the analysis the third option that takes into account the date and duration of the mission was used. In order to be precise, we included all the elements from Hydrogen with (Z=1) to Uranium with (Z=92) and, as an environment, we included a magnetospheric cutoff (model Størmer).

4.2.4 Secondary Particles

Ionization accounts for the majority of the energy loss suffered by primary particles as they pass through a spacecraft. However, because the energies of many of these particles are sufficiently high and the amount of shielding offered by the spacecraft is sufficiently big, a fraction of these primary particles will interact with the spacecraft's constituent nuclei, producing secondary particles.

There are two types of nuclear interactions between main charged particles and spacecraft target nuclei that are significant:

- Target fragmentation
- Projectile fragmentation

According to Benton[5], "Target fragmentation occurs when a high-energy charged primary, typically a trapped or GCR proton, collides with a heavy nucleus such as an Al nucleus of the spacecraft structure.". The nuclear interaction can follow a number of different channels, creating two or more secondary particles, depending on the kinetic energy of the parent charged particle. Knockout protons, neutrons, and a-particles, as well as recoil heavy nuclei, are examples of secondaries.

When a High Atomic number and energy elements (HZE) particle collides with a target nucleus, projectile fragmentation occurs. A wide variety of response pathways are conceivable depending on the energy and charge of the original particle as well as the angle of the contact. These interactions can yield bigger projectile fragments that retain most of the kinetic energy of the parent HZE particle, in addition to producing high-energy neutrons and protons.

The secondaries generated by target and projectile fragmentation continue to traverse the spacecraft's volume and may undergo further nuclear reactions. In the case of high-energy neutrons, this is especially true. The mass of the spacecraft can be viewed as a medium in which high-energy charged particles start hadronic cascades.

5. Space Dosimetry

When radiation interacts with matter, the energy and interaction or direction (or even both) of the incident particle is altered or the particle is absorbed. The interaction is continued by one or more secondary particles. The probability of interactions to take place is characterized by the interaction coefficient, which is dependent in a particular interaction, type, energy and target material. The fundamental coefficient of interaction is the cross section.

5.1 Definition of Quantities

5.1.1 Cross Section

According to [28], cross section σ of a particular interaction, the number of incedent particles is determined by the kind and energy of the particles. It is quotient of N by Φ, where N is the mean number of interactions per target and Φ is the particle fluence.

$$\sigma = \frac{N}{\Phi} \tag{5.1}$$

The unit of σ is barn and can be defined as $1b = 10^{-28}m^2$

An incident particle of a given type and energy, can be subjected to many different and unrelated types of interaction in a target. Therefore, the total cross section is the sum of the individual cross sections σ_j:

$$\sigma = \sum_J \sigma_J = \frac{1}{\Phi} \sum_J N_j \tag{5.2}$$

where N_J is the mean value of the number of interaction type J per target by the particle fluence Φ and σ_j is the component cross section of the interaction type J.

5.1.2 Fluence

The fluence[28], Φ, is the quotient of dN by da, where dN is the number of particles incident on a sphere of cross-sectional area da, thus:

$$\Phi = \frac{dN}{da} \tag{5.3}$$

The unit is m^{-2}

The energy fluence[28],Ψ, is the quotient of dR by da, where dR is the radiant energy incident on a sphere of cross-sectional area da, thus:

$$\Psi = \frac{dR}{da} \tag{5.4}$$

The unit is Jm^{-2}.

The distributions, Φ_E and Ψ_E of the fluence and the energy fluence with respect to energy are given by

$$\Phi_E = \frac{d\Phi}{dE} = \int \dot{\Phi_E} dt \tag{5.5}$$

and

$$\Psi_E = \frac{d\Psi}{dE} = \int \dot{\Psi_E} dt \tag{5.6}$$

The correlation between Equation 5.6 and Equation 5.5 is given by:

$$\Psi_E = E\Phi_E \tag{5.7}$$

5.1.3 Flux

The flux[28], $\dot{N}$, is the quotient of dN by dt, where dN is the increment of the particle number in the time interval dt, thus:

$$\dot{N} = \frac{dN}{dt} \tag{5.8}$$

The unit is s^{-1}.

The energy flux, $\dot{R}$, is the quotient of dR by dt, where dR is the increment of radiant energy in the time interval dt, thus:

$$\dot{R} = \frac{dR}{dt} \tag{5.9}$$

There is a correlation between flux and fluence, that's why flux can be referred as fluence rate. This concept can be visualized in the following Figure 5.1:

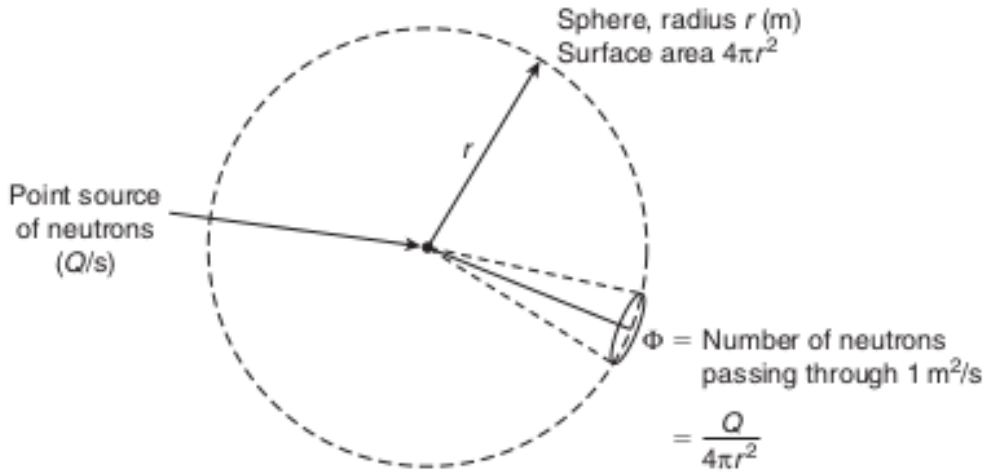

Figure 5.1: Flux from a point source [15]

The flux at a distance r is the quotient of the number of particles per second passing through an area of $1m^2$. If the source is uniformly distributed, the flux can be expressed as:

$$\Phi = \frac{\frac{dN}{dt}}{4\pi r^2} \tag{5.10}$$

5.1.4 Mass Stopping Power

The mass stopping power[28], S/ρ, of a material for charged particles, is the quotient of dE by ρ dl, where dE is the energy lost by a charged particle in traversing a distance dl in the material of density ρ, thus

$$\frac{S}{\rho} = \frac{1}{\rho}\frac{dE}{dl} \tag{5.11}$$

The unit for $\frac{S}{\rho}$ is Jm^2kg^{-1}. The mass stopping power can be expressed as a sum of independent components by:

$$\frac{S}{\rho} = \frac{1}{\rho}(\frac{dE}{dl})_{el} + \frac{1}{\rho}(\frac{dE}{dl})_{rad} + \frac{1}{\rho}(\frac{dE}{dl})_{nue} \tag{5.12}$$

where

- the first component is the mass collision stopping power due to collisions with electrons
- the second component is the mass radiative stopping power due to emission of bremsstrahlung in the electric fields of atomic nuclei or atomic electrons
- the third component is the mass nuclear stopping power due to elastic Coulomb collisions in which recoil energy is imparted to atoms

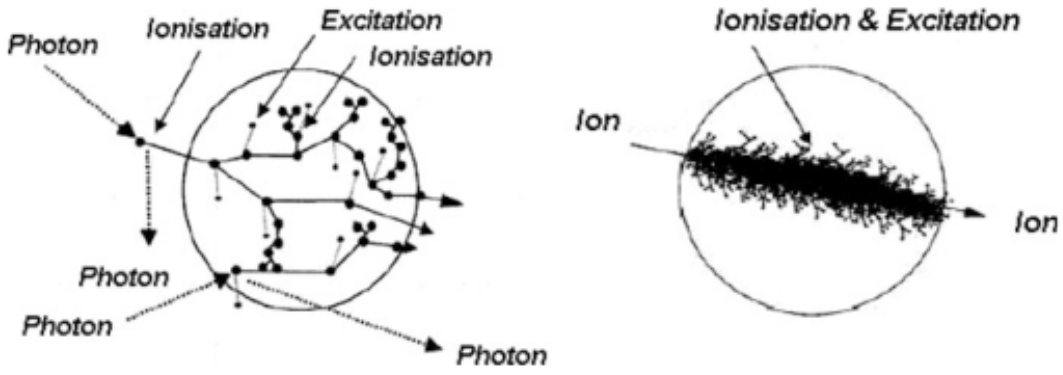

Figure 5.2: Representation of a photon track and an ion passing though matter [3]

The separate mass stopping power components can be expressed in terms of cross sections. For example, the mass electronic stopping power can be expressed as:

$$\frac{1}{\rho}(\frac{dE}{dl})_{el} = \frac{N_A}{M} Z \int w \frac{d\sigma}{dw} dw \tag{5.13}$$

where N_A is the Avogadro constant, M the molar mass of the atom, Z its atomic number, $d\sigma/dw$ the differential cross section for collisions and w is the enegy loss.

5.1.5 Linear Energy Transfer

Linear energy transfer[28],L_Δ, of a material for charged particles of certain type and energy is the quotient of dE_Δ by dl, where dE_Δ is the energy lost by a charged particle in traversing a distance dl due to electronic collisions, minus the sum of the kinetic energies of all the electrons released with kinetic energies in excess of Δ, thus:

$$L_\Delta = \frac{dE_\Delta}{dl} \tag{5.14}$$

The units is $J * m^{-1}$ or $keV * m^{-1}$. The LET can also according to the definition, be expressed as:

$$L_\Delta = S_{el} - \frac{dE_{\Delta,ke}}{dl} \tag{5.15}$$

where S_{el} is the linear electronic stopping power and $dE_{\Delta,ke}$ is the sum kinetic energies greater than Δ of all particle traversing a distance dl.

5.1.6 Absorbed Dose

The absorbed dose[28], D, is the quotient $d\bar{e}$ by dm, where $d\bar{e}$ is the mean energy imparted to matter of mass dm, thus:

$$D = \frac{d\bar{e}}{dm} \tag{5.16}$$

The unit is $J * kg^{-1}$ in SI. However the gray(Gy) unit is more widely used.

5.2 Interaction with Matter

5.2.1 Charged Particles: Electrons and Heavy Charged Particles

Two processes contribute primarily in the interaction of charged particles with matter: Coulomb interaction, which causes electron ionisation and excitation across the medium, and inelastic collisions with medium nuclei, which result in the release of photons known as "bremsstrahlung."

5.2.1.1 Coulomb Interaction

The energy transfer is adequate (>10 eV)[3] for a Coulomb interaction to drive the electron off the atom to which it is attached, create a "electron-hole pair" as a result. If it taken into account that the secondary that the electron energy is sufficient enough, further ionization across the medium is taking place. When the transfer of energy is unable to ionize, an excitation process on the orbital electrons replaces it.

5.2.1.2 Bremmstrahlung

Bremmstrahlung was caused by the deceleration of an electron near the medium's nucleus. The phenomena is significant at energy above the "critical." The empirical formula for Equation 5.17 , according to [6]:

$$T_C(MeV) = \frac{610}{Z + 1.24} \tag{5.17}$$

where Z is the atomic number of the medium.

As a result, the amount of energy transferred to the medium per length unit must be determined. The quantity of mass stopping power (subsection 5.1.4) is ideal for this task since it is independent of the medium density and related to LET:

$$\frac{S}{\rho} = \frac{1}{\rho}(\frac{dT}{dx}) \quad (MeV * cm^2 * g^{-1} \tag{5.18}$$

As stated also, in subsection 5.1.4 Equation 5.18 can be split in different components: the Coulomb interaction (col) and the bremsstrahlung one (rad). Thus Equation 5.18 can be resulted in the Equation 5.19:

$$\frac{S}{\rho} = \frac{1}{\rho}[(\frac{dT}{dx})_{coll} + \frac{dT}{dx})_{rad}] \tag{5.19}$$

Bremsstrahlung can be considered negligible for electrons due to light z material, according to [3].

$$\frac{S}{\rho} \sim (\frac{S}{\rho})_{coll}) = \frac{z^2 Z}{AT}[\ln \frac{f(T)}{I} + g(T)] \tag{5.20}$$

with T the kinetic energy of incident charged particle, z the charge carried by the incident particle, A and Z the molar mass and atomic number of crossed medium and I the mean excitation potential.

Electrons scatter when they flow through a material, largely due to elastic 'collisions' with atom nuclei, as can be observed. With lower beam energies and higher atomic numbers, scattering is more noticeable. Electrons lose energy when they pass through a material due to attenuation. Lower-energy electrons are more prone to scatter laterally. This may be seen in high-energy electron beams, where the penumbra is very narrow near the surface and widens dramatically as one goes deeper. When it comes to energy loss, the "mass scattering power," which is determined by both the incident electron energy and the material, is provided by expression.

$$\frac{\theta_s^2}{\rho} = \frac{1}{\rho}(\frac{d\theta^2}{dl}) \tag{5.21}$$

where ϑ is the mean scattering angle and ϱ is the density of material. The scattering power is proportional to the square of the atomic number Z Inversely proportional to the square of the kinetic energy of electron. Therefore, low energy electrons will be scattered more readily than high energy electrons; and high Z materials will cause more scattering than low Z material.

This clarifies two crucial physics concepts: If the in-homogeneity has a larger atomic number than the medium, electrons travelling through it can be back-scattered. On the low Z side of the in-homogeneity border, this can result in an increase in dosage. A linear accelerator produces high-energy electrons that travel in a pencil beam. They will be distributed in a variety of directions after passing through a scattering filter. To achieve the desired scattering, scattering filters are built of thin, high-Z materials.

5.2.2 Photons

Photons are a sort of "indirectly ionising" radiation that transmits its energy to secondary particles, electrons, which deposit some or all of their energy into the medium. Regarding the interaction of photons with matter, there are three main processes:

- The Photoelectric Effect
- Compton Effect

By connecting the energy to mass, we obtain an expression of the momentum dependent upon the total energy E of particle:

$$E = mc^2 \Leftrightarrow m = \frac{E}{c^2} \Leftrightarrow p = \frac{Ev}{c^2} \tag{5.22}$$

5.2.2.1 Photoelectric Effect

During the photoelectric effect, a photon interacts with a nucleus and the resulted energy, strips an orbital electron. The photo-electron is mono-energetic and its

energy can be defined by:

$$T_{ph} = E_\gamma - W_i \tag{5.23}$$

According to Rodolphe Antoni[3],"Considering that the mean ionization energy in the tissue $\bar{W}_t$ is negligible compared to the energy of incident photons, the energy transferred to the photo-electron is substantially the energy of primary photon."
The energy of the the electron from the orbital layer can thus be expressed as:

$$\bar{E_{tr}} = T_p h \cong E_\gamma \tag{5.24}$$

Note that this effect is all the more significant that the medium Z is high and the photon energy is low.

$$\sigma_{ph} \propto Z^5 E^{-7/2} \tag{5.25}$$

5.2.2.2 Compton Effect

The Compton Effect can be described as an inelastic scattering with decrease of photon energy on the orbital electron, which is expunged with a some of the energy of the primary photon.

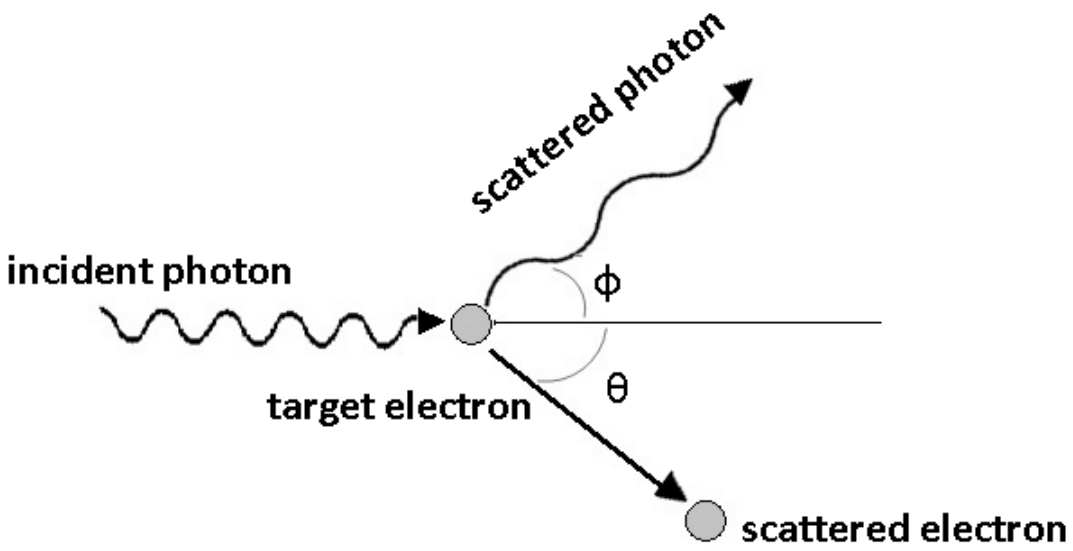

Figure 5.3: Compton Scattering [31]

The energy of the photon after the interaction is given, in the following

$$E'_\gamma = \frac{E_\gamma}{1 + \frac{E_\gamma}{m_0 c^2}(1 - cos\theta} \tag{5.26}$$

The energy transferred to the Compton electron is obtained by subtracting this energy to the photon of primary energy.

$$T_c = E_\gamma - E'_\gamma \Leftrightarrow T_c = \frac{E_\gamma^2(1 - cos\theta)}{m_o c^2 + E_\gamma(1 - cos\theta)} \tag{5.27}$$

From Equation 5.27, we can draw results for the maximum and minimum value.

$$T_c(max) \simeq \frac{4E_\gamma^2}{4E_\gamma + 1} \quad E_\gamma(MeV) \tag{5.28}$$

The differential cross section is expressed through the relationship of Klein and Nishina [12].

$$(\frac{d\sigma_c}{d\Omega})_{E_\lambda} = \frac{r_o^2}{2}(\frac{E'_\gamma}{E_\gamma})^2((\frac{E_\gamma}{E'_\gamma}) + (\frac{E'_\gamma}{E_\gamma}) - sin^2\theta) \Longleftarrow (\frac{d\sigma_c}{d\Omega})_{E_\lambda} = f(E_\gamma, \theta) \tag{5.29}$$

Where r_o is the classical radius of the electron with a value of 2.818fm.
Furthermore, $\sigma_{c,total}$ is determined by integrating over all space and by weighting by the Z of the medium in order to take into account all orbital electrons [3]:

$$\sigma_{c,total} = Z \int_\Omega (\frac{d\sigma_c}{d\Omega})_{E_\gamma} d\Omega \tag{5.30}$$

5.2.3 Neutrons

Elastic and inelastic collisions occur when these uncharged and neutral particles hit with the nuclei of the crossing medium. The elastic collision (n,n) is a simple mechanical analogue. This collision mechanism has no effect on the target nucleus' internal structure. However, in an inelastic collision, this internal change occurs.

- Inelastic scattering (n,n')
- Capture (n,X)

5.2.3.1 Eleastic Scattering

The original kinetic energy of the neutron is shared with the nucleus, which simply experiences recoil and is not left in an excited state. The smaller the nucleus' mass, the greater the fraction of kinetic energy it absorbs. The average fraction of neutron energy transmitted to an atomic medium each collision. From the conservation of energy, $E_n(i) = E_n(f) + E_{tr}$, the incident neutron energy to that transferred to the recoil nucleus, in the following

$$E_{tr} = E_n(i)\frac{4A}{(A+1)^2}cos^2\phi \tag{5.31}$$

Finally, notice that the general law to estimate the mean energy of neutron having passed through depth x:

$$\bar{E_n}(x) = E_n(i)exp[-\frac{\sum_s (1-a)x}{2}] \quad with \quad a = (\frac{A-1}{A+1})^2 \tag{5.32}$$

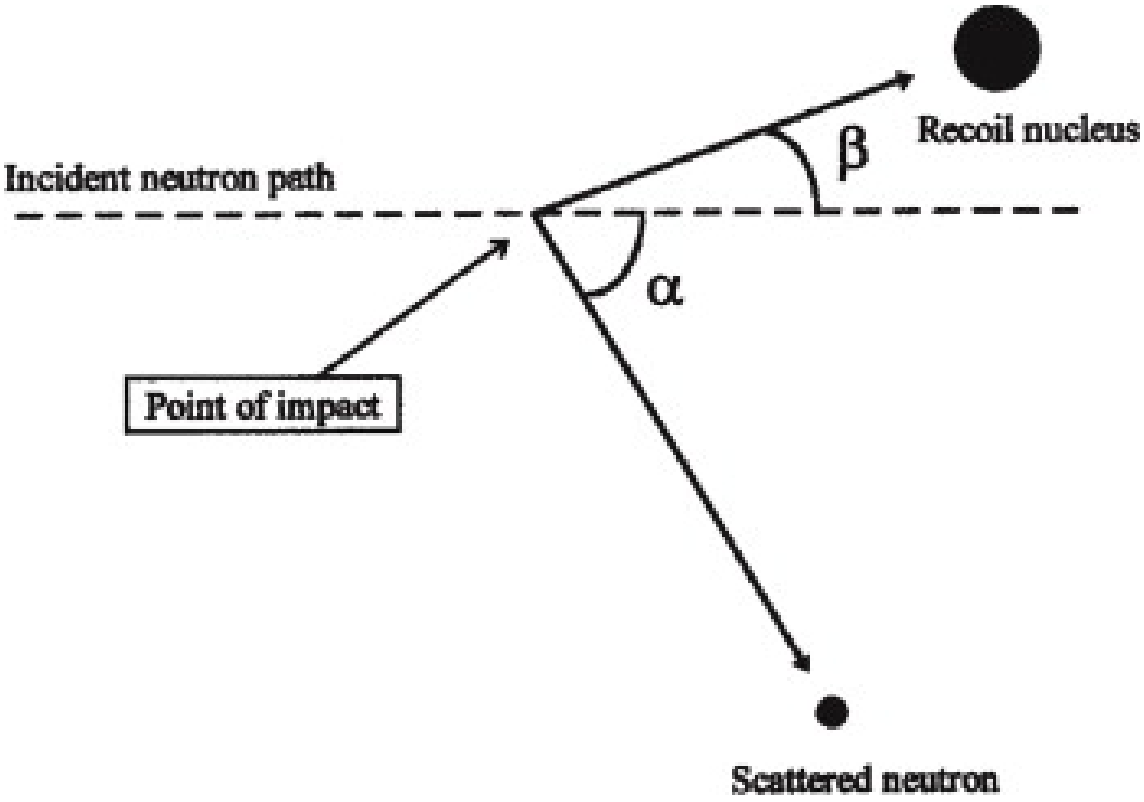

Figure 5.4: Principle of elastic scattering for neutrons

5.2.3.2 Inelastic Scattering

This nuclear reaction is going through a transitional stage where the neutron enters the target nucleus and creates a "compound nucleus" [3] that is tremendously excited and consequently unstable. The output method will consist of producing a new neutron n' with a lower energy than the incident neutron. After the emergence of the neutron, the leftover nucleus, which is identical to the initial nucleus, remains excited and produces a photon:

$$\mathrm{n} + {}^{\mathrm{A}}_{\mathrm{Z}}\mathrm{X} \rightarrow {}^{\mathrm{A+1}}_{\mathrm{Z}}\mathrm{X}^{*}_{\mathrm{NC}} \rightarrow \mathrm{n}'{+}\ {}^{\mathrm{A}}_{\mathrm{Z}}\mathrm{X} \rightarrow {}^{\mathrm{A}}_{\mathrm{Z}}\mathrm{X} + \gamma$$

The difference between the energy of the input neutron and the energy of the de-excited photon roughly equals the mean energy transmitted to the recoil nucleus[13]:

$$\bar{E_{tr}} \cong E_n(i) - E_\gamma = E_n(i) - E^*_{NC} \tag{5.33}$$

5.2.3.3 Radiative Capture (n,X)

The target nucleus captures the incident neutron, resulting in a compound nucleus that can be energized and release gamma radiation. Because thermal neutrons may cause this reaction in nearly all nuclides, it is most likely the most prevalent. In the radiative capture, the incident neutron remains "trapped" and the release of energy happens with a photon[29]:

$$\mathrm{n} + {}^{\mathrm{A}}_{\mathrm{Z}}\mathrm{X} \rightarrow {}^{\mathrm{A+1}}_{\mathrm{Z}}\mathrm{X}^{*}_{\mathrm{NC}} \rightarrow {}^{\mathrm{A+1}}_{\mathrm{Z}}\mathrm{X} + \gamma$$

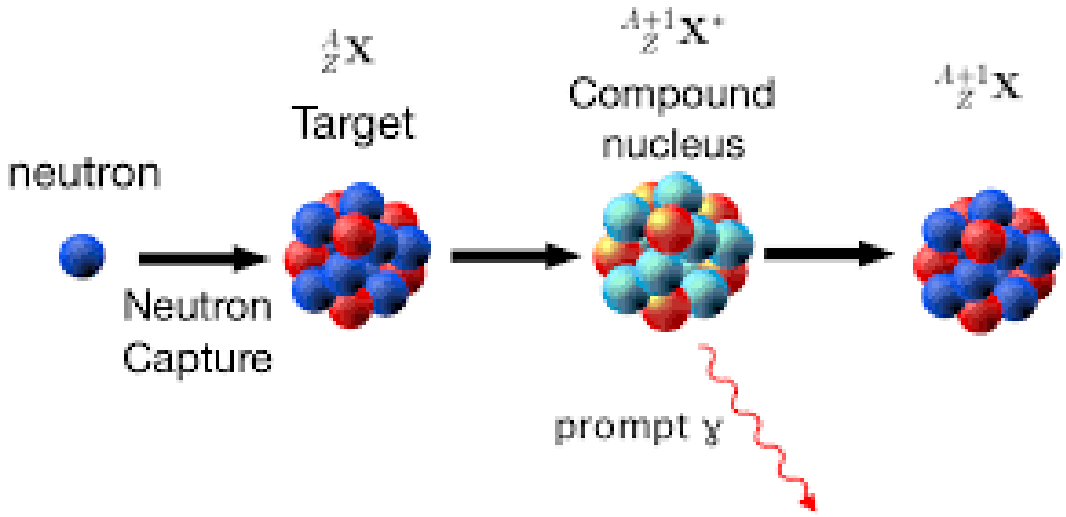

Figure 5.5: Radiative neutron capture process (n,X). From **PRETAM KUMAR DAS**

The energy of the recoil nucleus can be calculated by the conservation of momentum:

$$\sum \bar{p} = 0 \Longrightarrow \bar{p_\gamma} + \bar{p_r} = 0 \iff (\frac{E_\gamma}{c}) - M'v = 0 \iff E_{tr} = \frac{E_\gamma^2}{2M'c^2} \tag{5.34}$$

6. Simulation Tools

6.1 OMERE

https://www.trad.fr/en/space/omere-software/ is a software dedicated to space environment and radiation effects on electronic devices. This tool is developed by TRAD with the support of the National Centre for Space Studies (CNES), based on the requirements set by the European Space Agency through its European Cooperation for Space Standardization (ECSS).

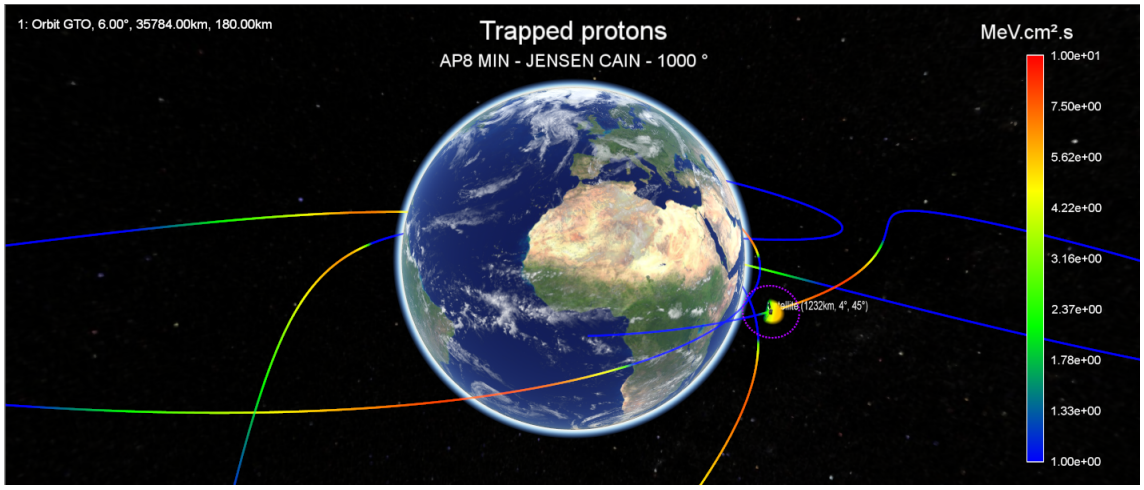

Figure 6.1: Caption

The software has the following, possibilities:

- Orbit definition
- Particle fluxes calculation
- Dose-depth curve calculation
- Non-Ionising dose and equivalent fluence depth curve
- LET and transported behind shielding proton fluxes
- SEE rate estimation for components for a space mission
- Solar Cell Degradation

6.2 FASTRAD

https://www.fastrad.net/ is the second simulation tool used in this thesis. FASTRAD is developed by the firm TRAD (TRAD, 2017) from 1999 onwards and has received support by the European Space Agency (ESA). Thanks to the Computer-aided design Interface, the program can incorporate full 3D models and immerse them into the selected radiation environment. The radiation simulation software estimates the dose and displacement damage of electronics and material of spacecraft, such that the weak spots of a design can be assessed. By selecting sections or even subsystems of a spacecraft, the aluminium mass equivalence can be determined that is required for the shielding of the section or subsystem.

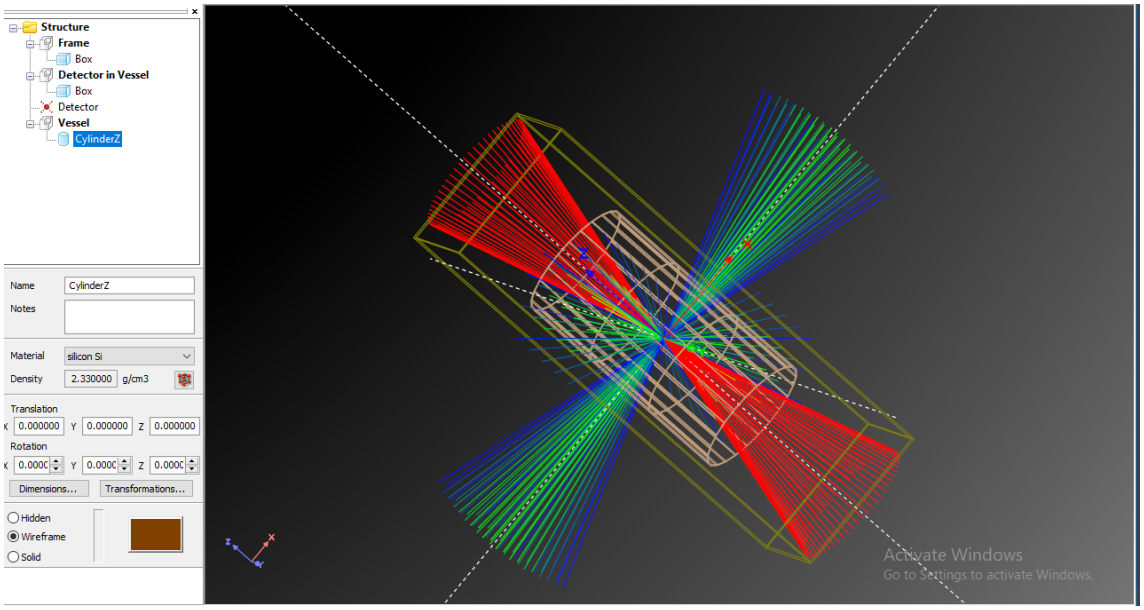

Figure 6.2: A look into the 3D environment of the FASTRAD.

This software provides advanced radiation dose analysis and shielding optimization with ray-tracing and Monte Carlo calculation methods to predict space radiation effects at electronic component and material levels .

7. OMERE - Simulation Results

7.1 Simulation Details and Mission Definition

The parameters listed in this paragraph are similar for each of the 8 simulations. The number of the simulations can be found by multiplying the different orbital cases and the two cases for the mission lifetime. As stated in the previous version, the mission duration was one year, but with the new additions there is the possibility of a one and a half mission. Therefore, in order to be compliant with the requirements that have been set by the team, both durations are calculated. The start date and time of each mission is set at 12:00.000 UTC in 01/07/2023. Lastly, all simulations will run for 300 orbits with 100 points for each orbit in order to have better Earth coverage.

7.1.1 Assumptions in Orbit Definition

The Keplerian parameters that affect the radiation analysis are only the semi-major axis (a) and the inclination (i). Therefore, due to the fact that the initial position of the satellite doesn't affect the radiation analysis, the three Keplerian parameters (Argument of Periapsis (AP), Longitude of the Ascending Node and True Anomaly (TA)) that define the initial position are set to zero. The last assumption made regarding the orbit definition is its circular nature. In order to have similar conditions during the run of the experiments, the value of the eccentricity should be close to zero.

Table 7.1: AcubeSAT Orbital Parameters for the Baseline Orbit

Keplerian Elements	Value
Semi-major axis (a)	6878 km
Inclination (i)	97.189
Eccentricity (e)	0
RAAN (Ω)	0
Argument of Perigee (ω)	0
True Anomaly (v)	0

Table 7.2: AcubeSAT Orbital Parameters for the Upper Orbit

Keplerian Elements	Value
Semi-major axis (a)	6978 km
Inclination (i)	97.764
Eccentricity (e)	0
RAAN (Ω)	0
Argument of Perigee (ω)	0
True Anomaly (v)	0

7.2 Detector layout and shielding

For the calculation of the TID, the geometry and the thickness of the shielding must be defined. The material of the shielding in *OMERE* is aluminum by default, which is deemed suitable, since the frame and the payload container are made from this material. From the available geometry options of the software, the sphere suits best the design of AcubeSAT. Three targets were selected to calculate the dose, the first being the area for the electronics of the AcubeSAT, the COMMS, the ADCS/OBC and the EPS board. Due to lack of available space, these three Printed Circuit Board (PCB)s only have the frame and solar panels functioning as shielding, which is 1.7 mm thick. On the other hand, the two remaining targets are situated inside the payload container, which adds an extra 3 mm of shielding with a total shielding of 4.7 mm. The materials of the target are silicon for the electronics part and human tissue for the biological part.

7.3 Results - SSO 600km

As part of recent changes in the mass budget, the SSO orbit higher than 550km, which is the current upper limit is investigated. Therefore, a higher altitude around 600km has been added in the list for scenarios. It is obvious that this orbit shall be the harshest and it is a test to see whether we comply with our radiation requirements.

7.3.1 Flux Calculation

7.3.1.1 Trapped Protons and Electrons

In the subsection of the appendix, the fluxes of trapped particles are presented as well as the fluxes of particles in Figure 7.1.

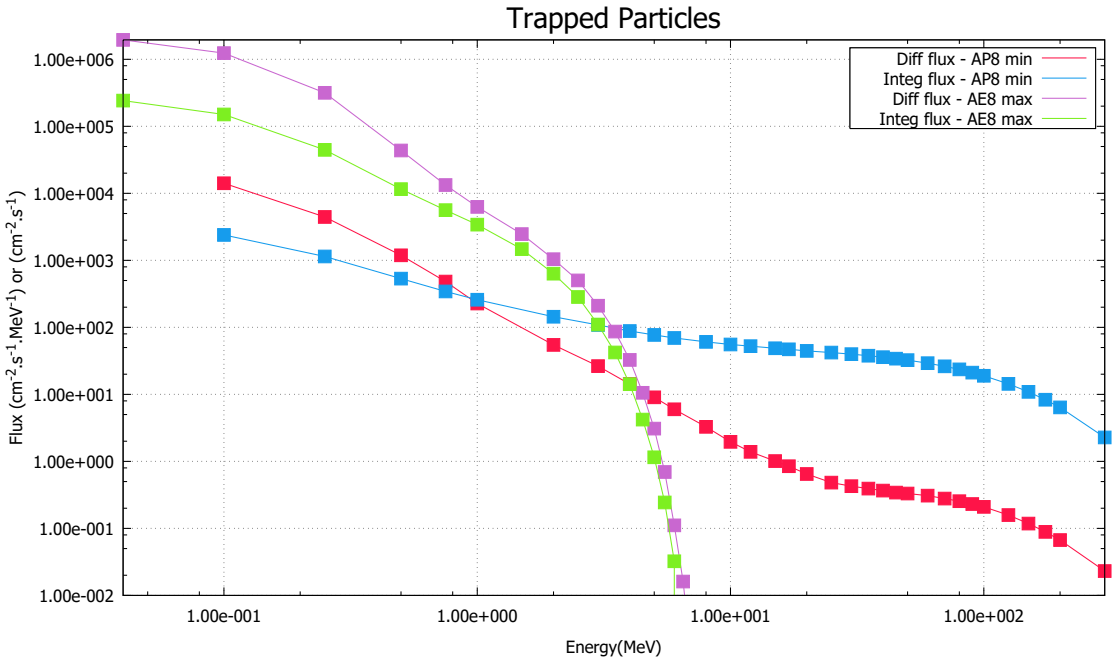

Figure 7.1: Flux Graph for Trapped Particles

7.3.1.2 Solar Energetic Protons and Ions

In this subsection, the mean fluxes and the flux along the orbit of particles from the Sun are presented in Figure 7.2.

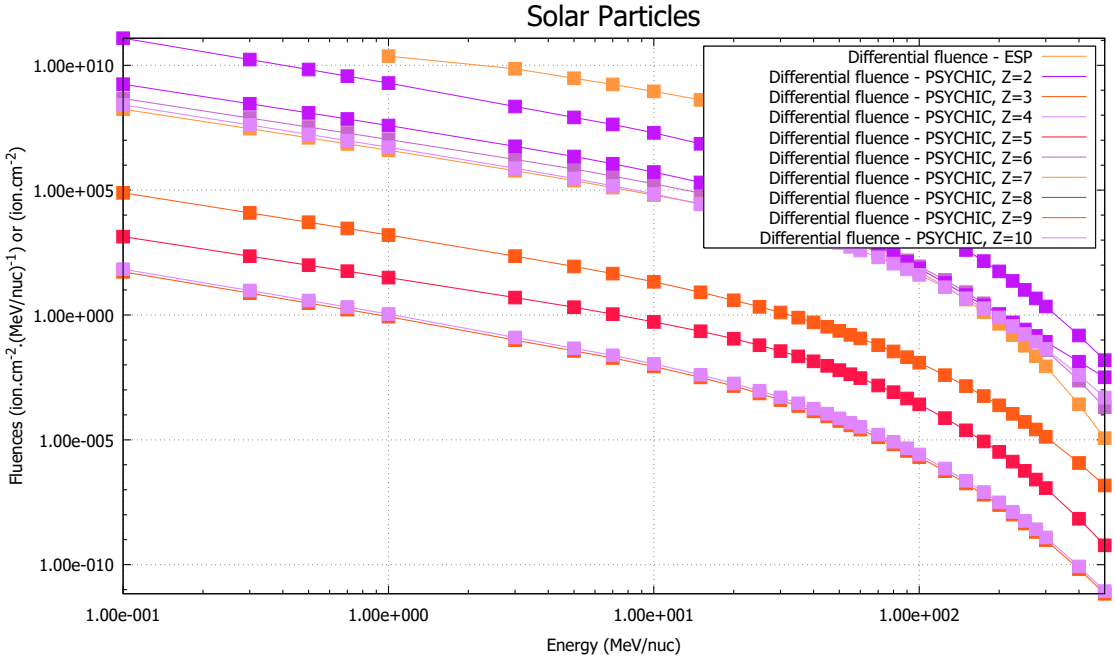

Figure 7.2: Flux Graph for Energetic Solar Particles

7.3.1.3 Solar Flares

In this subsection, the fluxes of particles from solar flares are presented in Figure 7.3.

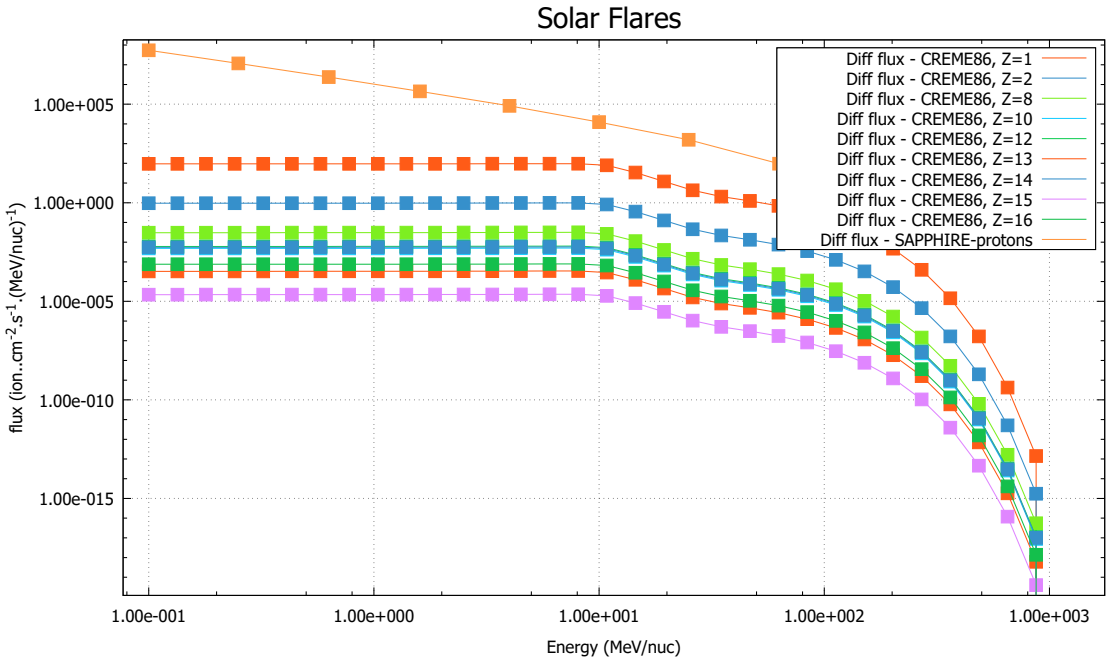

Figure 7.3: Flux Graph for Solar Flares

7.3.1.4 Galactic Cosmic Rays

In this subsection, the fluxes of ions from the galactic cosmic rays are presented in Figure 7.4.

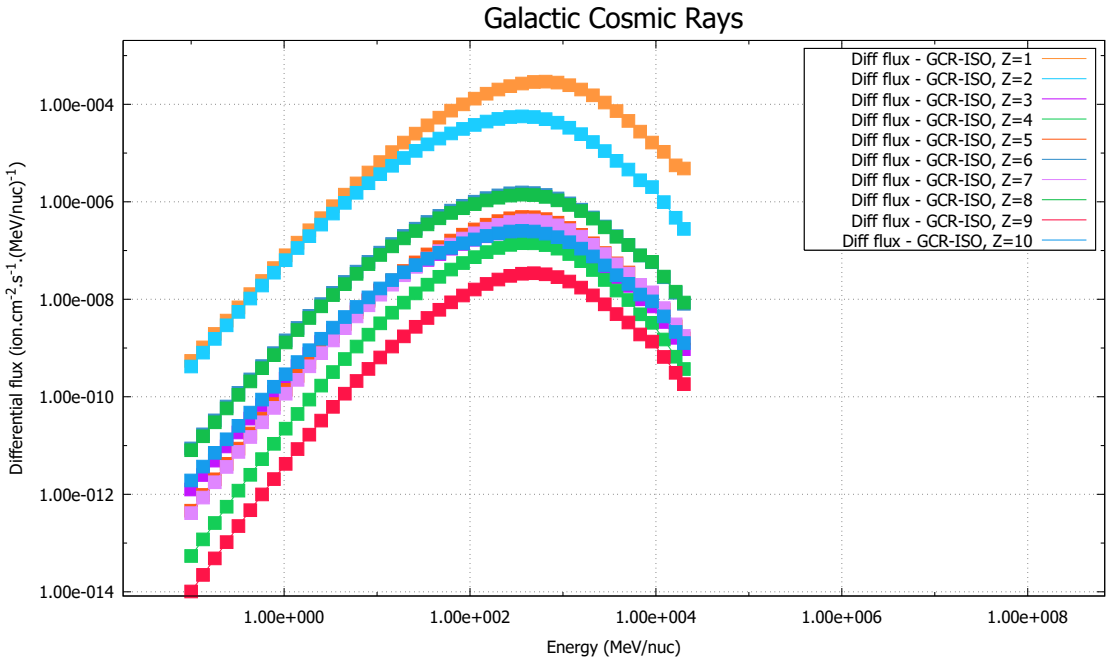

Figure 7.4: Flux Graph for Galactic Cosmic Rays

7.3.2 Linear Energy Transfer(LET) Calculation

7.3.2.1 Mission Duration: 1 year

In this subsection, the results for the Linear Energy Transfer (LET) values are presented for a possible off 600km. The values are four in total, as stated in the Linear Energy Transfer calculation section and are presented below with the representative graph showing the difference between the effect of solar Flares regarding the Linear Energy Transfer calculation (Figure 7.5).

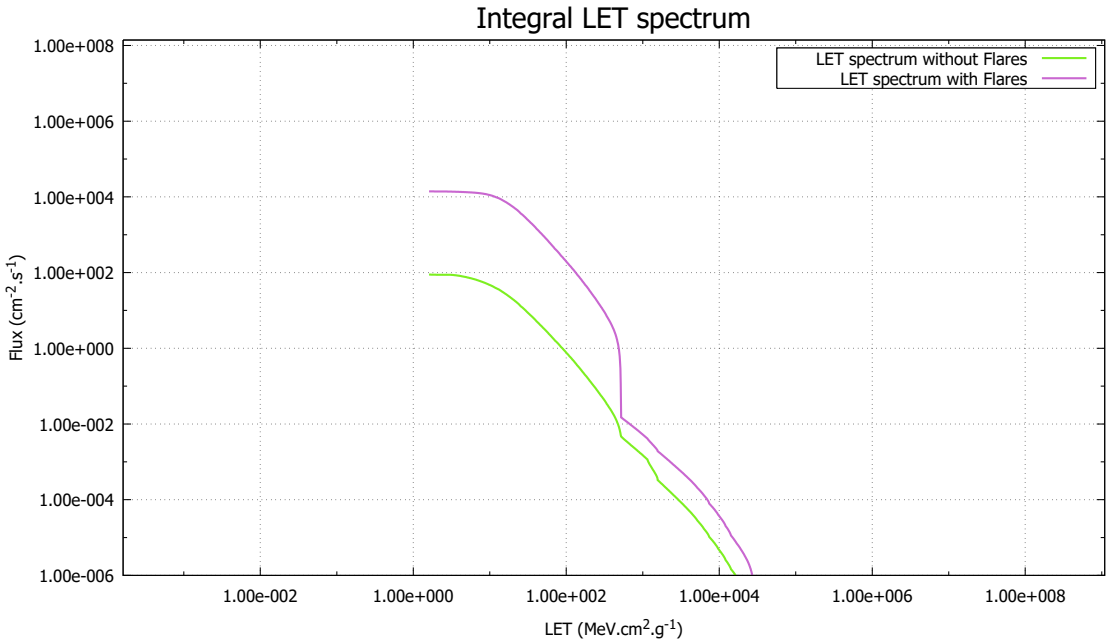

Figure 7.5: Both LET curves at 4.7mm

7.3.2.2 Mission Duration: 1.5 year

In this subsection, the results for the Linear Energy Transfer values are presented for a possible off 600km. The values are four in total, as stated in the Linear Energy Transfer calculation section and are presented below with the representative graph showing the difference between the effect of solar Flares regarding the Linear Energy Transfer calculation (Figure 7.6).

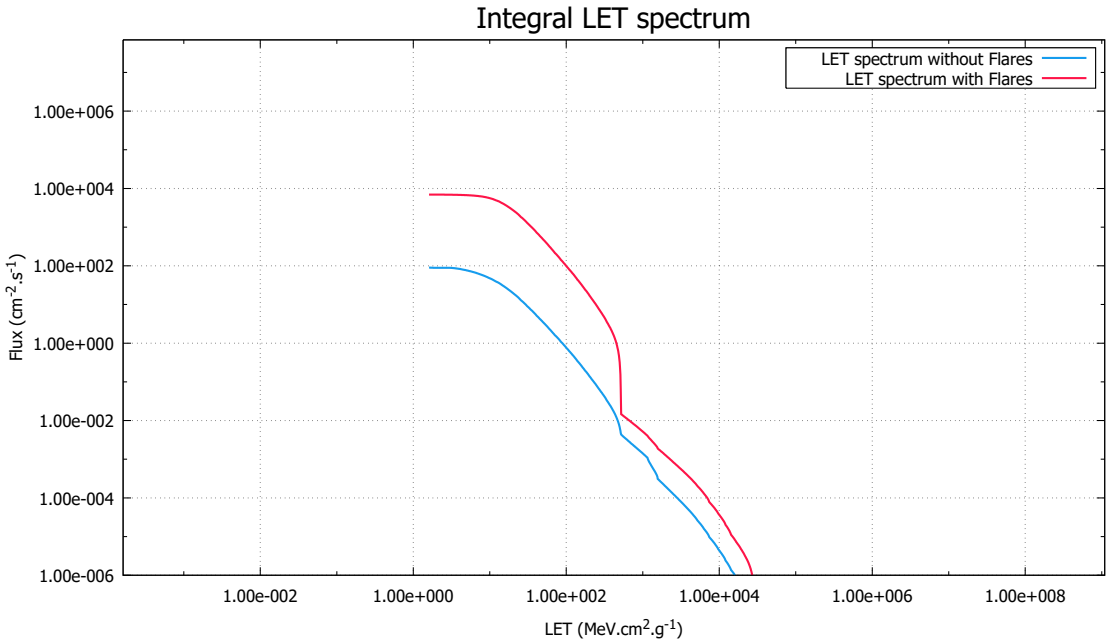

Figure 7.6: Both LET curves at 4.7mm

7.3.3 Dose Calculation

In this section, the dose depth is calculated regarding the fluxes, as given by the radiation analysis. For each orbit, two different dose depths are calculated, as also stated before, for two different targets. Regarding radiation, the physical phenomena of interaction considered are nuclear attenuation, local charged-secondary energy deposition and exponential distribution approximation of neutron dose.

7.3.3.1 Mission Duration: 1 year

The dose depth graphs for both targets are presented below for both silicon and muscle target in Figure 7.7 and Figure 7.8 respectively.

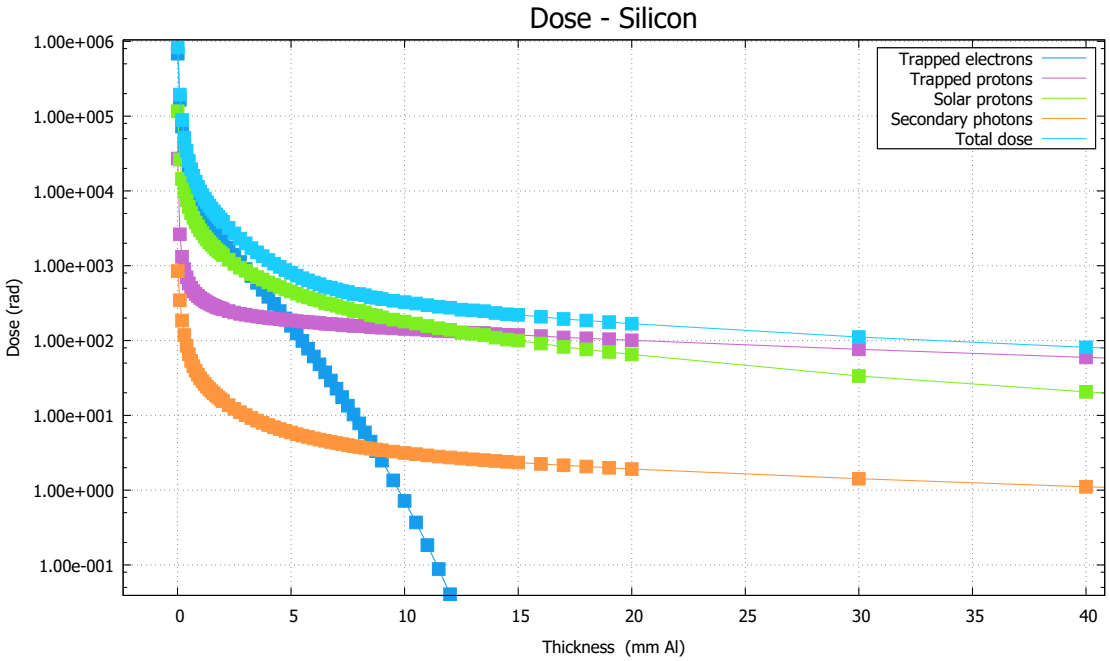

Figure 7.7: Dose depth curve for silicon target

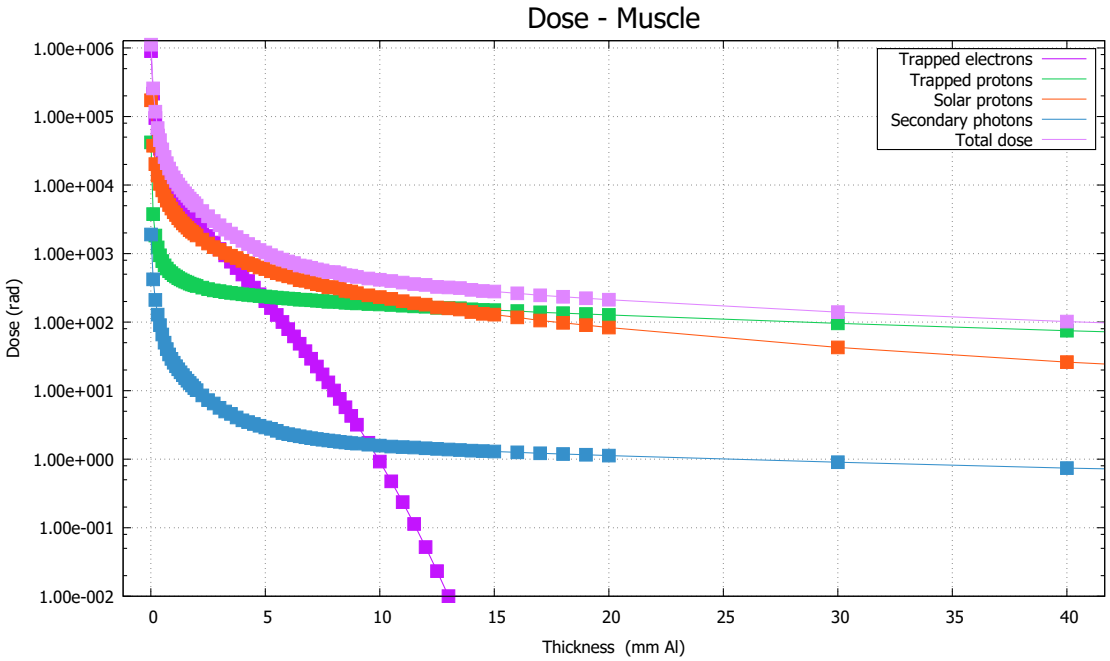

Figure 7.8: Dose depth curve for muscle tissue target

7.3.3.2 Mission Duration: 1.5 years

The dose depth graphs for both targets are presented below for both silicon and muscle target in Figure 7.9 and Figure 7.10 respectively.

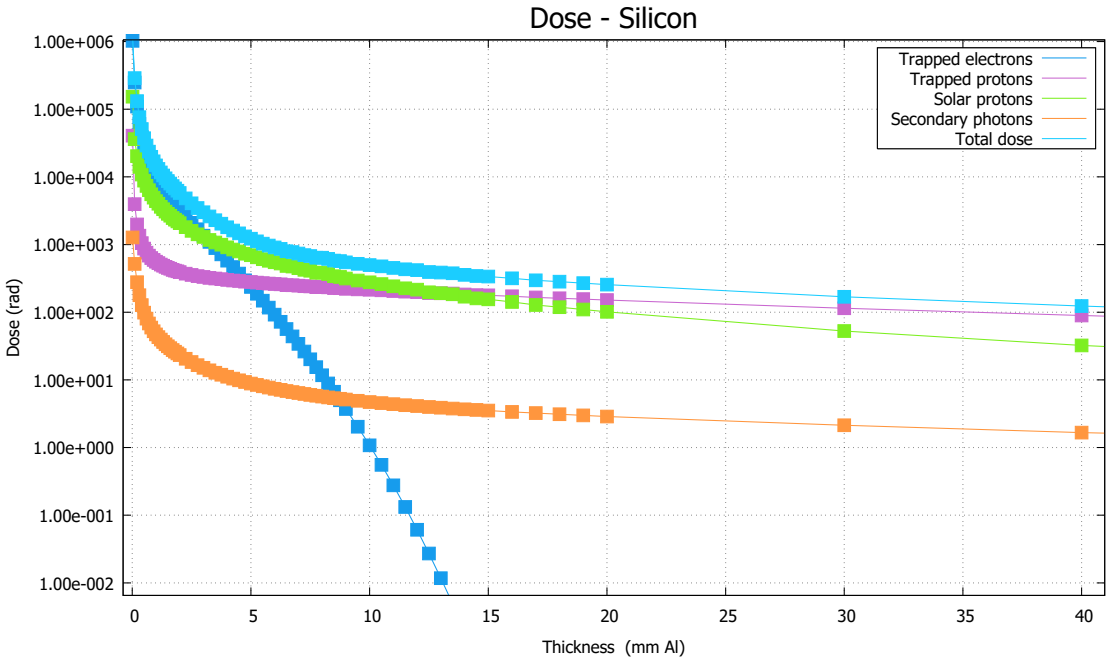

Figure 7.9: Dose depth curve for silicon target

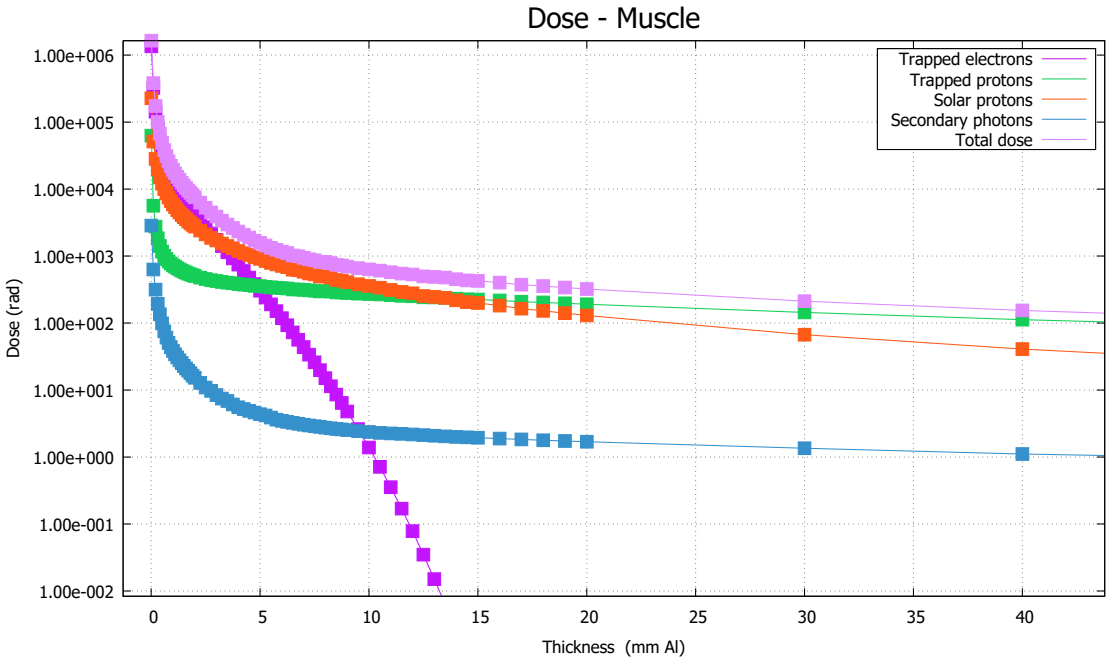

Figure 7.10: Dose depth curve for muscle tissue target

Table 7.3: Dose-depth values for SSO 600km

Orbits	Deposited dose - Silicon (krad)	Deposited dose - Muscle (krad)
SSO 600	4.873	6.349
	0.878	1.125

7.4 Results - SSO 500km

7.4.1 Flux Calculation

For each candidate orbit, the fluxes of each radiation source listed above are calculated and presented.

The Sun-Synchronous Orbit is considered to be the baseline orbit. A representative orbit inside the altitude ranges from the possible orbits.

7.4.1.1 Trapped Protons and Electrons

In the subsection of the appendix, the fluxes of trapped particles are presented in Figure 7.11.

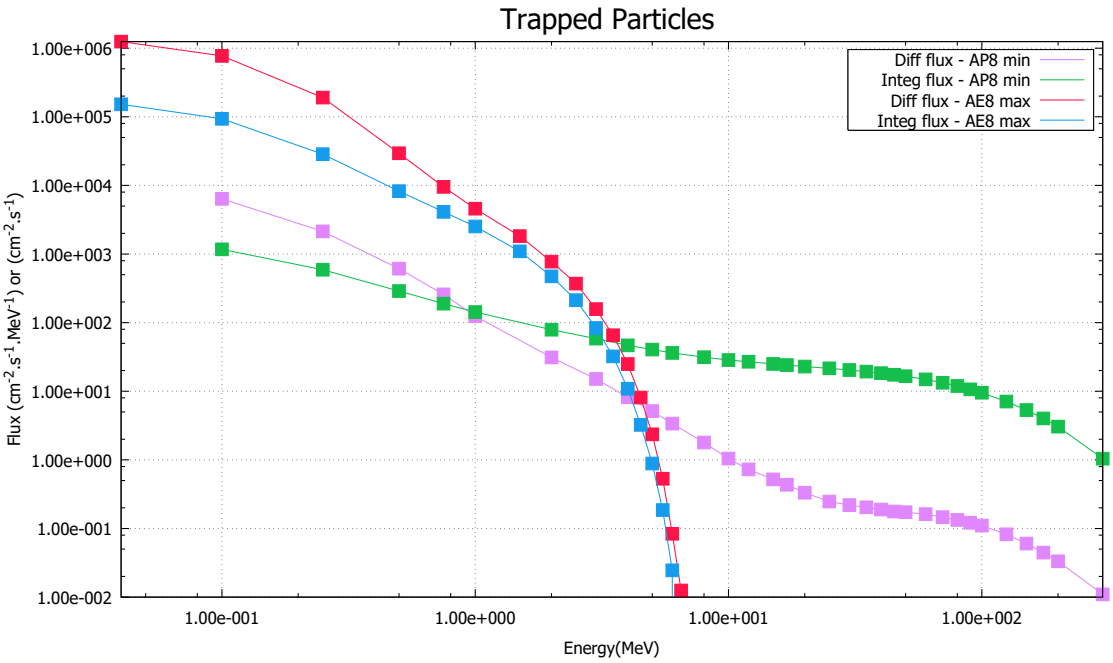

Figure 7.11: Flux Graph for Trapped Particles

7.4.1.2 Solar Energetic Protons and Ions

In this subsection, the mean fluxes and the flux along the orbit of particles from the Sun are presented in Figure 7.12.

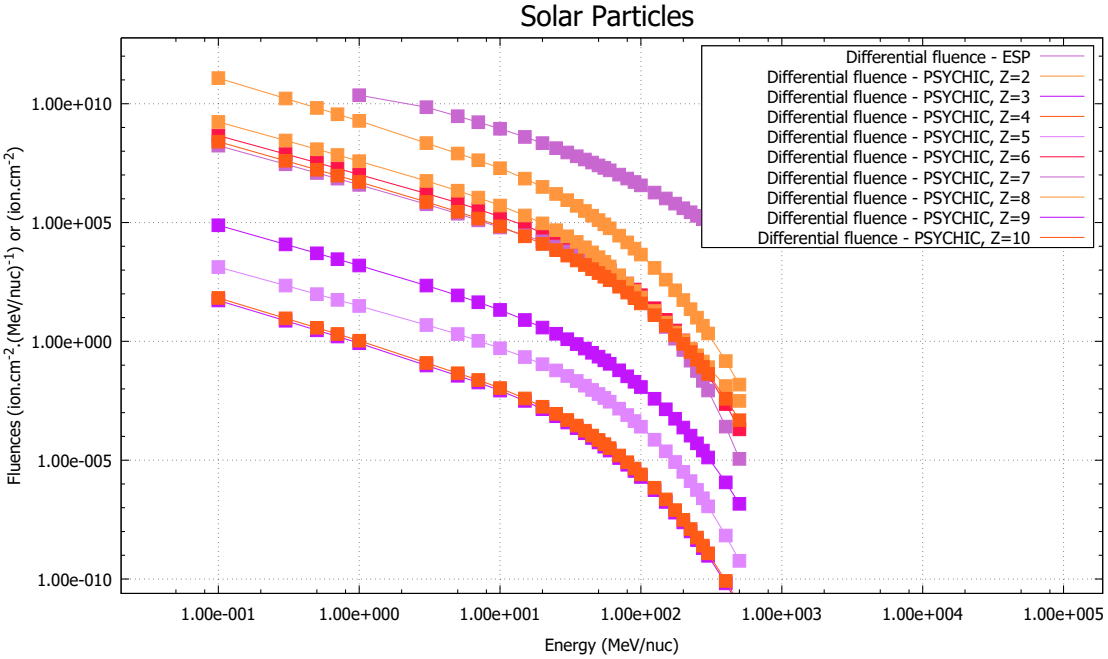

Figure 7.12: Flux Graph for Energetic Solar Particles

7.4.1.3 Solar Flares

In this subsection, the fluxes of particles from solar flares are presented in Figure 7.13.

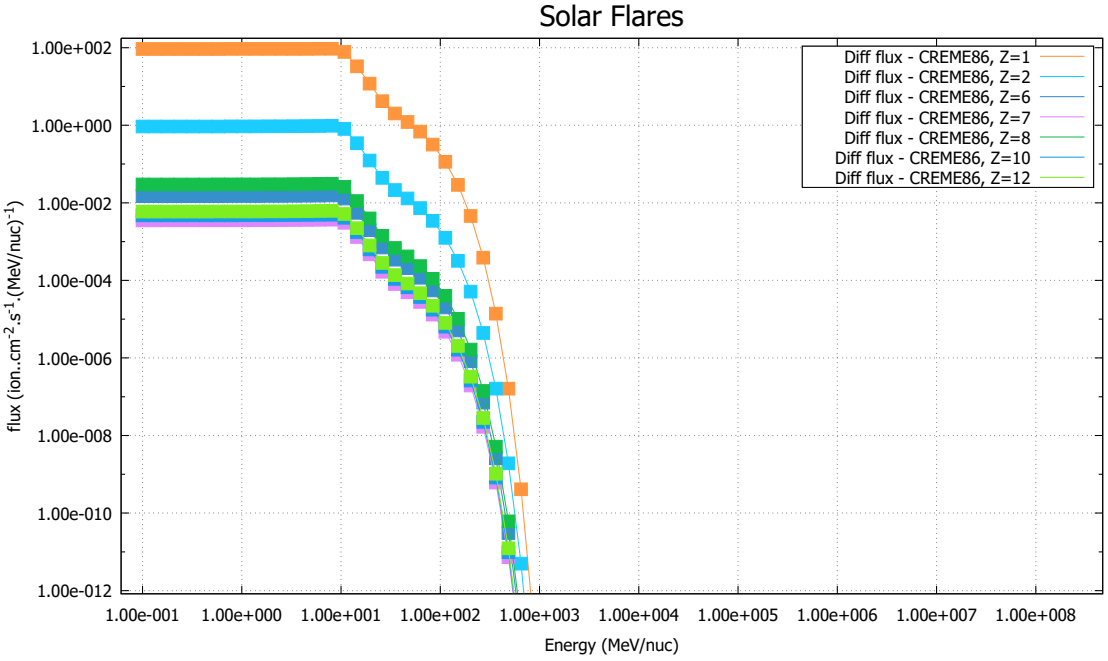

Figure 7.13: Flux Graph for Solar Flares

7.4.1.4 Galactic Cosmic Rays

In this subsection, the fluxes of ions from the galactic cosmic rays are presented in Figure 7.14.

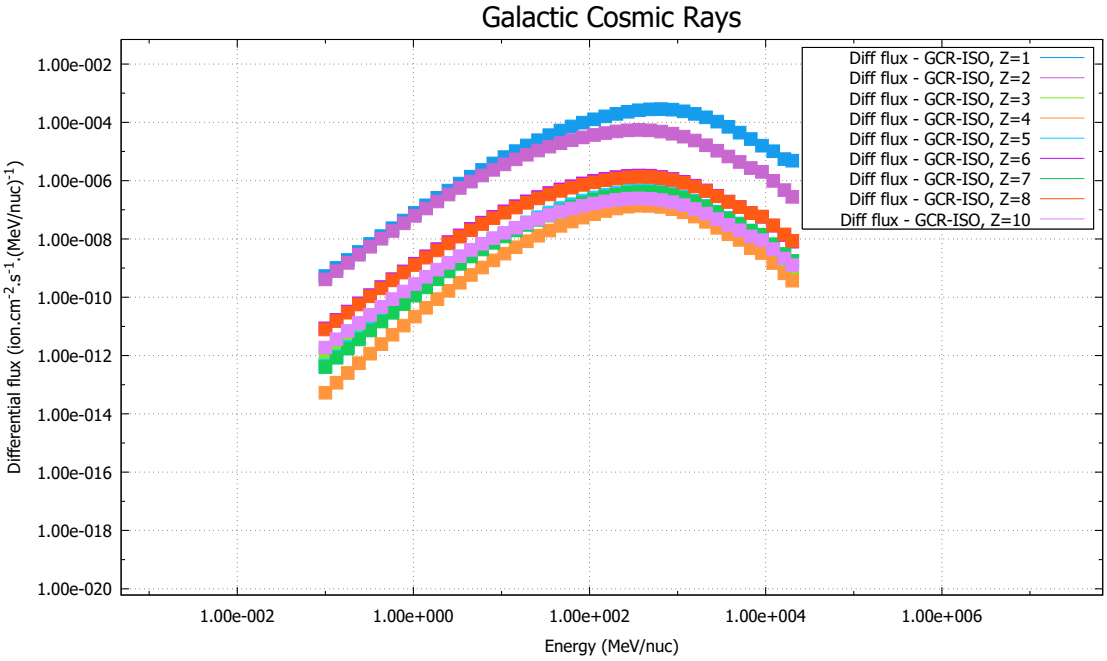

Figure 7.14: Flux Graph for Galactic Cosmic Rays

7.4.2 Linear Energy Transfer(LET) calculation

In this section, the Linear Energy Transfer is presented. The sources of Linear Energy Transfer are trapped and solar energetic protons, as well as ions from the cosmic rays. The defined targets of the Linear Energy Transfer are two: one with a shielding of 1.7 mm aluminium, which simulates the inside of the of the AcubeSAT and one with shielding of 4.7 mm, which simulates the area inside the payload container. Furthermore, two different types of Linear Energy Transfer are simulated, with and without the solar flares models. Finally the graphs and the results for both mission durations have been calculated.

7.4.2.1 Mission Duration: 1 year

In this subsection, the results for the Linear Energy Transfer values are presented for the baseline Sun-Synchronous Orbit. The values are four in total, as stated above, and are presented below with a representative graph of the difference between the effect of Solar Flares in the Linear Energy Transfer calculation (Figure 7.15).

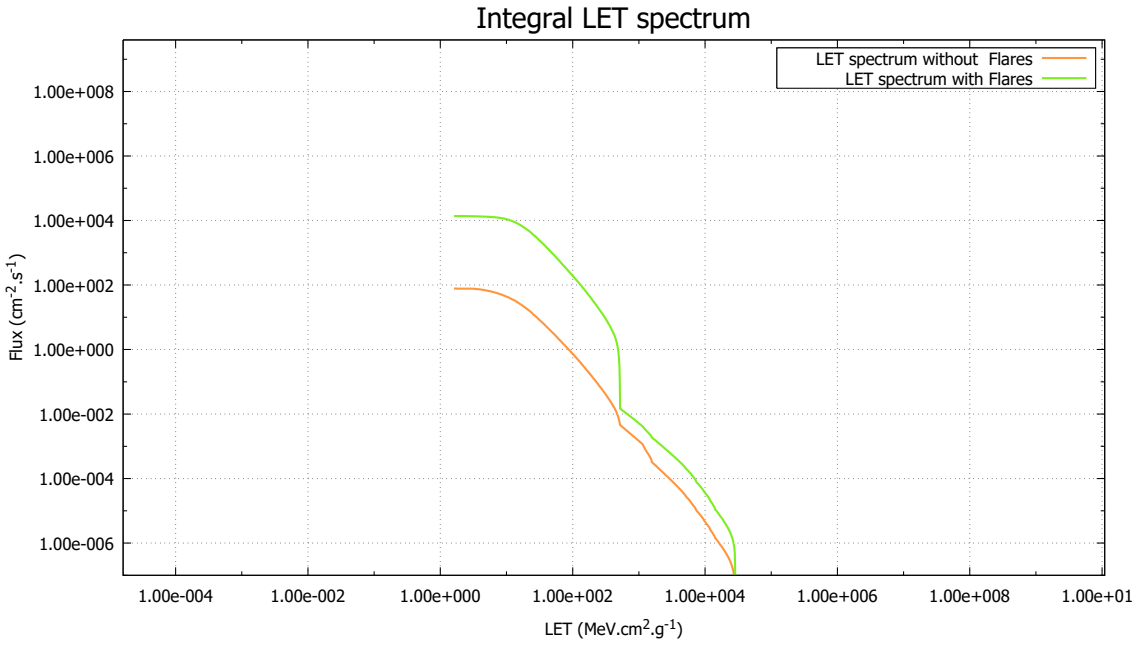

Figure 7.15: Both Linear Energy Transfer curves at 4.7mm

7.4.2.2 Mission Duration: 1.5 years

In this subsection, the results for the Linear Energy Transfer values are presented for the baseline Sun-Synchronous Orbit. The values are four in total, as stated above in the Linear Energy Transfer calculation section, and are presented below with a representative graph of the difference between the effect of Solar Flares in the Linear Energy Transfer calculation,Figure 7.16.

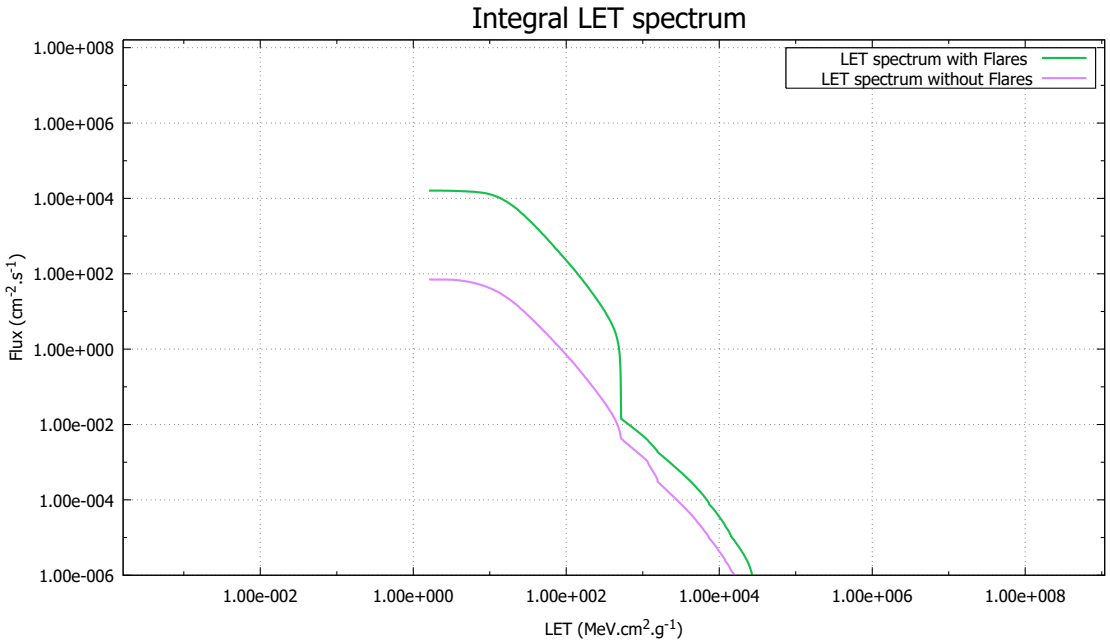

Figure 7.16: Both Linear Energy Transfer curves at 4.7mm

7.4.3 Dose Depth Calculation

In this section, the dose depth is calculated regarding the fluxes, as given by the radiation analysis. For each orbit, two different dose depths are calculated, as also stated before, for two different targets. Regarding radiation, the physical phenomena of interaction considered are nuclear attenuation, local charged-secondary energy deposition and exponential distribution approximation of neutron dose.

7.4.3.1 Mission Duration: 1 year

The dose depth graphs for both target are in Figure 7.17,Figure 7.18.

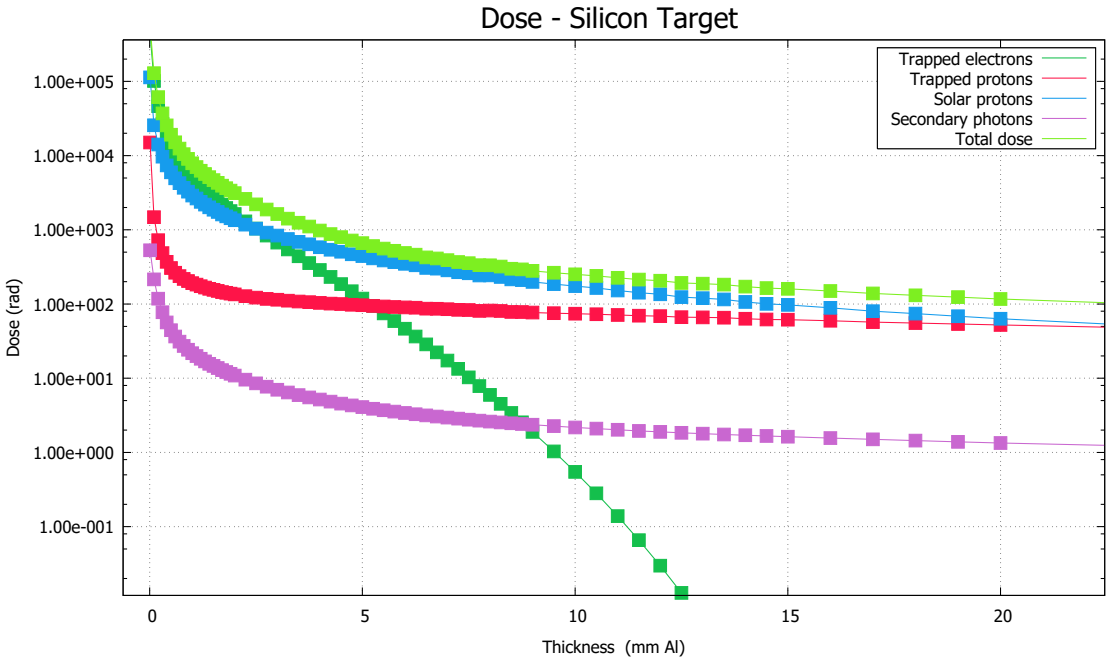

Figure 7.17: Dose depth curve for silicon target

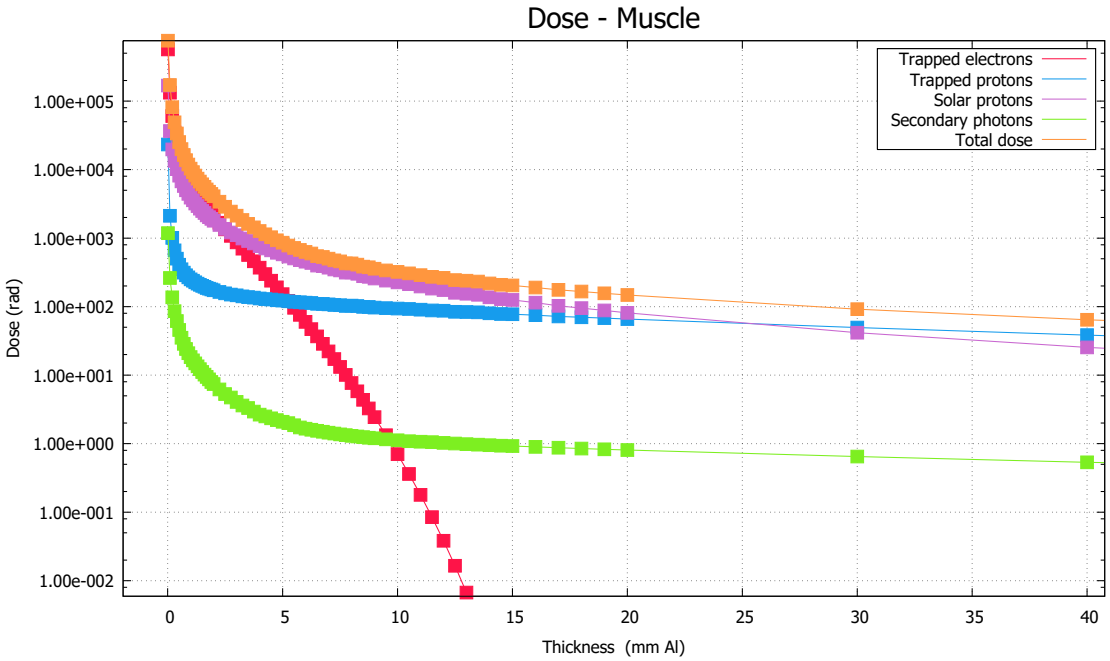

Figure 7.18: Dose depth curve for muscle tissue target

7.4.3.2 Mission Duration: 1.5 year

The dose depth graphs for both targets are in Figure 7.19,Figure 7.10.

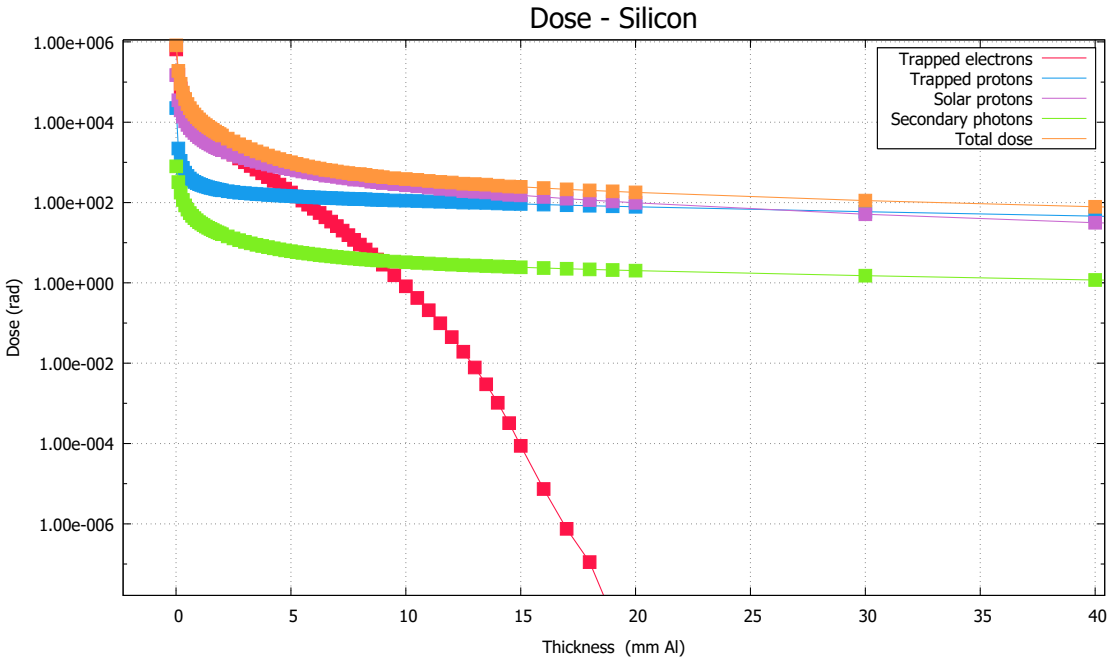

Figure 7.19: Dose depth curve for silicon target

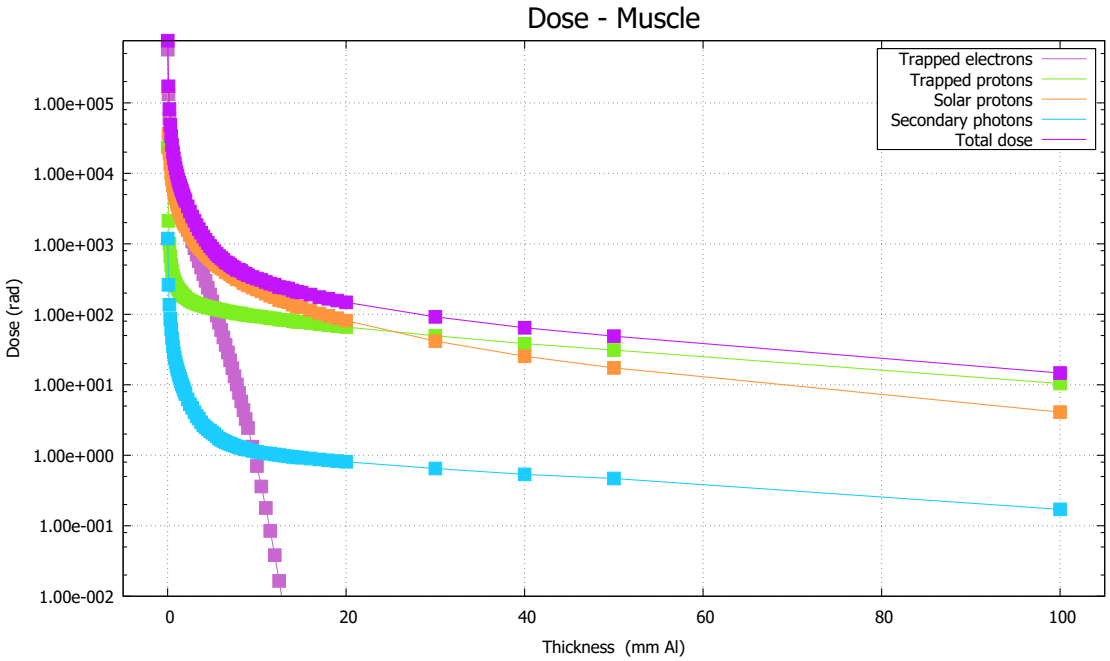

Figure 7.20: Dose depth curve for muscle tissue target

Table 7.4: Dose-depth values for SSO 500km

Orbits	Deposited dose - Silicon (krad)	Deposited dose - Muscle (krad)
SSO 500	3.955	5.139
	0.719	0.929

8. FASTRAD - Simualation Results

For the analysis in the FASTRAD software, only one orbit will be studied since the worst case scenario analysis is needed. From the chapter 7, it is obvious that the height of the orbit is proportional to the dosage level in the satellite. Therefore, only the orbit "SSO 600" is presented here.

8.1 Simulation Techniques Models

The methods utilized in these thesis, the Forward Monte Carlo (FMC) and Ray-Tracing Method (RTC) will be studied.

8.1.1 FMC Method

Forward Monte Carlo (FMC) is unique tool that enables the calculation of the deposited dose of electrons, photons and protons. There are two general principles: (1) each particle is tracked from the source until the target and (2) physical interactions and material properties are considered: better calculation accuracy than the Ray-Tracing method[18]. However, a considerable calculation time is used when the sensitive area is small compared to the full model. Therefore lots of particles are wasted.

In a MC method, there is a realistic particle tracking from the source in the geometry. When tracking the particles in a geometry from the source, the simulation stops when (1) the particles leave the geometry or (2) the particles lose their energy. The particle trajectories and behavior depend on the physical process selected at each step, with the example in the following Figure 8.1:

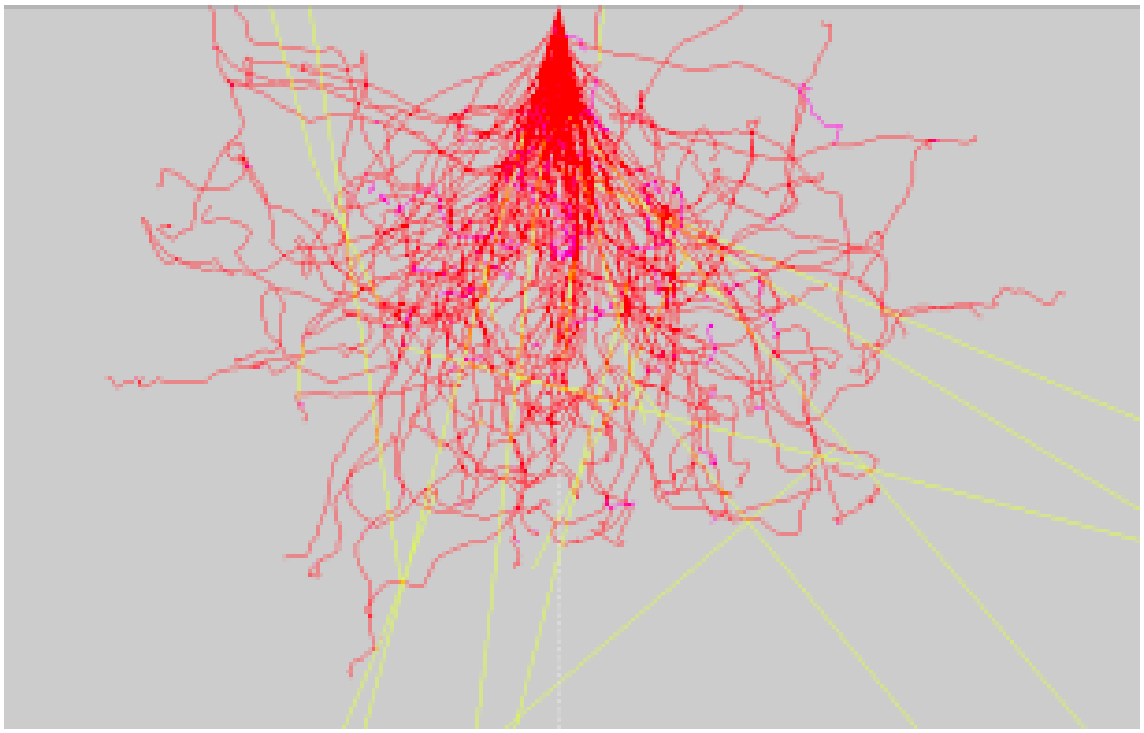

Figure 8.1: Passage of particles through matter.

The particles are tracked step by steps. Steps are limited by geometrical boundaries or physical processes. Several physical lengths (i.e. mean free paths) are calculated from cross sections depending on particle type, energy and material. Also, the shortest length (among the physical and geometrical lengths) is selected for each step corresponding to the process that has the highest probability of occurring. Then the physical process is applied.

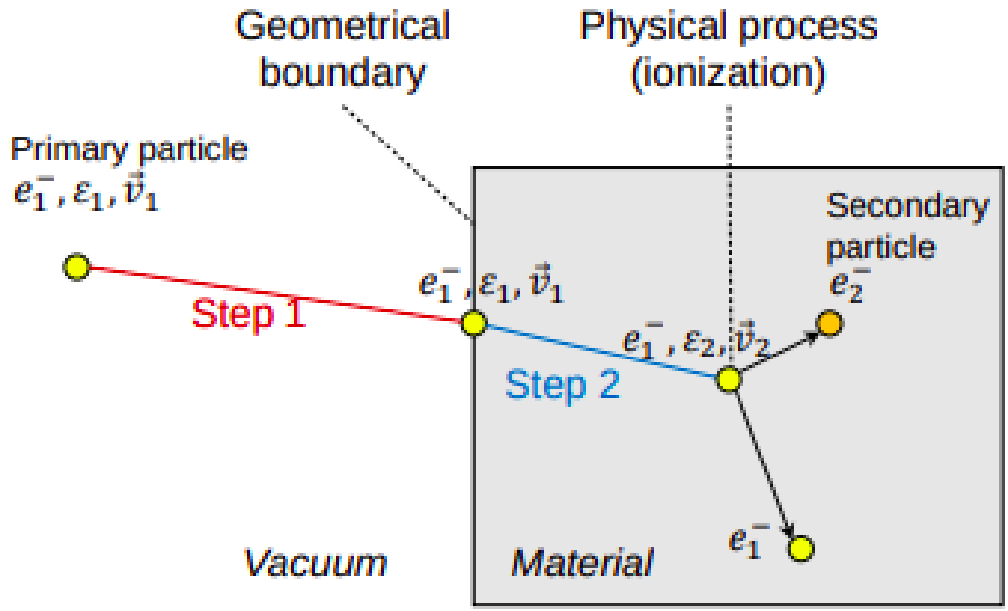

Figure 8.2: Method step visualization.

The Monte Carlo calculation method is based on random numbers for parameters:

(1) the particle emission parameters from the source such us the energy and direction, (2) physical process selection at each particle step and (3) parameters of the secondary particles generated such us the energy and direction.

For each sensitive volume, the calculation of the deposited energy and deposited dose is executed.

$$TID = \frac{E}{m} \tag{8.1}$$

With E: the energy deposited in the sensitive volume and m: the mass of the sensitive volume.

The physical processes is based on the GEANT4 software[23],[1]. The available particles that can be simulated are the following:

- electrons
- photons
- protons
- positrons

The energy range of the particles can be from 1 keV up to 1 GeV. For all charged particles a continuous energy loss process is applied due to their interaction with the electron clouds. The physical processes that can be expressed for the aforementioned particles are the following:

- electrons
  - multiple scatteting
  - ionization
  - bremmstrahlung
- photons
  - photo-electric effect
  - compton scattering
  - materialization
  - atomic relaxation
- protons
  - multiple scattering
  - ionization
- positrons
  - multiple scattering
  - ionization
  - bremmstrahlung

– annihilation

For the proper calculation of the deposited dose the source, must be defined. A source is composed of three distributions: (1) space distribution, (2) direction distribution and (3) energy distribution. Complex distributions gather both the Space and Direction distributions. The space distribution can be expressed from a point, a volume, a surface, the world or others. The direction distribution can be analyzed in (1) isotropic, (2) fixed parallel and (3) fixed angular. At last the distribution law of energy can be mone-energetic or as a function of the energy in a given file.

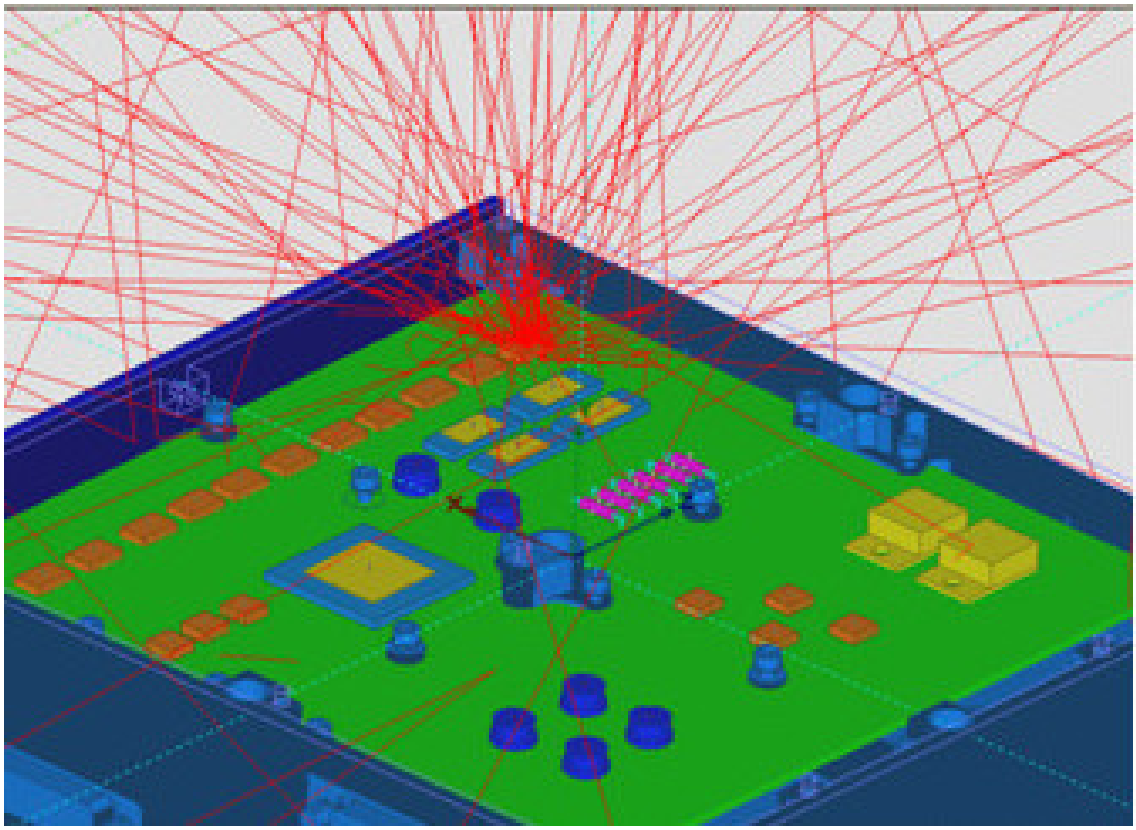

Figure 8.3: Forward Monte Carlo particle generation. From [42]

For the particle number generated the flux spectrum is utilized. The spectrum divided in energy bins: based on the energy bins of the input spectrum. Shoots the "particles number" per energy bin. Each particle is weighted depending on its number in the spectrum and only writes the results once particles were shot for all energy bins.

$$N = \sum_{i=1}^{nbofspec} n_i * (particle_number) \tag{8.2}$$

where N is the total number of particles shot and n_i the number of bins in the spectrum.

8.1.2 Ray-Tracing Method

Ray-tracing method (also known as sector analysis) allows for the calculation of dose for a 3D-model. Dedicated to TID and TNID calculation in external isotropic environment. It requires the division of the sphere surrounding the sensitive area in identical solid angles.

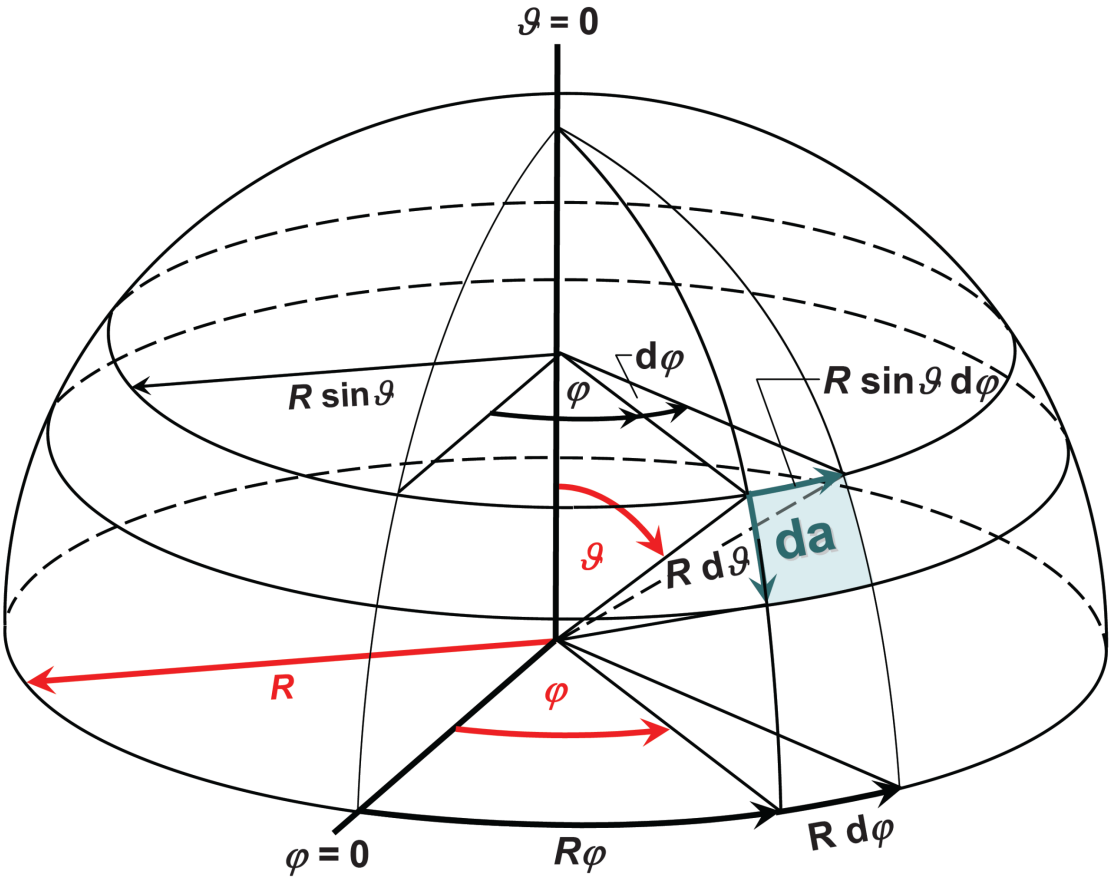

Figure 8.4: Solid angle calculation method. From the source.

When the concept of plane angles is extended into three-dimensional space, solid angles emerge. As a result, a plane circle (2D) becomes a sphere (3D), and the length of a circle's arc (2D) becomes the sphere's surface area (3D). The solid angle corresponds to the ratio of the sphere's segment area a to the square of the sphere's radius R, as seen in the image below:

$$d\Omega = \frac{da}{R^2} \tag{8.3}$$

The solid angle can be represented as, given the geometrical relations that hold for the edge of the differential segment area da:

$$d\Omega = \frac{da}{R^2} = \frac{(rsin\theta d\phi)(Rd\theta)}{R^2} = sin\theta d\theta d\phi \tag{8.4}$$

For each solid angle, dose depth method is determined. Then the total calculation is estimated by the average over all the solid angles. For the Ray-Tracing Method,

the space is divided into sectors $\Omega_i(i = 1, N)$ and the crossed equivalent aluminum thickness $\lambda_i(Al)$.

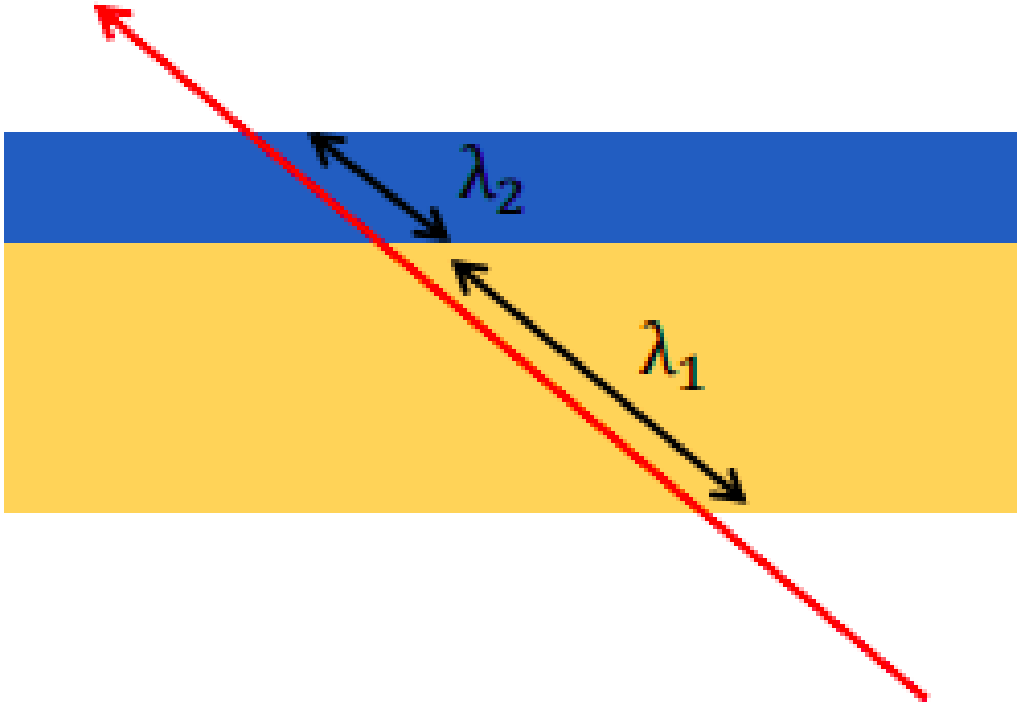

Figure 8.5: Slant Method Calculation.

$$\lambda = \lambda_1 \frac{\rho_1}{\rho_{al}} + \lambda_2 \frac{\rho_2}{\rho_{al}} \tag{8.5}$$

For the determination of the thickness the slant and minimum path are calculated. Also the method can be used for more than one mediums.

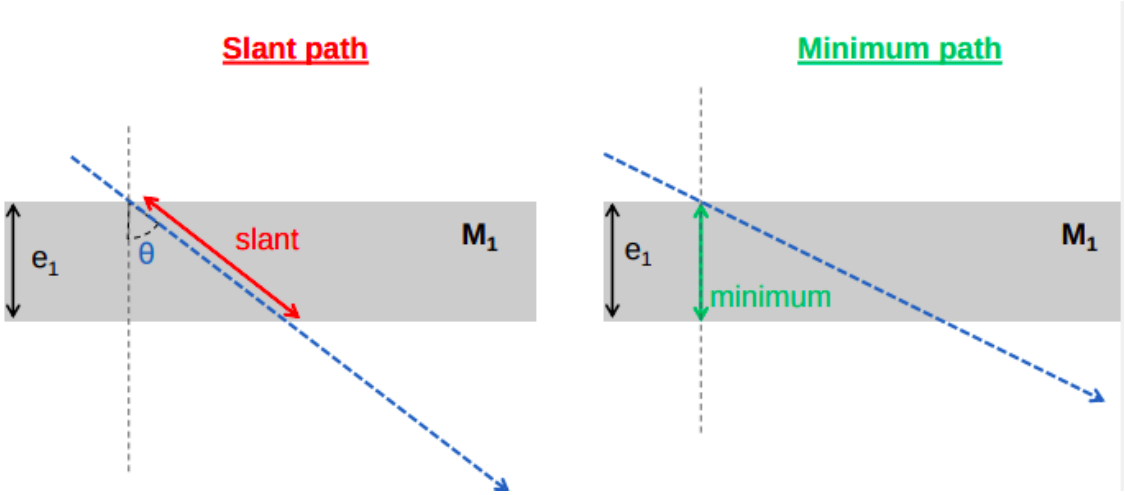

Figure 8.6: Slant path (left) and minimum path (right

The slant and minimum path are calculated respectively.

$$\lambda = \frac{e_1}{cos\theta}\frac{\rho_{M1}}{\rho_{Al}} \tag{8.6}$$

$$\lambda = e_1\frac{\rho_{M1}}{\rho_{Al}} \tag{8.7}$$

For more than one mediums, the equations are expressed as .

$$\lambda = \frac{e_1}{cos\theta}\frac{\rho_{M1}}{\rho_{Al}} + \frac{e_2}{cos\theta}\frac{\rho_{M2}}{\rho_{Al}} \tag{8.8}$$

$$\lambda = e_1\frac{\rho_{M1}}{\rho_{Al}} + e_2\frac{\rho_{M2}}{\rho_{Al}} \tag{8.9}$$

The mean dose is then calculated as:

$$D = \sum_{i=1}^{N}\frac{d(\lambda_i)\Omega_i}{4\pi} \tag{8.10}$$

There are several advantages and disadvantages in using this method for the radiation analysis.

- PROS
  - Quick dose estimation.
  - Quick shielding distribution surrounding the sensitive area.
- CONS
  - Does not take into account the properties of each material shielding, just its density (density ratio based on aluminum).
  - Particle transportation in "straight" lines (electrons behave differently).
  - Shielding reduced to equivalent spheres.
  - Target for some materials only.
  - May overestimate the dose ($>$ x2 in some cases).

8.2 Geometry Model

The model is a simplified representation of AcubeSAT. It's structure represents a 3U Cubesat, with the chosen width of the frame procured for AcubeSAT. Similar to the section for the detector placement in OMERE section 7.2, the target locations are still the same the pcb stack and the inside the vessel. However due to the 3D-Geometry, the shielding is not constant like the previous time. The dimensions for the model are the following:

Table 8.1: AcubeSAT dimensions

Dimensions	Value
height	34.5 cm
width	10 cm
length	10 cm

Consequently, the projection of xy and yz of the simplified model are the following:

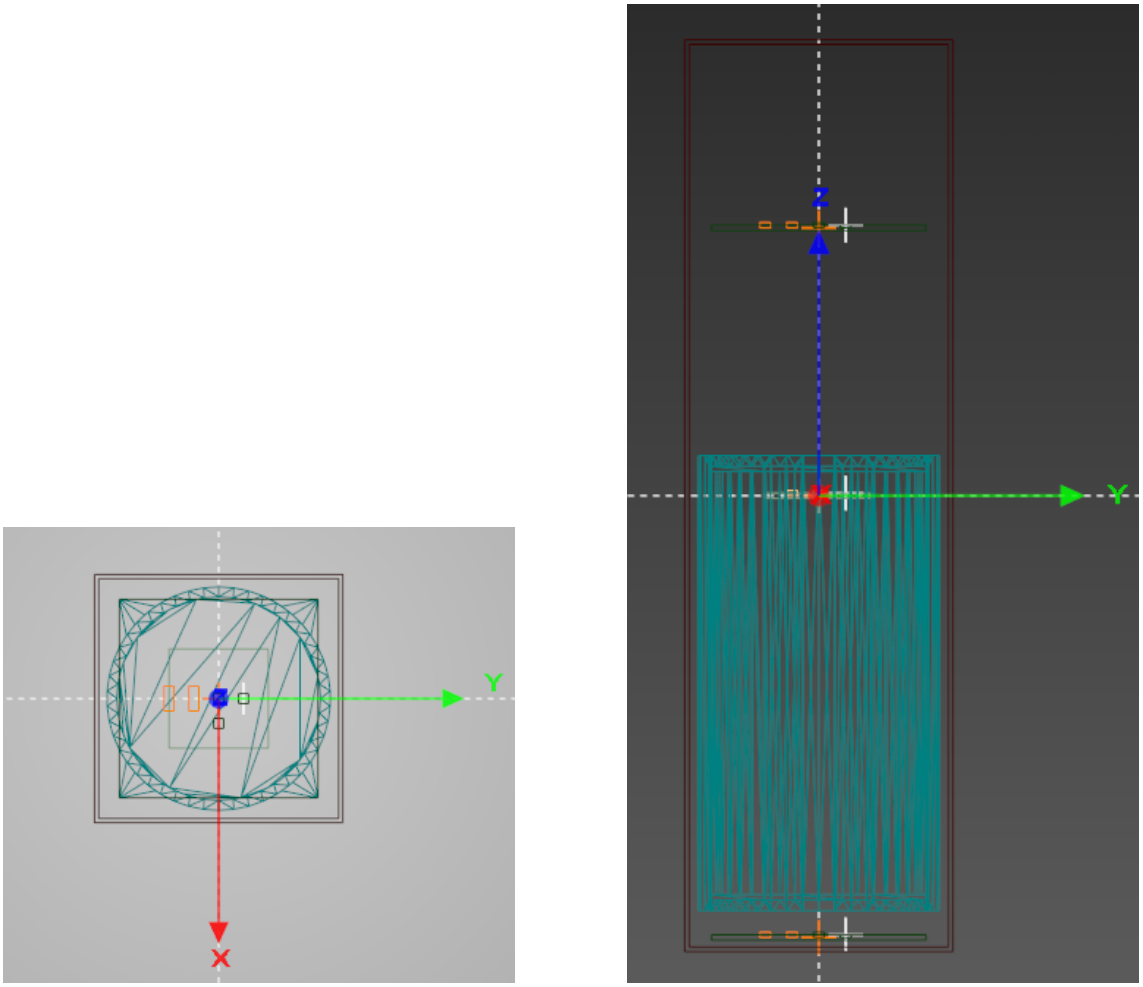

(a) The xy surface of the model.

(b) The yz surface of the model.

Figure 8.7: The AcubeSAT simplified model.

8.3 Results

In this section the results for the two simulation techniques are presented.

8.3.1 Forward Monte Carlo Method

In this subsection, the results after the simulation of the Forward Monte Carlo (FMC) is presented:

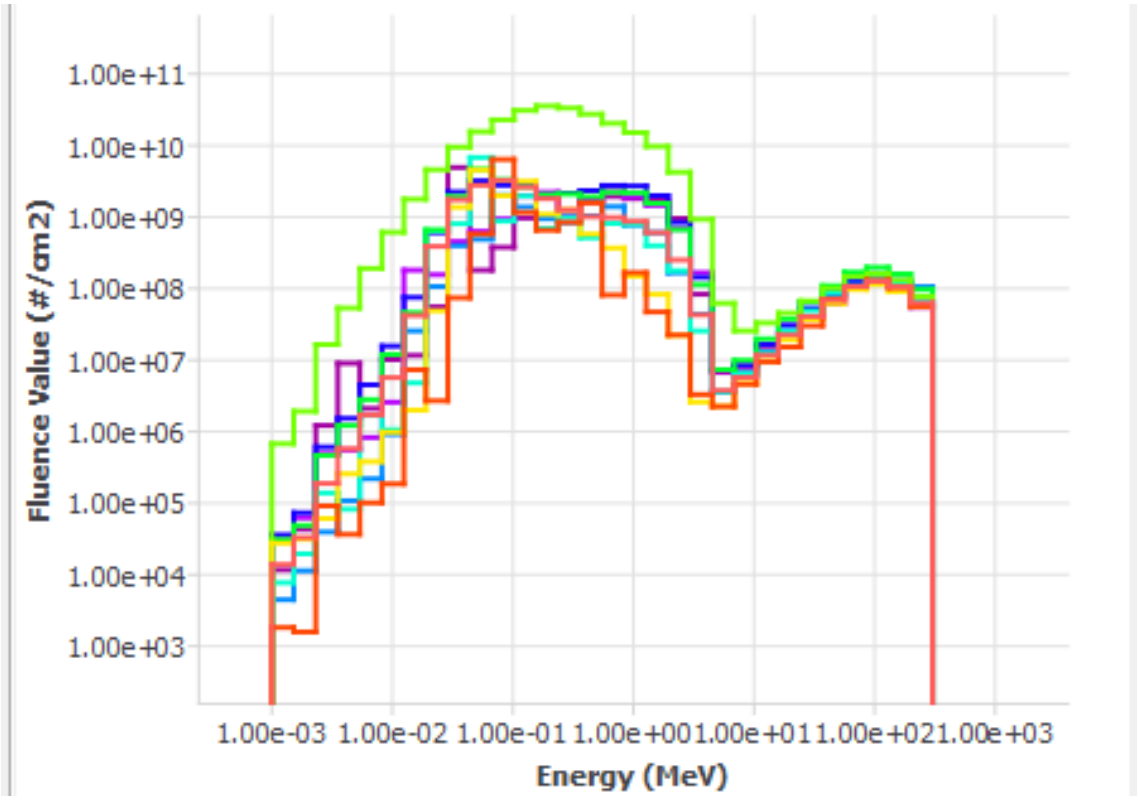

Figure 8.8: Fluence for the various detectors in the model.

Also, the map of the deposited dose for the OBC PCB is presented, as an example since the other ones are similar.

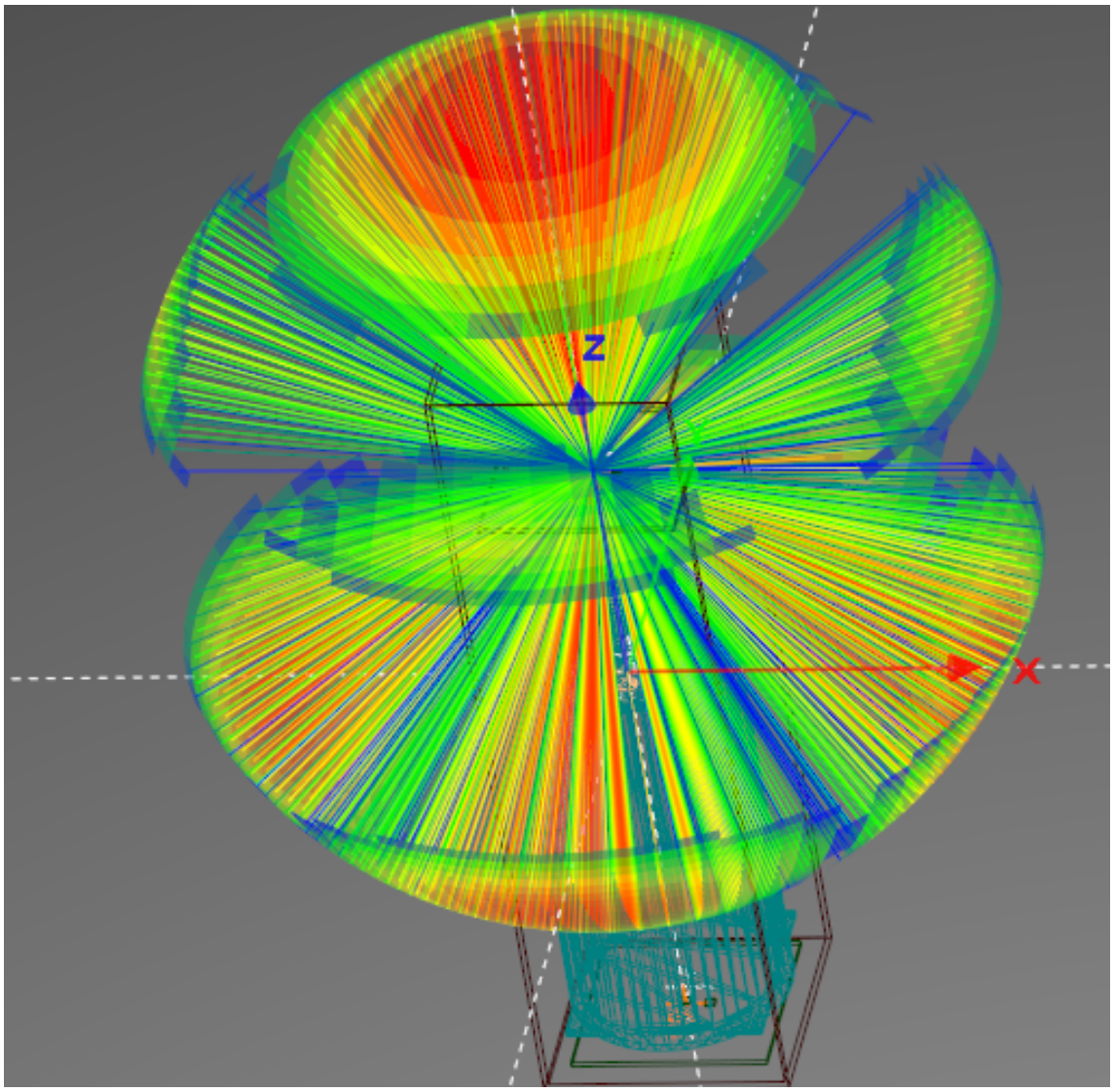

Figure 8.9: Deposited dose in the OBC PCB

Furthermore, the values of the deposited dose and its error are presented:

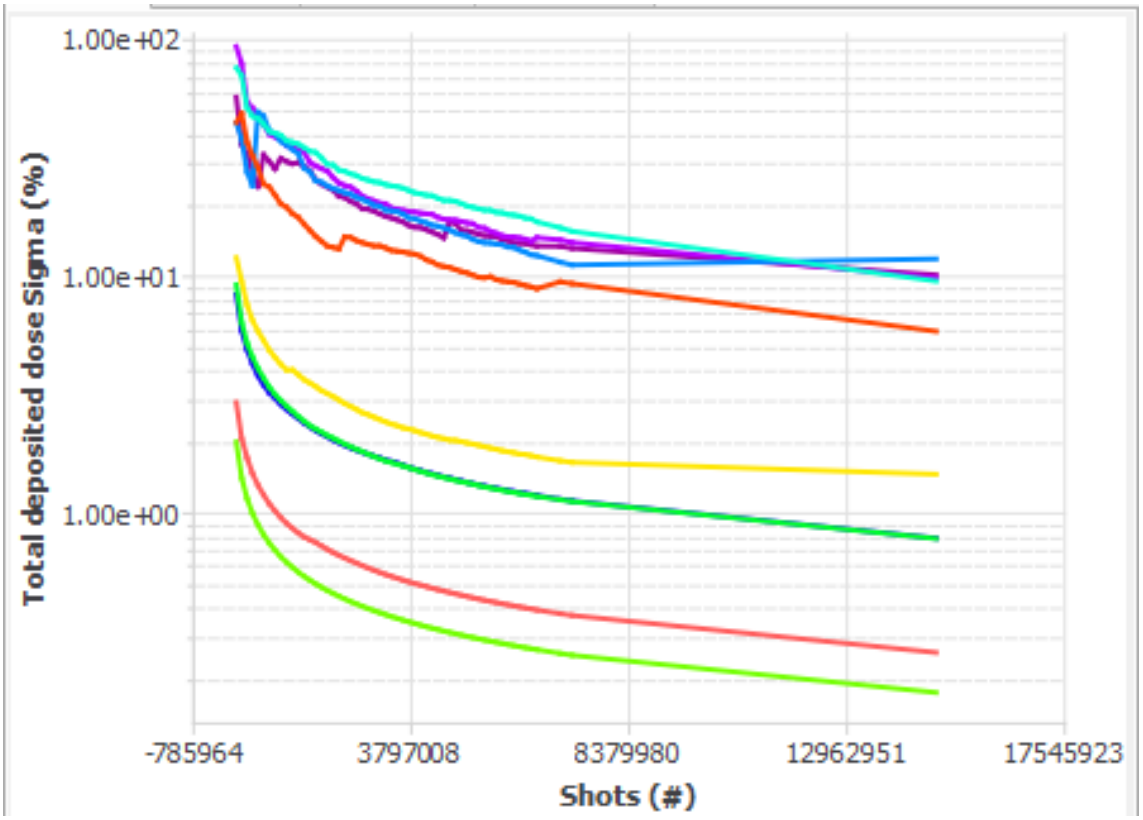

Figure 8.10: Error in the deposited dose

Table 8.2: Dose-depth values for the FMC method

Detector	Deposited dose (krad)	Sigma (%)
OBC PCB	1.45	0.79
SU Experiment	0.88	6.59
SU MRAM	0.712	4.88

8.3.2 Ray-Tracing Method

In this subsection, the map after the simulation of the Ray-Tracing Method (RTC) is presented:

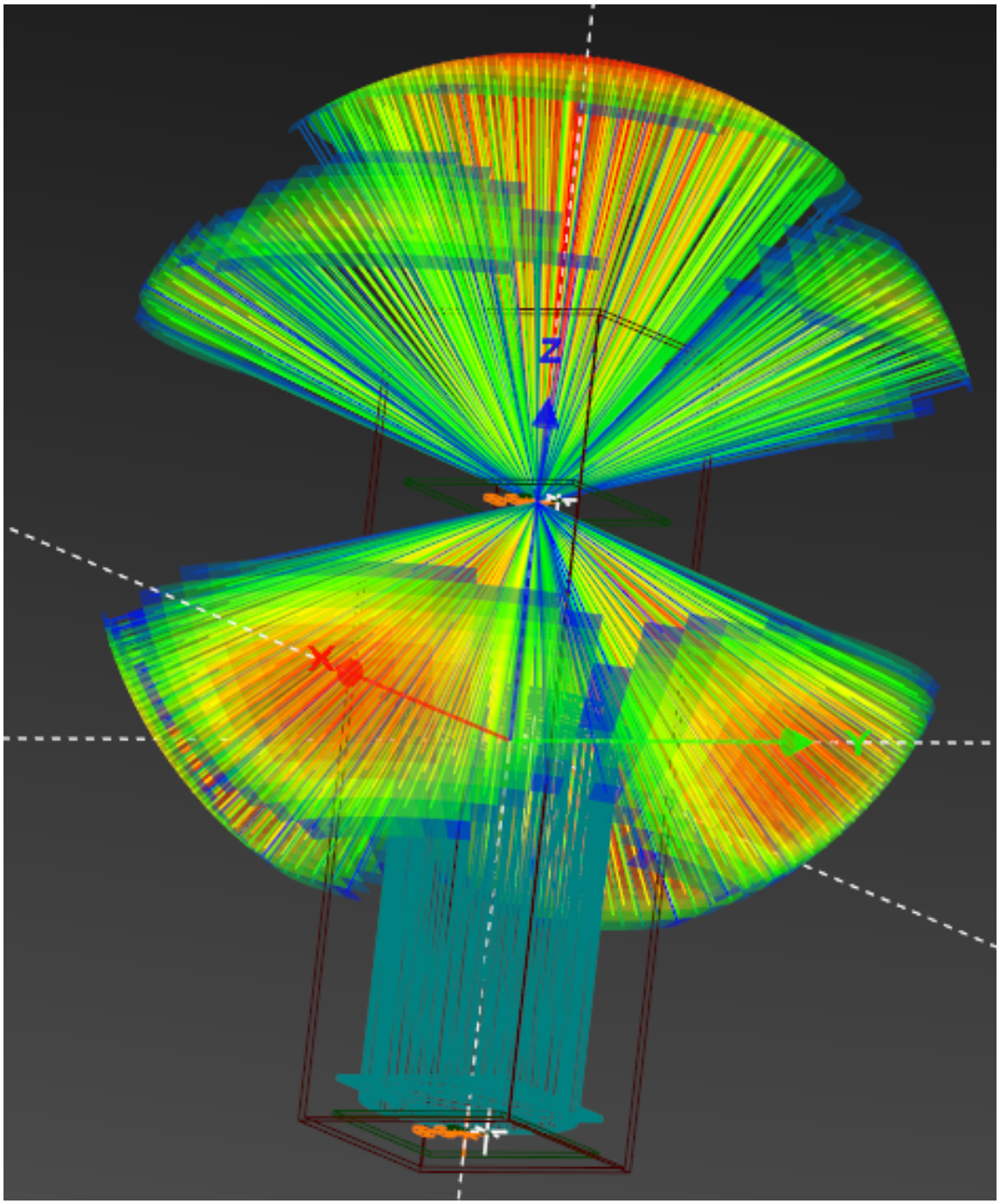

Figure 8.11: The rays tracing from the detector placed inside the OBC PCB

Furthermore, the deposited doses after the simulation are shown in the following Table 8.3:

Table 8.3: Ray-tracing method deposited doses

Detector	Deposited dose (krad)
OBC PCB	2.17
SU experiment	0.725
SU PCB	0.421

9. Conclusion

Several satellite models have been exposed to the radiation environment of the AcubeSAT's orbit. The results of these models' radiation shielding are discussed in this section. A ray-tracing simulation was used to evaluate simplified models to see which materials would improve the satellite's radiation protection. A ray-tracing simulation like this gives you a good idea of how much radiation you're getting at each location in the model (where one has placed a detector). This ray-tracing method also provides an overview of the radiation doses received by this detector from various directions. This makes the ray-tracing method worthwhile because it will reveal which areas of the satellite should be protected more effectively.

It should be considered in future simulations is that the detectors should be arranged in such a way with more shielding, since some additional geometry elements are not included in the model due to its complexity. As a result, the dose value is projected to be slightly higher than the values found in the tables in the FASTRAD simulations.Simulations are still being run to determine the exact value. Following the sector analysis, Monte Carlo simulations are run with a higher computation resolution, resulting in more accurate and reliable findings.

In order to avoid some hazards, potential threats, and determine the background, a study of the radiation environment to which a space mission will be exposed is required. Because of the relevance of this analysis, a specific simulation was run during the satellite's development. All the results are summarized in Table 7.3,Table 7.4, Table 8.2 and Table 8.3. Now it is time to summarize and recount the most compelling findings.

9.1 Sector Shielding Analysis for future improvement

The sector files developed in this thesis, particularly the sector shielding analysis of the 3U model, will be useful for future CubeSat structure study. For the mission, the dense grid of detectors in the model has generated a wealth of information regarding the direction from which each point in a 3U CubeSat structure receives its radiation dose, which could be used for further studies.

9.2 FMC Method

Now it clear that the FMC method is computationally intensive. The errors all, where close to the 5% limit in order to be acceptable. However, for smaller dimension targets the error is far higher and require more time or threads in the computer.

In order to achieve this results a 6 hour minimum simulation was required. Also, the simulations were carried in the computer of the team. For further, analysis it is likely that the Aristotle's cluster will be needed.

9.3 Model Variation

From the results, it is clear that there is a variation in the values of the deposited dose in the different geometry models. The model of OMERE was much more simple, than the FASTRAD one as expected, however there wasn't a significant enough difference that could give us false assurances for our team's design requirements.

9.4 AcubeSAT viability

From the thesis, which is an accumulation of some of the work performed in the team. As part of the levels of the Total Ionizing Energy (TID) we can be certain, that none of the critical components of the satellite will exceed the 10 krad threshold set by the team as a requirement. Therefore there is minimal chance of total ionizing damage caused in the satellite. As a result, the team should be more focused in the SEE section A.1, which however was not investigated as part of this thesis.

9.5 Future Work

This section will list research subjects that have not yet been completed but could lead to major results in the radiation shielding of future CubeSat flights to low earth space.

9.5.1 CubeSAT models

Even-though the thesis was mainly concentrated for AcubeSAT mission, the model was not the actual and further studies should be implemented in order to approximate the model more truthfully, but with not a significant strain in the computational resources. Furthermore, more CubeSat models could be studied like 6U or even larger.

9.5.2 Radiation Methods

In the thesis, two simulation methods, the Ray-Tracing Method (RTC) and the Forward Monte Carlo (FMC), have been carried out. However, there is also the possibility of inclusion other methods such us the Reverse Monte Carlo (RMC) and the Internal Charging (IC). Since, for the LEO orbit most of the radiation sources are omnidirectional, the RMC method could be useful.

A. Radiation Effects

A.1 Single Event Effects - SEE

Single Event Effects are connected with the generation of electron-hole pairs in semiconductor material when exposed to ionizing radiation. The number of pairs generated is proportional to the energy deposited. For semiconductor devices, the parameter LETth (Linear Energy Transfer Threshold) is defined, being a measure of how susceptible the device is. For particles with Linear Energy Transfer (LET - normalized particle energy per mass of the absorbing material) below this threshold no effect will be observed. Single Event Effects are divided into two groups - non-destructive (fully recoverable, possibly after power cycle) and destructive (permanent damage) effects. These are described below, defined as:

- Non-destructive effects
  - Single Event Upset
    - Single Event Functional Interrupt
  - Single Event Transient
- Destructive effects
  - Single Event Latch-up
  - Single Event Gate Rupture
  - Single Event Burnout

.

A.2 Total Ionizing Dose - TID

TID is defined as the total energy absorbed during exposure. This can be caused by any kind of radiation, behaving differently in every semiconductor device. In general, TID successively degrades electronic device parameters over time, causing them to stop functioning when critical irradiation is reached. The total ionizing dose (TID), mostly due to electrons and protons, can result in device failure (or biological damage to astronauts). In either case, TID can be measured in terms of the absorbed dose, which is a measure of the energy absorbed by matter. Absorbed dose is quantified using either a unit called the rad (an acronym for radiation absorbed dose) or the SI unit which is the gray (Gy); 1 Gy = 100 rads = 1 J/kg.

B. Workflow-diagram

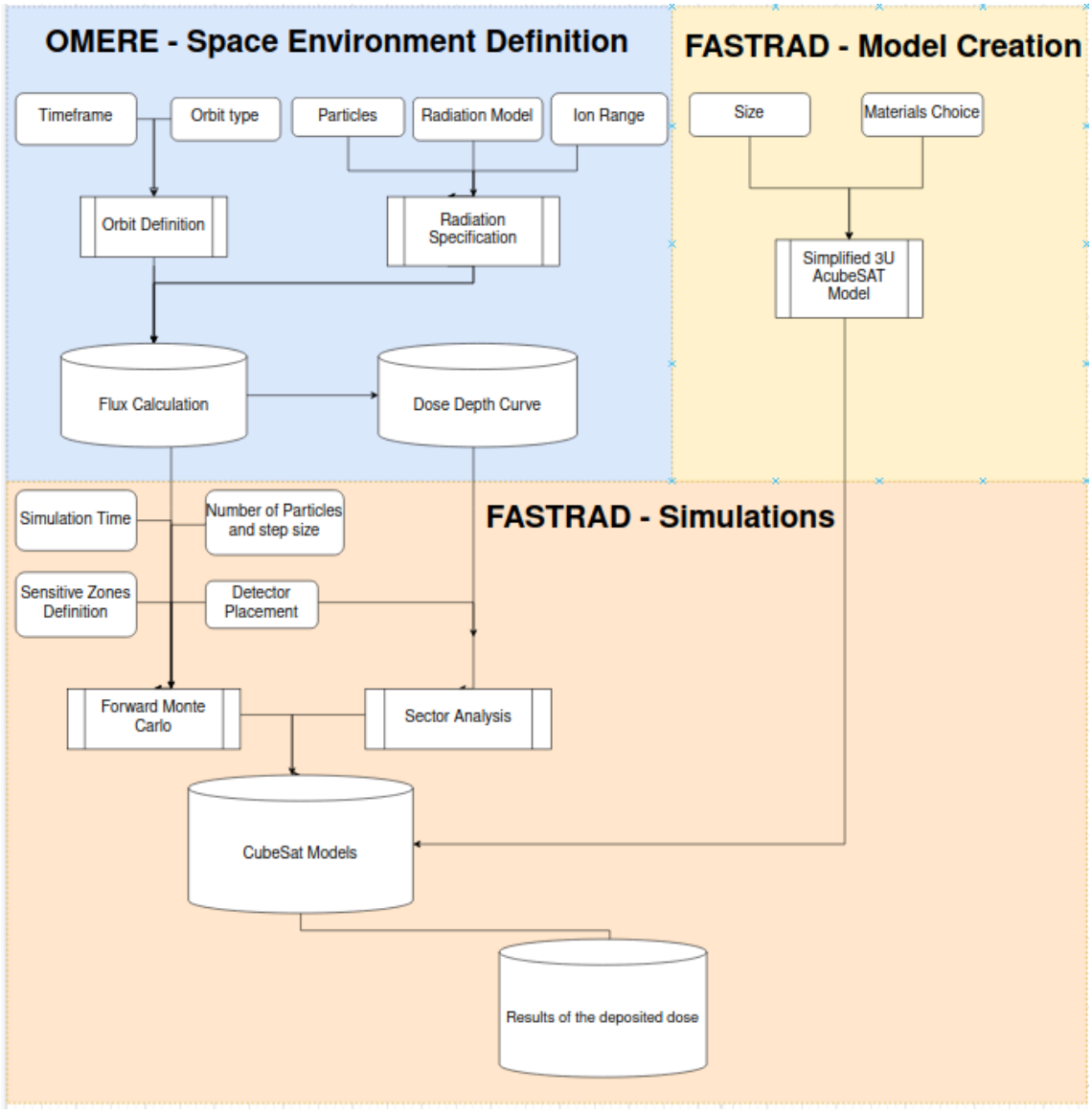

Figure B.1: Workflow Diagram

Bibliography

[1] Sea Agostinelli, John Allison, K al Amako, John Apostolakis, H Araujo, Pedro Arce, Makoto Asai, D Axen, Swagato Banerjee, GJNI Barrand, et al. Geant4—a simulation toolkit. *Nuclear instruments and methods in physics research section A: Accelerators, Spectrometers, Detectors and Associated Equipment*, 506(3):250–303, 2003.

[2] F Alby, D Alwes, Luciano Anselmo, H Baccini, Christophe Bonnal, R Crowther, W Flury, Rüdiger Jehn, H. Klinkrad, C Portelli, and R Tremayne-Smith. The european space debris safety and mitigation standard. *Advances in Space Research*, 34:1260–1263, 09 2001.

[3] R Antoni and L Bourgois. *Applied physics of external radiation exposure: Dosimetry and radiation protection.* Springer, Cham, Switzerland, 2017.

[4] Gautam D. Badhwar. The Radiation Environment in Low-Earth Orbit. *Radiation Research*, 148(5s):S3–S10, 11 1997.

[5] E.R Benton and E.V Benton. Space radiation dosimetry in low-earth orbit and beyond. *Nuclear Instruments and Methods in Physics Research Section B: Beam Interactions with Materials and Atoms*, 184(1):255–294, 2001. Advanced Topics in Solid State Dosimetry.

[6] J Collot. Cours de physique expérimentale des hautes énergies du dea de physique théorique rhône-alpes. 2001.

[7] Secretariat ECSS. Space environment. Technical report, ECSS-E-10-04A, ESA Publications Division [Internet], 2000. Available from . . . , 2008.

[8] Nikolay Emelyanov. 3 - equations of motion and analytic theories. In Nikolay Emelyanov, editor, *The Dynamics of Natural Satellites of the Planets*, pages 39–149. Elsevier, 2021.

[9] SB Gabriel. Cosmic rays and solar protons in the near-earth environment and their entry into the magnetosphere. In *Proceedings of ESA Workshop on Space Weather,(Invited Paper), ESA WPP-155*, pages 99–106, 1998.

[10] Robért Glein, Florian Rittner, and Albert Heuberger. Adaptive single-event effect mitigation for dependable processing systems based on fpgas. *Microprocessors and Microsystems*, 59:46–56, 2018.

[11] Jeffrey Jones and Fathi Karouia. *Radiation Disorders*, pages 475–519. 03 2008.

[12] Oskar Klein and Yoshio Nishina. Über die streuung von strahlung durch freie elektronen nach der neuen relativistischen quantendynamik von dirac. *Zeitschrift für Physik*, 52(11):853–868, 1929.

[13] MICHAEL F. L'ANNUNZIATA. 1 - nuclear radiation, its interaction with matter and radioisotope decay. In Michael F. L'Annunziata, editor, *Handbook of Radioactivity Analysis (Second Edition)*, pages 1–121. Academic Press, San Diego, second edition edition, 2003.

[14] W J Larson and J R Wertz. Space mission analysis and design. 1 1992.

[15] Alan Martin, Sam Harbison, Karen Beach, and Peter Cole. *An introduction to radiation protection*. CRC Press, 2018.

[16] RA Mewaldt, AC Cummings, James H Adams Jr, Paul Evenson, W Fillius, JR Jokipii, RB McKibben, and Paul A Robinson Jr. Toward a descriptive model of galactic cosmic rays in the heliosphere. In *Interplanetary Particle Environment. Proceedings of a Conference*, 1988.

[17] E.N. Parker. The passage of energetic charged particles through interplanetary space. *Planetary and Space Science*, 13(1):9–49, 1965.

[18] Pierre Pourrouquet, Jean-Charles Thomas, Pierre-Francois Peyrard, Robert Ecoffet, and Guy Rolland. Fastrad 3.2: Radiation shielding tool with a new monte carlo module. In *2011 IEEE Radiation Effects Data Workshop*, pages 1–5. IEEE, 2011.

[19] AcubeSAT Project. *CDR: Critical Design Review*. SpaceDot Team, 2 edition, 2021.

[20] Gerd W. Prolss. *Physics of the Earth's space environment : an introduction / Gerd W. Prolss.* Springer, Berlin ;, 2004.

[21] Robert.wickramatunga. United nationsoffice for outer space affairs.

[22] Lisa Rosenqvist, A Hilgers, H Evans, E Daly, M Hapgood, R Stamper, R Zwickl, S Bourdarie, and D Boscher. Toolkit for updating interplanetary proton cumulated fluence models. *Journal of spacecraft and rockets*, 42(6):1077–1090, 2005.

[23] G Santina, P Nieminen, H Evansa, E Daly, F Lei, PR Truscott, CS Dyer, B Quaghebeur, and D Heynderickx. New geant4 based simulation tools for space radiation shielding and effects analysis. *Nuclear Physics B-Proceedings Supplements*, 125:69–74, 2003.

[24] Wayne A Shiroma, Larry K Martin, Justin M Akagi, Jason T Akagi, Byron L Wolfe, Bryan A Fewell, and Aaron T Ohta. Cubesats: A bright future for nanosatellites. *Central European Journal of Engineering*, 1(1):9–15, 2011.

[25] EG Stassinopoulos and JH King. Empirical solar proton model for orbiting spacecraft applications. *IEEE Transactions on Aerospace and Electronic Systems*, (4):442–450, 1974.

[26] Carl Störmer. *The polar aurora*. Clarendon Press, 1955.

[27] JUICE team. Juice environment specification, 2017.

[28] David J. Thomas. ICRU report 85: fundamental quantities and units for ionizing radiation. *Radiation Protection Dosimetry*, 150(4):550–552, 05 2012.

[29] Vlado Valković. Chapter 5 - measurements of radioactivity. In Vlado Valković, editor, *Radioactivity in the Environment*, pages 117–258. Elsevier Science, Amsterdam, 2000.

[30] James A Van Allen. Radiation belts around the earth. *Scientific American*, 200(3):39–47, 1959.

[31] Vinay Venugopal and Piyush Bhagdikar. de broglie wavelength and frequency of scattered electrons in the compton effect. *Physics Education*, 29:35, 03 2013.

[32] James I Vette. *The AE-8 trapped electron model environment*, volume 91. National Space Science Data Center (NSSDC), World Data Center A for Rockets ..., 1991.

[33] Kirk Woellert, Pascale Ehrenfreund, Antonio J Ricco, and Henry Hertzfeld. Cubesats: Cost-effective science and technology platforms for emerging and developing nations. *Advances in space Research*, 47(4):663–684, 2011.

[34] Luis Zea, Victor Ayerdi, Sergio Argueta, and Antonio Muñoz. A methodology for cubesat mission selection. *J. Small Satell*, 5(3):483–511, 2016.

[35] Curtis, Howard D. Orbital Mechanics for Engineering Students. Amsterdam: Elsevier Butterworth Heinemann, 2005.

[36] www.spacedot.gr/

[37] https://phys.org/news/2020-09-solar-begun.html

[38] www.acubesat.spacedot.gr/

[39] www.esa.int/ESA_Multimedia

[40] www.trad.fr/en/space/omere-software/

[41] www.geomag.bgs.ac.uk/education/earthmag.html

[42] www.fastrad.net/

Declaration of authorship

I hereby declare that the report submitted is my own unaided work. All direct or indirect sources used are acknowledged as references. I am aware that the Thesis in digital form can be examined for the use of unauthorized aid and in order to determine whether the report as a whole or parts incorporated in it may be deemed as plagiarism. For the comparison of my work with existing sources I agree that it shall be entered in a database where it shall also remain after examination, to enable comparison with future Theses submitted. Further rights of reproduction and usage, however, are not granted here. This paper was not previously presented to another examination board and has not been published.

Location, date

_____

Name